Machine Learning-Aided Design of Additively Manufactured Ridge Gap Waveguide Components

by

Mohammed Farouk NAKMOUCHE

MANUSCRIPT-BASED THESIS PRESENTED TO ÉCOLE DE TECHNOLOGIE SUPÉRIEURE
IN PARTIAL FULFILLMENT FOR THE DEGREE OF
DOCTOR OF PHILOSOPHY
Ph.D.

MONTREAL, SEPTEMBER 8, 2025

ÉCOLE DE TECHNOLOGIE SUPÉRIEURE
UNIVERSITÉ DU QUÉBEC

BOARD OF EXAMINERS

THIS THESIS HAS BEEN EVALUATED

BY THE FOLLOWING BOARD OF EXAMINERS

Mr. Ghyslain Gagnon, thesis supervisor
Engineering Department at École de technologie supérieure

Mr. Dominic Deslandes, co-supervisor
Engineering Department at École de technologie supérieure

Mr. Vladimir Brailovski, president of the board of examiners
Engineering Department at École de technologie supérieure

Mr. Frédéric Nabki, member of the jury
Engineering Department at École de technologie supérieure

Mr. Tarek Djerafi, external independent examiner
Institut national de la recherche scientifique

THIS THESIS WAS PRESENTED AND DEFENDED

IN THE PRESENCE OF A BOARD OF EXAMINERS AND THE PUBLIC

ON 28, AUGUST, 2025

AT ÉCOLE DE TECHNOLOGIE SUPÉRIEURE

ACKNOWLEDGEMENTS

For many in my country, Algeria, a career path with the nation's prominent petroleum industry is a common goal to reach. However, my fascination lay elsewhere in the intricate and elegant language of engineering that overcomes geographical boundaries. This early yearning to understand the "soul" of technology led me to pursue my bachelor's and master's degrees at the University of Laghouat Amar Telidji Université. This academic foundation became a springboard, propelling me through enriching experiences in Turkey, France, and Taiwan, where I had the privilege of learning from and collaborating with leading figures in the advancing field of antenna engineering. This led me to the doctorate degree at École de Technologie Supérieure (ÉTS) in Montréal, Canada, under the supervision of my two professors, Professor Ghyslain Gagnon and Professor Dominic Deslandes.

Beyond extending praise and gratitude to the One to whom all thanks are ultimately due, I wish to sincerely thank those whose presence in my life, by His wisdom, has shaped my journey and contributed to my growth.

I would like to express my deepest gratitude to Professor Ghyslain Gagnon, who transformed my aspirations into a rigorous research program, providing a framework for writing, project management, and scientific integrity. I would equally like to express my gratitude to Professor Dominic Deslandes, who deepened my ability to analyze electromagnetic problems and strengthened the technical foundations of my work. Together, they have shown me that the best mentors nurture innovation, encourage independence, and provide an environment where students' creativity can truly blossom, enabling them to cultivate fruitful research results.

I also warmly thank the many colleagues, mentors, and friends who supported this journey with their wisdom and encouragement, namely, Diaa Gadelmola, Abdelmajid Allam, Shokry Shams, Mahmoud Elsaadany, and Anis Ben Arfi, as well as the IEEE MTT-S community and my peers at the Laboratoire de Communications et d'Intégration de la MicroÉlectronique (LaCIME). My special thanks go to Philippe Olivier, who welcomed me during my first two weeks at ÉTS and shared many coffee-fueled discussions on RF and microwave research and current development. I am also grateful to the Department of Electrical Engineering technicians, especially André Zelzal, whose skilled assistance was indispensable during fabrication and to Professor Vladimir and his student Anatolie Timercan, whose expertise in 3D printing brought several of my prototypes to life. My deepest appreciation also goes to the countless others whom I didn't mention; your various forms of support were essential to the completion of my PhD research.

I am forever indebted to my family for their unwavering support and guidance. To my father, Belabbas, and my mother, Zoulikha, for their encouraging words and for their unwavering support and tremendous amount of patience. I also would like to thank my sisters, Ines, Imane, and Faiza, for their kindness and encouragement.

This thesis stands as a testament to the collective support of all these remarkable individuals.

Approche de synthèse dirigée par apprentissage automatique pour la conception de composants passifs et d'antennes basés sur un guide d'ondes à rainure de crête fabriqué par fabrication additive

Mohammed Farouk NAKMOUCHE

RÉSUMÉ

La rapide évolution des systèmes sans fil de nouvelle génération engendre des défis majeurs pour la conception de composants passifs compacts à hautes performances et d'antennes massives MIMO. Les processus de conception classiques des cellules unitaires de guide d'ondes à rainure (RGW) et de guide d'ondes à rainure imprimé (PRGW) reposent sur des simulations électromagnétiques (EM) pleine onde et des études paramétriques itératives pour déterminer les fréquences de bande d'arrêt, ce qui se traduit par des coûts de calcul prohibitifs, des délais d'exécution très longs et une généralisabilité limitée des formules de dispersion analytiques. Parallèlement, les progrès en électromagnétique computationnelle (CEM), notamment les résolveurs MoM, FEM et FDTD, ont amélioré la fidélité des modèles sans pour autant diminuer les besoins en mémoire et en puissance de calcul nécessaires à l'affinage manuel des conceptions.

Motivée par le succès de l'apprentissage automatique (ML) dans d'autres domaines et par l'essor des recherches EM basées sur l'intelligence artificielle, cette thèse propose un cadre de synthèse entièrement automatisé et conscient des contraintes de fabrication pour les cellules unitaires RGW/PRGW, exploitant l'apprentissage supervisé pour remplacer le travail itératif manuel.

Un jeu de données EM de haute fidélité couvrant de 3 à 300 GHz et intégrant les variations géométriques liées à la fabrication additive et aux matériaux diélectriques a été généré par des simulations automatisées. Des approches de programmation génétique (GP) et de réseaux de neurones artificiels (ANN) ont ensuite été implémentées, comparées et optimisées pour apprendre à la fois le passage direct (geometry $\rightarrow$ performance) et le passage inverse (performance $\rightarrow$ geometry) avec une précision proche de celle des méthodes pleine onde et des temps d'exécution drastiquement réduits (minutes contre heures/jours).

Les contributions clés sont :

- Le premier cadre de synthèse complet piloté par ML pour les cellules unitaires métalliques RGW/PRGW.
- Un jeu de données EM évolutif et conscient des contraintes de fabrication couvrant 3–300 GHz.
- Une comparaison systématique des méthodes GP et ANN en conception inverse, évaluées selon les métriques MSE, MAE, MAPE et les temps de calcul.
- La conception, l'impression 3D et la validation expérimentale d'antennes MIMO PRGW à large bande, forte isolation et reconfigurables en diagramme de rayonnement, y compris un réseau origami 8×8 avec résonateurs diélectriques multipermittivité.

Les résultats montrent que la synthèse assistée par ML peut suppléer aux itérations EM traditionnelles, ouvrant une voie évolutive vers des modules System-on-Package compacts et économiques pour les communications mm-wave. La thèse se conclut par une discussion des limitations et propose des pistes prometteuses pour le renforcement de l'apprentissage, la génération avancée de données et la modélisation inverse en conception EM.

Mots-clés: Guide d'ondes à rainure imprimé, guide d'ondes à rainure, apprentissage automatique, programmation génétique, apprentissage profond, entrées multiples, sorties multiples (MIMO) and fabrication additive (FA)

Machine Learning-Aided Design of Additively Manufactured Ridge Gap Waveguide Components

Mohammed Farouk NAKMOUCHE

ABSTRACT

The rapid evolution of next-generation wireless systems poses significant challenges for the design of compact, high-performance passive components and massive-MIMO antenna arrays. Conventional workflows for ridge gap waveguide (RGW) and printed ridge gap waveguide (PRGW) unit cells rely on iterative full-wave EM simulations and parametric studies to locate stop-band frequencies, resulting in prohibitive computational cost, long turn-around times, and limited generalizability of analytical dispersion formulas. Meanwhile, advances in computational electromagnetics (CEM) including MoM, FEM, and FDTD solvers have eased model fidelity but not the excessive memory and processing demands required to refine designs by hand.

Motivated by the success of machine learning (ML) in other fields and the growing volume of AI-based EM research, this thesis develops a fully automated, fabrication-aware synthesis framework for RGW/PRGW unit cells that leverages supervised learning to replace manual trial-and-error.

A high-fidelity dataset covering 3–300 GHz and accounting for geometric variations related to additive manufacturing and dielectric materials was generated via automated EM simulations. Genetic programming (GP) and artificial neural networks (ANN) were then implemented, benchmarked, and optimized to learn both forward (geometry $\rightarrow$ performance) and inverse (performance $\rightarrow$ geometry) mappings with near-full-wave accuracy and drastically reduced run-times (minutes vs. hours/days).

Key contributions include:

- The first end-to-end ML-driven synthesis framework for metallic RGW/PRGW unit cells.
- A scalable, fabrication-aware EM dataset enabling data-driven modeling across 3–300 GHz.
- Systematic comparison of GP and ANN inverse-design approaches using MSE, MAE, MAPE, and timing metrics.
- Design, 3D-printing, and experimental validation of wideband, highly isolated, pattern-reconfigurable PRGW-based MIMO antennas, including an origami-inspired 8×8 array with multi-permittivity dielectric resonators.

The results demonstrate that ML-aided synthesis can overcome brute-force EM iteration, offering a scalable path toward compact, cost-effective System-on-Package modules for future mm-wave communications. The thesis concludes with a discussion of limitations and outlines promising directions for reinforcement learning, advanced data generation, and inverse modeling in EM structure design.

Keywords: Printed ridge gap waveguide, ridge gap waveguide, machine learning, genetics programming, deep learning, multiple input multiple output (MIMO), additive manufacturing (AM)

TABLE OF CONTENTS

Page

LIST OF TABLES

Page

LIST OF FIGURES

LIST OF ALGORITHMS

LIST OF ABREVIATIONS

AlSi10Mg	Aluminium–Silicon–Magnesium alloy powder
RGW	Ridge Gap Waveguide
PRGW	Printed Ridge Gap Waveguide
ML	Machine Learning
EM	Electromagnetic
PSO	Particle Swarm Optimization
GA	Genetic Algorithm
k-NN	k-Nearest Neighbors
MSE	Mean Squared Error
MAE	Mean Absolute Error
MAPE	Mean Absolute Percentage Error
LPBF	Laser Powder Bed Fusion
MSL	Microstrip Line
SIW	Substrate Integrated Waveguide
EBG	Electromagnetic Band Gap
AMC	Artificial Magnetic Conductor
PMC	Perfect Magnetic Conductor
MoM	Method of Moments
FEM	Finite Element Method
FDTD	Finite-Difference Time-Domain
CST	Computer Simulation Technology
SLA	Stereolithography (3D-printing file format)
TRL	Thru-Reflect-Line (de-embedding method)
VNA	Vector Network Analyzer

ANN	Artificial Neural Network
DGS	Defected Ground Structure
MIMO	Multiple-Input Multiple-Output
IoS	Internet of Space
DRA	Dielectric Resonator Antenna
DR	Dielectric Resonator
PLA	Polylactic Acid
LEO	Low Earth Orbit
Q-TEM	Quasi-Transverse Electromagnetic

LIST OF SYMBOLS AND UNITS OF MEASUREMENTS

ρ	Surface roughness
Ω	Ohm
Hz	Hertz
GHz	Gigahertz
m	Meter
s	Second
V	Volt
W	Watt
R^2	Coefficient of determination
σ	Standard deviation

INTRODUCTION

0.1 Motivation and Challenges

In modern communication systems, the modeling and co-design of antennas and passive components involve complex iterative processes that integrate design and optimization. Traditionally, electromagnetic (EM) structures such as antennas, filters, feeding networks, couplers, and interconnections have been designed using computational electromagnetics (CEM). Based on Maxwell's equations, CEM (Sumithra & Thiripurasundari, 2017; Tayli, 2018; Volakis, Johnson & Jasik, 2007) models the interaction of electromagnetic fields with EM structures, providing approximate solutions that enhance our understanding of both their physical structures and performance. Initially, we analyzed EM structure using integral equations. However, advances in computer memory and processing power have enabled the use of both integral and differential equation solvers for Maxwell's equations. One such approach, the Method of Moments (MoM) (Gibson, 2014), was introduced to solve integral equations. Over time, researchers developed differential equation solvers such as the Finite Element Method (FEM) and the Finite-Difference Time Domain (FDTD), capable of handling a greater number of unknowns and facilitating the analysis of more complex EM structures.

Despite these advancements, antenna and passive component design using integral and differential equation solvers is influenced by two key factors: the reliance on computationally expensive electromagnetic simulations for performance prediction and the need for extensive domain expertise and empirical methods for design refinement. The latter arises from the former, as numerical modeling and optimization in antenna design remain challenging, demanding substantial memory and processing power, both of which scale with the size of the EM structure (Gupta, Karahan, Bhat, Sengupta & Khankhoje, 2023). The advancements in high-performance computing, big data, and software engineering, along with the success of machine learning in fields such as image processing and economic forecasting, are driving a paradigm shift in antenna and passive component design (El Misilmani, Naous & Al Khatib, 2020; Lu, Pestourie, Yao, Wang, Verdugo & Johnson, 2021). Artificial intelligence (AI) enables machines to perform tasks that typically require human thought, including learning, decision-making, and problem-solving. This technology has become an important part of today's research projects and is driving changes in many fields, including EM structure design.

To gain deeper insights into the evolving research trends in ML for passive components and antenna design, Figure 0.1 highlights the increasing number of publications in recent years. The growing adoption of AI techniques in EM design underscores their potential to enhance automation and optimization in this field. Notably, publications

focusing on neural networks for EM component design are steadily increasing, while research on other methods has remained relatively stable (Arani, Shahidi & Zhang, 2024).

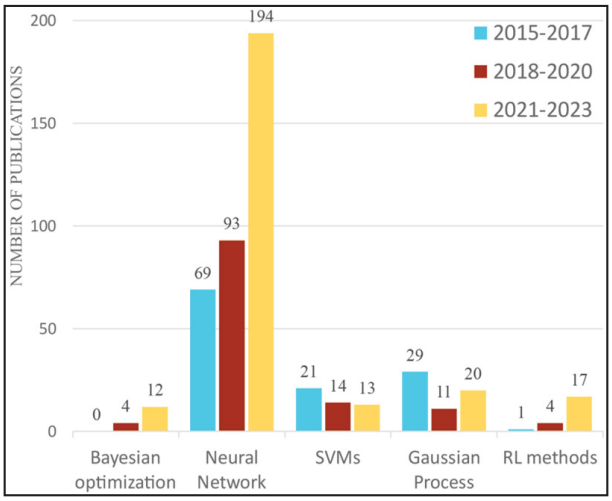

Figure 0.1 Publications on various ML-based methods in the EM field, including antennas and passive components such as filters and couplers, across different time periods, sourced from IEEE Xplore, ACM, Elsevier ScienceDirect, and Springer databases
Taken from Arani *et al.* (2024)

As AI techniques are increasingly used in EM structure design as shown in Figure 0.2, there are many chances to improve and use these methods in EM modeling and design. These opportunities include advanced reinforcement learning algorithms and innovative data generation techniques. Additionally, EM structure design inherently involves an inverse problem in performance analysis, making the use of inverse modeling for straightforward automatic design approaches to find the best solutions an exciting and promising area for future research (Karahan, Gupta, Khankhoje & Sengupta, 2022; Karahan, Shao & Sengupta, 2024b) and (Karahan, Liu & Sengupta, 2023).

As next-generation (Next-G) wireless technologies continue to advance, the integration of an increasing number of antennas and active and passive components within compact volumes poses significant challenges for emerging millimeter-wave (mm-wave) systems. The demand for high functionality, performance, and compact integration necessitates innovative design approaches. These systems comprise both radiative and non-radiative elements, as well as single-port and multi-port components, each governed by distinct design principles and geometric constraints. Furthermore, there is an increasing need for three-dimensional (3D) integrated, compact passive components and antennas to enable low-volume, cost-effective System-on-Package (SoP) modules with fully integrated hardware solutions (Xiao, Shao, Jin, Wang & Liu, 2021). In this context, achieving higher data throughput and improved signal integrity necessitates advanced antenna architectures and supporting technologies.

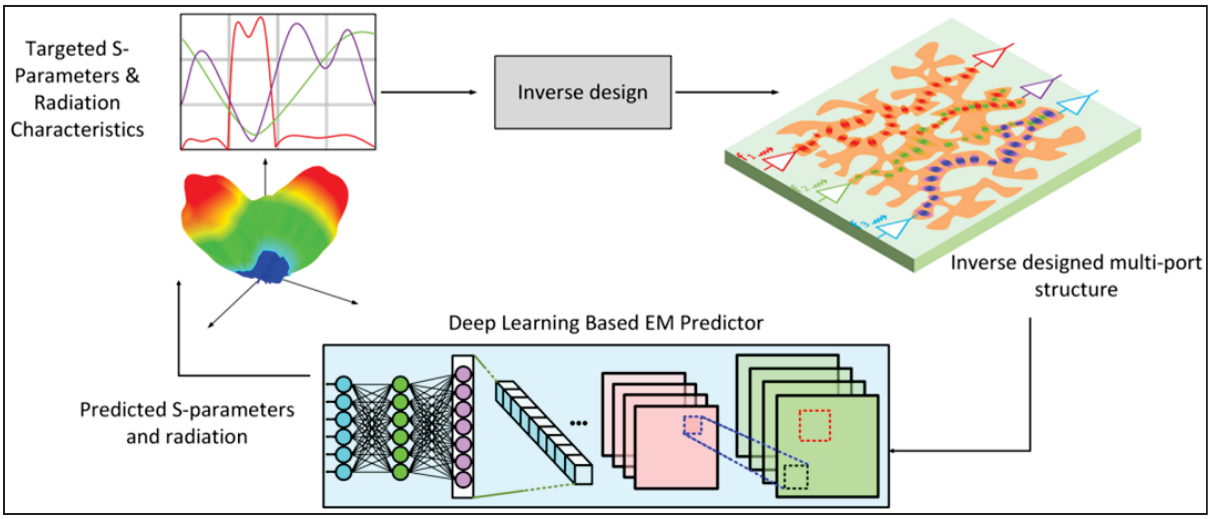

Figure 0.2 Overview of the Machine Learning-Based Inverse Synthesis Approach for Passive Components and Antennas
Taken from Karahan *et al.* (2024a)

Within the landscape of modern antenna technologies, massive multiple-input multiple-output (Massive-MIMO) has attracted significant attention for its potential to enhance spectral and energy efficiency. However, integrating a large number of antenna elements within a compact system presents substantial challenges. A primary concern is maintaining high isolation between elements and other active and passive components while ensuring optimal impedance matching, bandwidth, radiation characteristics, and efficiency. Moreover, achieving these performance metrics while minimizing cost, ensuring structural robustness, and facilitating ease of testing remains a critical challenge (Ali & Ibrahim, 2017; Qu, Piao & Kim, 2019; Swindlehurst, Ayanoglu, Heydari & Capolino, 2014).

To overcome these challenges, particularly at mm-wave frequencies, researchers have increasingly turned to alternative transmission line technologies. Among these, Gap Waveguide (GW) technology has emerged as a highly promising candidate, owing to its distinctive structural features and advantageous electromagnetic behavior.

Gap Waveguide (GW) technology is a highly promising transmission line solution for mmWave and sub-THz massive MIMO systems, as it combines the integration advantages of substrate-based technology with the superior power-handling capability and low-loss performance of traditional waveguides (Rajo-Iglesias, Ferrando-Rocher & Zaman, 2018b). Originally introduced by Kidal (Kildal, Alfonso, Valero-Nogueira & Rajo-Iglesias, 2009b; Valero-Nogueira, Baquero, Herranz, Domenech, Alfonso & Vila, 2011), GW is a metamaterial-based wave-guiding structure that leverages hard and soft boundary conditions to control electromagnetic wave propagation. Four different types of gap waveguides (GW) have been created and used in various antenna and passive component designs (Brazalez,

Zaman & Kildal, 2012b; Castillo-Tapia, Zetterstrom, Algaba-Brazález, Manholm, Johansson, Fonseca & Quevedo-Teruel, 2023; Pérez-Quintana, Bilitos, Ruiz-García, Ederra, Teniente-Vallinas, González-Ovejero & Beruete, 2023; Sharifi Sorkherizi & Kishk, 2017; Vosoogh, Sharifi Sorkherizi, Vassilev, Zaman, He, Yang, Kishk & Zirath, 2019a; Vosoogh, Zirath & He, 2019b), as shown in Figure 0.3. These are groove gap waveguide (GGW), ridge gap waveguide (RGW), printed ridge gap waveguide (PRGW), which is also called microstrip gap waveguide, and inverted microstrip gap waveguide (IMGW) (Yong, Vosoogh, Bagheri, Van De Ven, Hadaddi & Glazunov, 2023a).

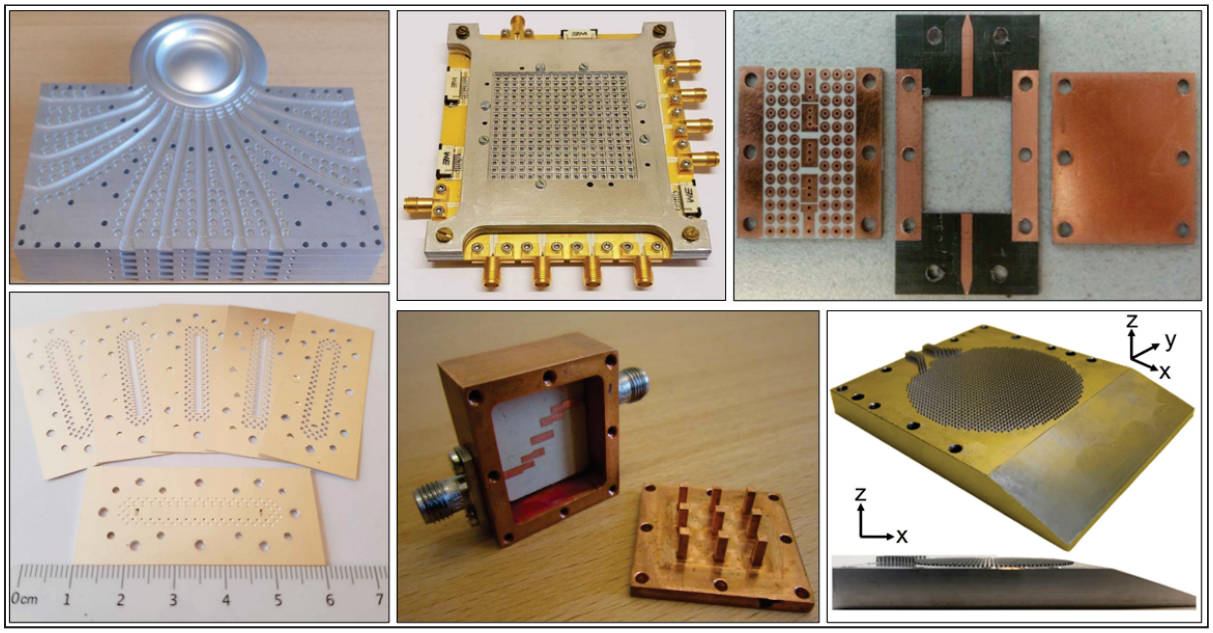

Figure 0.3 Examples of reported GW-based components
Taken from Brazalez *et al.* (2012b); Castillo-Tapia *et al.* (2023); Pérez-Quintana *et al.* (2023); Sharifi Sorkherizi & Kishk (2017); Vosoogh *et al.* (2019a,1)

The working principle of the GW is to guide the propagation of EM waves via a parallel-plate waveguide [Bayat-Makou & Kishk (2018b)]. Traditionally, a parallel-plate waveguide comprises two unconnected perfect electric conductor (PEC) plates, between which the EM wave propagates. However, when one of the PEC plates is replaced with perfect magnetic conductors (PMCs) at a separation distance of $\lambda/4$, the transmission of EM between them becomes impossible. This is due to the high surface impedance characteristics of the PMC, which cause a cutoff for all propagating modes across an air gap smaller than $\lambda/4$ (Shi, Feng, Qian, He, Zhou, Xue, Che & Wu, 2023).

Changing a segment in this PMC area to a PEC, which can be a ridge, groove, or strip, forces EM waves to follow the designated PEC pathway. Figure 0.4 illustrates the aforementioned concept. While current metallic materials

can approximate ideal PEC behavior to a certain extent, real PMCs do not naturally exist. However, they can be artificially engineered, often taking the form of an artificial magnetic conductor (AMC) or a high-impedance surface (Rajo-Iglesias & Kildal, 2011c).

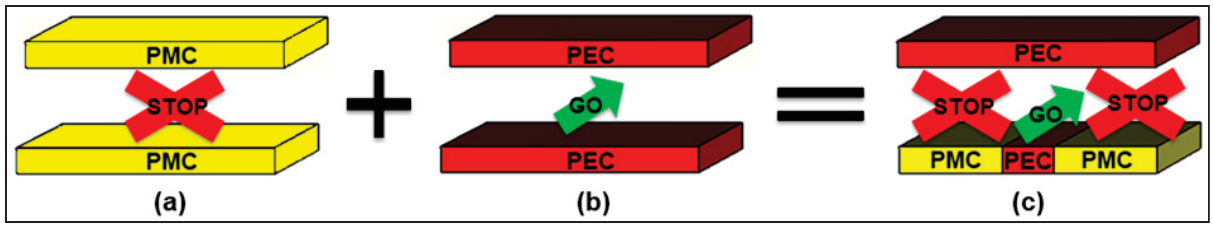

Figure 0.4 Basic working principle of the gap waveguide. (a) PEC-PEC Parallel-Plate Waveguide. (b) PEC-PMC Parallel-Plate with electromagnetic wave cut-off. (c) Concept of wave propagation in the gap waveguide

Clearly, AMC significantly influences the design of RGW. This is because the frequency range within which the local quasi-TEM mode can propagate as the single mode is defined by the presence of a stop band in the parallel-plate modes within that frequency range.

0.2 Problem Statement

In the most reported design process of an RGW unit cell, the engineer initially specifies the target stop-band frequency appropriate for their application. Subsequently, the dispersion diagrams that show the first three propagating modes are calculated and plotted. The obtained results give approximated and not accurate start and end frequencies of the stop band. Engineers then need to update these physical dimensions through many iterations (parametric studies) until the objectives are met. This approach is inefficient in terms of computational cost (Wei et al., 2023b; Zhou et al., 2024). This inefficiency arises from the complexity of the problem, which involves numerous variables, multiple objectives, and constraints that require several electromagnetic (EM) iteration steps.

To overcome this, some studies have proposed analytical solutions for calculating the dominant quasi-TEM mode in homogeneous RGW (Polemi & Maci, 2010b; Silveirinha, Fernandes & Costa, 2008b). A dispersion equation, which yields accurate results for the stop band in comparison to the CST Studio Suite eigenmode solver findings, has been used and generated. However, while the proposed closed formula for determining the band stop remains valid for particular unit cell parameters, the generalization has not been achieved.

Furthermore, from the perspective of RGW-based components, designing a compact, highly isolated, massive MIMO system with complex antenna and interconnection structures is computationally inefficient. As a result,

conventional design methodologies are becoming increasingly inadequate for addressing the growing complexity of RGW-and PRGW-based MIMO antennas in general, and the unit cell of RGW/PRGW in particular. This emphasizes the need for advanced modeling and design techniques.

Therefore, developing a fully automated design methodology for the RGW/PRGW unit cell, which serves as the core component of various RGW-based designs, would be highly advantageous.

0.3 Objectives and Contribution

Titled "A Machine Learning-Driven Synthesis Approach for Additively Manufactured Ridge Gap Waveguide Based Passive Components and Antennas," this doctoral thesis presents a four-year research endeavor aimed at overcoming the limitations of conventional design methodologies for RGW and PRGW components. The primary objective is to develop an intelligent, scalable, and fabrication-aware design framework that leverages machine learning (ML) techniques to automate and accelerate the synthesis of high-performance passive structures, with particular emphasis on compatibility with additive manufacturing technologies.

To concretize this vision, the research was guided by a set of well-defined objectives and resulted in several key contributions, as presented in the following subsections.

0.3.1 Objectives

The main research objectives are outlined as follows:

- To construct a comprehensive and scalable EM simulation dataset for RGW and PRGW unit cells, covering the 3–300 GHz range and accounting for geometric variations related to 3D printing, as well as dielectric material variations relevant to PRGW.
- To implement, benchmark, and optimize a suite of supervised machine learning models capable of accurately learning the forward and inverse mappings between geometric parameters and EM performance metrics of the unit cells.
- To develop a robust, fully automated, and computationally efficient ML-aided synthesis methodology for the design of complex RGW/PRGW-based microwave passive components and antenna arrays.

- To apply the proposed ML framework to the design of a compact, low-cost, highly isolated, and pattern-reconfigurable MIMO antenna system using 3D-printed PRGW structures and multi-permittivity dielectric resonators (DRs).

0.3.2 Contribution

The key scientific and technical contributions of this work are as follows:

- Introduction of the first unified, end-to-end ML-driven synthesis framework for metallic RGW and PRGW unit cells, enabling high-accuracy inverse design while reducing synthesis time from several hours or even days, as required by conventional full-wave techniques, to one minute after model training.
- Development and validation of a high-fidelity EM simulation dataset (3–300 GHz), enabling data-driven modeling and inverse design of 3D-printable RGW and PRGW unit cells—establishing a foundation for synthesizing complex passive components and MIMO antennas.
- The deployment of advanced ML models, including Genetic Programming (GP) and Artificial Neural Networks (ANN), for the inverse synthesis approach, with systematic evaluation based on metrics such as mean squared error (MSE), mean absolute error (MAE), mean absolute percentage error (MAPE), and synthesis computational time, to identify the most effective algorithm for each design scenario.
- The design, fabrication, and experimental validation of novel 3D-printed RGW and PRGW-based microwave components and MIMO antennas, featuring wideband operation, enhanced isolation, and reconfigurable radiation characteristics using low-cost additive manufacturing techniques.

0.4 Thesis Organization

This thesis is organized into individual chapters, each presenting the results of a distinct paper. The structure is outlined as follows:

CHAPTER ONE presents a comprehensive literature review and explores potential future developments. The main objective is to provide an overview of Ridge Gap Waveguide (RGW) technology, Additive Manufacturing (AM) technology, and their applications in passive component and antenna design. Next, we examine the latest advancements in machine learning (ML) techniques for passive component and antenna design. The chapter concludes by exploring research focused on the integration of ML with RGW and AM-based antenna designs.

CHAPTER TWO introduces, for the first time, an end-to-end ML framework for the automated and computationally efficient design of a fully metallic, 3D-printed back-to-back RGW structure, covering frequency bands from 3 to 300 GHz. We further extend this framework to design a highly isolated 90° bent 4-port RGW structure, demonstrating its adaptability to complex waveguide geometries, as presented in **CHAPTER THREE**.

CHAPTER FOUR proposes, for the first time, a scalable Genetic Programming (GP)-based approach for the synthesis of PRGW unit cells. This method enables the automated design of unit cells for any specified stop-band frequency within the 3–300 GHz range. The GP algorithm generates explicit mathematical expressions that predict PRGW unit cell dimensions based on predefined stop-band requirements and substrate materials. Compared to conventional trial-and-error methods and heuristic optimization techniques available in electromagnetic (EM) simulators, this approach significantly reduces computational time while achieving superior performance.

CHAPTER FIVE introduces a scalable Artificial Neural Network (ANN)-based inverse design approach for a newly shaped Defected Ground Structure (DGS) aimed at enhancing isolation in PRGW-based MIMO antennas. This approach facilitates the design of scalable MIMO systems, including configurations such as 4×4, 16×16, and higher-order arrays. The PRGW structure is designed using the results obtained in **CHAPTER FOUR**.

CHAPTER SIX applies the developed inverse design approach to create a low-cost, origami-inspired, compact 4×4 MIMO antenna, utilizing multi-permittivity dielectric resonators (DRs). This innovative design enhances antenna bandwidth and introduces a new, cost-effective radiation pattern reconfigurability concept in PRGW, offering a promising solution for next-generation wireless systems.

The thesis concludes by summarizing the work, highlighting the academic achievements, and discussing the limitations of the proposed contributions. Additionally, it suggests potential directions for future research.

0.5 Related Publications

As an outcome of this research, the following manuscripts were published:

- **Mohammed Farouk Nakmouche**, Dominic Deslandes, Mourad Nedil, and Ghyslain Gagnon, "Machine Learning-Aided Design of Defected Ground Structures for PRGW-Based MIMO Antennas," Accepted in IEEE Transactions on Antennas and Propagation.

- **Mohammed Farouk Nakmouche**, Dominic Deslandes, Ghyslain Gagnon, "Machine Learning-Aided Synthesis Approach for 3D Printed Ridge Gap Waveguides," under review in IEEE Transactions on Components, Packaging and Manufacturing Technology.

- **Mohammed Farouk Nakmouche**, Dominic Deslandes, Ghyslain Gagnon, "3D-Printed Metallic 90° Bent Ridge Gap Waveguide Structures: Enabling Compact Antenna and Passive Component Integration in CubeSats," under review in IEEE Antennas and Wireless Propagation Letters.

- **Mohammed Farouk Nakmouche**, Dominic Deslandes, and Ghyslain Gagnon, "Printed Ridge Gap Waveguide Synthesis Approach Based on Genetic Programming," under review in IEEE Journal on Multiscale and Multiphysics Computational Techniques.

- **Mohammed Farouk Nakmouche**, Dominic Deslandes, and Ghyslain Gagnon, Low-Cost Origami Printed RGW Wideband MIMO Antenna With Additively Manufactured Dielectric Resonator," under review in IEEE Transactions on Antennas and Propagation.

- **Mohammed Farouk Nakmouche**, Dominic Deslandes, Ghyslain Gagnon, George Xiao, and Jianping Lu," Fabry Perot Array Antenna Design Using Machine Learning," 2024 IEEE International Symposium on Antennas and Propagation and USNC-URSI Radio Science Meeting (AP-S/URSI), Florence, Italy, July 2024.

- **Mohammed Farouk Nakmouche**, Dominic Deslandes, Ghyslain Gagnon, George Xiao, and Jianping Lu, "Design of a Beam Reconfigurable Flexible SIW Slot Array Antenna Using ANN-Based Technique," 2024 IEEE International Symposium on Antennas and Propagation and USNC-URSI Radio Science Meeting (AP-S/URSI), Florence, Italy, July 2024.

- **Mohammed Farouk Nakmouche**, Dominic Deslandes, Ghyslain Gagnon, "Machine Learning Design Approach of 3D Printed Pixelated Lens MIMO Antenna for CubeSat," 2023 IEEE International Symposium on Antennas and Propagation and USNC-URSI Radio Science Meeting (AP-S/URSI), Portland, USA, July 2023.

- **Mohammed Farouk Nakmouche**, Dominic Deslandes, Ghyslain Gagnon, "Machine Learning Aided Design of Sub-Array MIMO Antennas for CubeSats Based on 3D Printed Metallic Ridge Gap Waveguides," 2022 IEEE Future Networks World Forum, October 2022.

- **Mohammed Farouk Nakmouche**, Dominic Deslandes, Ghyslain Gagnon, "Dual-Band 4-Port H-DGS Based Textile MIMO Antenna Design Using Genetic Algorithms for Wearable Application," 2022 IEEE International Symposium on Antennas and Propagation and USNC-URSI Radio Science Meeting (AP-S/URSI), Denver, CO, USA, 2022.

CHAPTER 1

LITERATURE REVIEW

This chapter explores Gap Waveguide (GW) technology and its different types used in antenna and passive component design. It presents a comprehensive literature review on integrating machine learning (ML) techniques in antenna design. Additionally, the chapter briefly overviews additive manufacturing (AM) technology, aligning with the thesis scope as the selected fabrication method.

1.1 Gap Waveguide Technology

Among the various transmission line technologies explored in the literature, gap waveguide (GW) has emerged as a promising alternative to microstrip lines (MSL) (Pozar, 2011) and substrate-integrated waveguides (SIW) (Deslandes & Wu, 2001). GW technology minimizes propagation attenuation by eliminating dielectric losses, offering a lower insertion loss than MSL and SIW (Berenguer, Fusco, Zelenchuk, Sánchez-Escuderos, Baquero-Escudero & Boria-Esbert, 2016a). Furthermore, its non-contact vertical metallic walls alleviate fabrication constraints, enabling efficient implementation at higher frequencies (Shi, Feng & Cao, 2021c). The key advantages of GW over conventional waveguide technologies, including SIW and microstrip waveguides (Yong, Vosoogh, Bagheri, Ven, Hadaddi & Glazunov, 2023b), are summarized below and illustrated in Figure 04, which presents the trade-offs among loss, fabrication complexity, and cost in guided wave technologies.

1.1 illustrates the comparative positioning of microstrip lines, SIW, and metallic waveguides in terms of transmission loss, fabrication complexity, and cost. MSL technology, while cost-effective and simple to fabricate, suffers from high transmission losses due to dielectric dissipation. Metallic waveguides, in contrast, exhibit minimal loss but require complex and costly fabrication processes. SIW provides an intermediate solution, mitigating some loss while maintaining manufacturability. However, a noticeable ‘performance gap’ remains, as indicated in the figure, highlighting the need for an alternative approach. GW technology addresses this gap by offering low-loss propagation while avoiding the fabrication challenges associated with metallic waveguides, making it a promising alternative for high-frequency applications.

- Lower losses due to the elimination of dielectric materials, minimizing propagation attenuation.
- Cost efficiency, as the absence of conducting joints simplifies manufacturing and reduces production costs.
- Self-packaging capability, allowing straightforward assembly without additional enclosures.
- Seamless integration of active components, enhancing overall system performance.

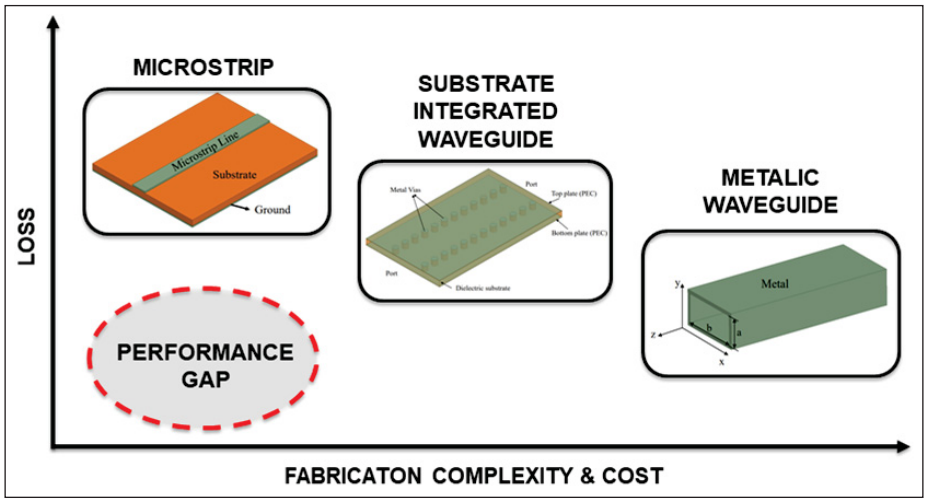

Figure 1.1 Trade-Off Between Loss, Fabrication Complexity, and Cost in Guided Wave Technologies

As discussed earlier, AMC structures play a crucial role in GW technology by enabling bandstop behavior within the targeted frequency range. As illustrated in 1.2, these structures can be realized as fully metallic designs (e.g., GGW and RGW) or substrate-integrated configurations (e.g., PRGW and IMGW). Each technology structure presents distinct advantages and limitations concerning fabrication complexity, compactness, power-handling capacity, integration feasibility, and electromagnetic performance, among other critical factors (Rajo-Iglesias, Ferrando-Rocher & Zaman, 2018a). Table 1.1 provides a comparative analysis of GW technology structures based on key performance metrics such as transmission loss, bandwidth, and ease of manufacturing.

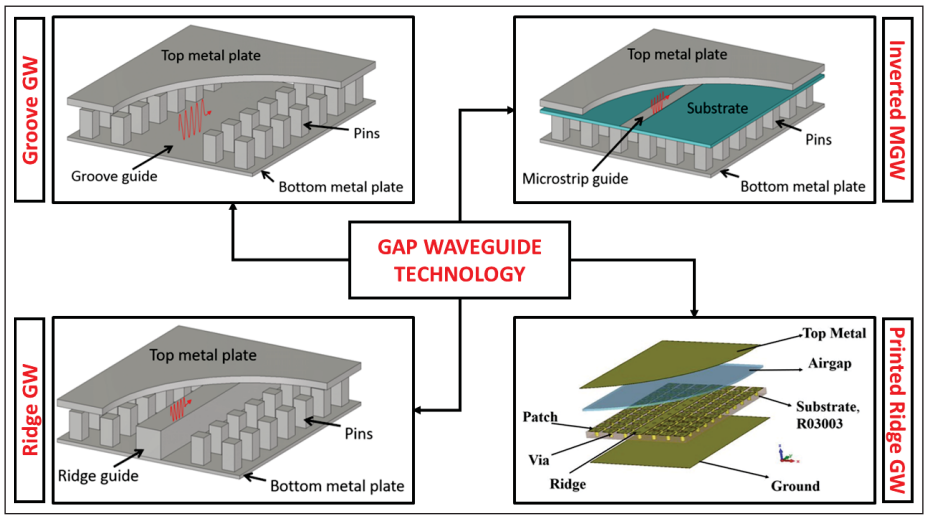

Figure 1.2 Classification of Gap Waveguide (GW) Technology Types.

Table 1.1 Comparative Analysis of Gap Waveguide (GW) Technology Types

Legend: ∗ = Average, ∗∗ = Favorable, ∗ ∗ ∗ = Highly Favorable, ∗ ∗ ∗∗ = Very Favorable.				
GW Transmission Line Structures	**GGW**	**RGW**	**SIGW**	**IMGW**
Fundamental Mode	TE_{10}	Q-TEM	Q-TEM	Q-TEM
Transmission Loss	∗∗	∗ ∗ ∗	∗ ∗ ∗∗	∗ ∗ ∗∗
Monomode Bandwidth	∗ ∗ ∗	∗ ∗ ∗	∗ ∗ ∗∗	∗ ∗ ∗∗
Physical Size	∗	∗ ∗ ∗	∗ ∗ ∗∗	∗ ∗ ∗∗
Ease of Manufacturing	∗ ∗ ∗∗	∗ ∗ ∗∗	∗∗	∗
Integration	∗ ∗ ∗∗	∗ ∗ ∗∗	∗ ∗ ∗∗	∗ ∗ ∗∗
Packaging and Shielding	∗ ∗ ∗∗	∗ ∗ ∗∗	∗ ∗ ∗∗	∗∗

1.1.1 State-of-the-Art: Gap Waveguide-Based Antenna Design and Passive Component Design

Due to the limitations of conventional transmission line technologies, researchers have investigated GW-based antennas and passive components, leveraging their superior performance advantages. To provide a comprehensive overview of these advancements, the following subsection examines key developments in GW-based antenna and passive component design.

1.1.1.1 GW-Based Antenna

The initial GW antenna design integrated four slots into the RGW structure, operating at 13 GHz (Zaman & Kildal, 2014). To support different array configurations, two distinct feeding mechanisms were employed: a linear feed for a 1×4 array and a corporate feed for a 2×2 array. These feeding strategies were specifically developed to enhance power distribution and improve radiation performance.

Building on the concept of slot integration within RGW structures, subsequent research extended this approach to higher-frequency bands. For instance, in (Vosoogh & Kildal, 2016), a V-band slot array antenna operating in a fully metallic configuration was introduced, employing RGW technology with an 8×8 array layout. The design incorporates a multi-layered structure composed of three separate, unconnected layers: the radiating slot layer, the cavity layer based on GW technology, and the feeding layer, which utilizes RGW principles.

While the aforementioned V-band slot array utilizes a multi-layered structure, an alternative approach focuses on wideband patch antennas fed by RGW. In (Zarifi, Farahbakhsh & Zaman, 2017), a wideband patch antenna is employed to realize an 8×8 array operating at 60 GHz, achieving an array efficiency exceeding 75% across the entire operational bandwidth. Similarly, in (Sadri-Moshkenani, Rashed-Mohassel & Shahabadi, 2018), a comparable design approach is utilized, substituting the RGW with Gap Waveguide (GGW) while preserving the fundamental principles and exploring an alternative feeding structure.

The integration of GW technology with microstrip patch antennas effectively reduces feeding losses and suppresses unwanted surface waves. Unlike conventional rectangular waveguides, GW technology can be seamlessly co-designed with microstrip patch antennas, resulting in substantial enhancements in overall antenna performance.

Among the various implementations of GW-based antennas, PRGW has emerged as a widely adopted technology for microstrip antenna development. Numerous PRGW-based designs have been realized, incorporating diverse radiating elements such as magnetoelectric (ME) dipoles (Ali, Afifi & Sebak, 2020a; Sorkherizi, Dadgarpour & Kishk, 2017), spiral antennas (Baghernia, Ali & Sebak, 2020; Baghernia, Movahedinia & Sebak, 2021), and metasurface antennas (Li & Chen, 2020). These designs underscore the versatility of PRGW technology, showcasing its broad applicability in enhancing the performance and functionality of microstrip antennas.

Beyond microstrip configurations, GW technology has also been explored for enhancing horn antennas, a fundamental component in microwave applications for over 70 years. Horn antennas are well known for their broad bandwidth, high gain, and low-loss characteristics. Traditionally, these antennas are fed through a waveguide, typically fabricated from a perfect electric conductor (PEC). However, manufacturing conventional horn antennas, particularly at higher frequencies, presents significant challenges due to compact dimensions, stringent fabrication tolerances, and the necessity for precise electrical contacts.

Recent advancements have introduced key design concepts for various GW-based horn antennas, incorporating different GW technologies such as PRGW (Bayat-Makou & Kishk, 2017) and Gap Waveguide (GGW) (Hamedani, Oraizi, Amini, Zarifi & Zaman, 2020; Mohammadpour, Mohajeri & Razavi, 2022). Notably, much of the existing research has concentrated on 2D planar configurations, emphasizing an important developmental direction for GW-based horn antennas.

Although significant research has been devoted to 2D planar GW-based horn antennas, design constraints have largely confined these to H-plane configurations. Addressing this limitation, the study in (Cao, Li, Wang, Sun & Ge, 2021) introduced an innovative 3D dual-polarized pyramidal horn antenna. This design utilizes a 3D GW orthomode transducer (OMT) based on PRGW technology. The resulting 3D pyramidal horn with OMT achieves a bandwidth of approximately 28% at 31 GHz. Unlike conventional horn antennas that require intricate fabrication processes to ensure proper electrical connections, the GW-based horn antenna is realized through a layered assembly approach, eliminating the need for complex electrical contacts. This streamlined fabrication method significantly reduces production costs while maintaining high performance.

1.1.1.2 GW-Based Passive Components

Given the structural similarities between GW configurations and conventional transmission-line technologies—such as rectangular waveguides, SIW, and MSL researchers have increasingly explored GW technology for the design and implementation of passive components.

One of the earliest applications of this technology was the development of a GW-based filter, realized using an IMGW structure that integrated the conventional microstrip parallel-coupled technique. Positioned between metallic AMC pins and a PEC metallic plate, this filter was specifically designed for Ku-band applications (Brazalez, Zaman & Kildal, 2012a). Expanding on this approach, a similar methodology was later employed to develop a fourth-order bandpass filter for V-band applications (Vosoogh, Brazález & Kildal, 2016), where an end-coupled mechanism replaced the parallel-coupled approach. Further extending the scope of GW technology, multiple filters have been implemented using SIGW structures (Sorkherizi & Kishk, 2017)-(Chen, Shen, Zhang & Sa, 2021). However, despite their design flexibility, both IMGW and SIGW filters tend to exhibit higher insertion loss due to the inherent presence of the dielectric substrate.

To address this challenge, researchers have increasingly turned to GGW and RGW structures, which offer improved wave confinement and reduced dielectric-related dissipation [(Horestani & Shahabadi, 2018)]. These advancements have enabled the successful engineering of GW-based filter topologies across a broad frequency spectrum, ranging from the X-band to the D-band.

Beyond filters, GW technology has also facilitated the design of advanced diplexers. For instance, an X-band diplexer was developed using two GGW-based fourth-order Chebyshev filters, designated for transmission and reception (Farahani, Sadeghzadeh, Gharanfeli & Kishk, 2017). This design achieves a bandstop attenuation exceeding 20 dB while maintaining an insertion loss of approximately 1.5 dB within the passband. Encouragingly, this approach has been extended to higher frequency bands, including Ku-band (Zarifi, Shater, Ashrafian & Nasri, 2018), Ka-band (Vosoogh, Sorkherizi, Zaman, Yang & Kishk, 2018), and E-band (Rezaee & Zaman, 2017). Additionally, a Ka-band diplexer employing an IMGW filter (Sanchez-Cabello, Herran & Rajo-Iglesias, 2020) demonstrates a passband insertion loss of approximately 2 dB while achieving over 20 dB attenuation in the stopband.

1.1.1.3 Challenges and Research Gaps

Despite promising studies in the literature, the design of RGW remains computationally expensive and inefficient, primarily due to its reliance on the unit cell (i.e., the AMC). This inefficiency arises from the complexity of the design process, which involves numerous variables, multiple objectives, and constraints, necessitating extensive

EM simulations. These challenges highlight the need for advanced ML-based modeling and design approaches, presenting a promising research direction that requires further exploration.

1.2 Machine Learning-Aided Antenna Design Approach

Microwave modeling and simulation are critical steps in the development of novel antenna and passive component designs. Traditionally, engineers have relied on EM simulation software, such as HFSS and CST Studio, which utilize integral and differential equation-based methods refined over the past century. These tools enable accurate assessment of antenna and passive component behavior prior to fabrication, reducing design iterations and development costs. However, as design complexities grow and computational demands increase, alternative approaches based on ML have emerged to overcome the limitations of conventional methods, offering faster predictions and enhanced optimization capabilities.

AI has recently emerged as a powerful tool in automatic antenna design and behavior prediction, offering the potential to significantly accelerate the design process while maintaining high accuracy. By leveraging AI-driven techniques, researchers have introduced novel approaches aimed at minimizing computational resource usage, particularly in terms of memory and CPU efficiency (Balanis, 2005; Bhartia, Ittipiboon, Garg & Bahl, 2001; W & A, 2006; Zhang, Lin, Zhang & Li, 2019a). These advancements address the growing challenges posed by conventional EM simulations, making AI an increasingly viable tool for complex antenna design tasks.

Expanding on this trend, researchers have increasingly leveraged AI-driven approaches for antenna modeling in microwave engineering, particularly due to its ability to handle the complex nonlinear relationships between key performance parameters such as S-parameters, gain, radiation efficiency, and directivity (Zhang, Gupta & Devabhaktuni, 2003b). In fact, AI-based methods have proven to outperform traditional EM simulators in terms of accuracy and computational efficiency (Shi, Zhang, Zhang, Yi & Liu, 2021a). However, the effectiveness of AI-based modeling is intrinsically tied to the availability and quality of training data. As more data is provided, ML algorithms can develop increasingly accurate models, refining their predictive capabilities.

Despite these advantages, a major challenge in applying ML to microwave engineering is the lack of standardized datasets, unlike well-established fields such as computer vision. This necessitates the generation of high-quality datasets through conventional EM simulation software, such as HFSS and CST, ensuring robust and reliable ML training (Misilmani, Naous, Khatib & Salwa, 2020a).

To address this gap, this research introduces a novel dataset specifically tailored for GW-based antenna and passive component design. Given the absence of standardized datasets in this field, our work provides a structured and high-quality dataset that can serve as a benchmark for future studies. This dataset, generated through extensive EM simulations in CST and HFSS, captures the complex relationships between geometric parameters, electromagnetic

performance metrics, and fabrication constraints. By making this dataset available, we aim to advance data-driven methodologies in microwave and antenna engineering, facilitating more efficient and accurate ML-based design processes.

To systematically apply ML in microwave engineering, the approach typically follows three key stages, each playing a crucial role in ensuring the effectiveness and accuracy of the final model, as illustrated in Figure 1.3:

1. **Data Generation:** Firstly, a database of inputs and outputs is created using EM simulation software. In our research project, we employ Visual Basic for Applications (VBA) macro programming in HFSS and CST Microwave Studio to automate the design and simulation process, resulting in the automated generation of the dataset.

2. **Training and Validation:** Once a comprehensive dataset has been generated, the next critical step involves training, testing, and validating the ML model to ensure its ability to accurately predict antenna behavior. For this step, we use a Python program based on the Scikit-Learn, PyTorch, and Keras libraries to carry out the training, testing, and validation of our ML model.

3. **Model Evaluation and Optimization:** Following successful training and validation, the focus shifts to evaluating and optimizing the best-performing ML model. This final step ensures that the model is not only accurate but also robust enough for practical antenna design applications. In this step, we begin by evaluating the implemented ML models using statistical metrics such as the mean squared error (MSE), Mean Absolute Percentage Error (MAPE), and the regression value R^2.

1.2.1 State-of-the-Art: Machine Learning Application in Antenna Design and Optimization

Building upon the advantages of ML in microwave engineering, recent studies have extensively explored its applications in automating various aspects of antenna design. Researchers have leveraged different ML techniques to optimize antenna parameters, improve prediction accuracy, and reduce computational costs, demonstrating significant advancements in performance and efficiency.

One prominent example is the use of Support Vector Regression (SVR) and Artificial Neural Networks (ANNs) for predicting the positions and sizes of asymmetrical/symmetrical slots in a classical rectangular microstrip antenna (Khan & Roy, 2019). Comparative analysis revealed that SVR outperformed ANN, achieving 10% higher accuracy and 416 times faster computation.

Similarly, in (Khan, De & Uddin, 2013), ML models were employed to determine the optimal size of a slotted patch antenna and its substrate air gap dimension based on resonance frequency, gain, and directivity. By testing various ANN training algorithms, the study demonstrated that ML approaches can yield optimal results with

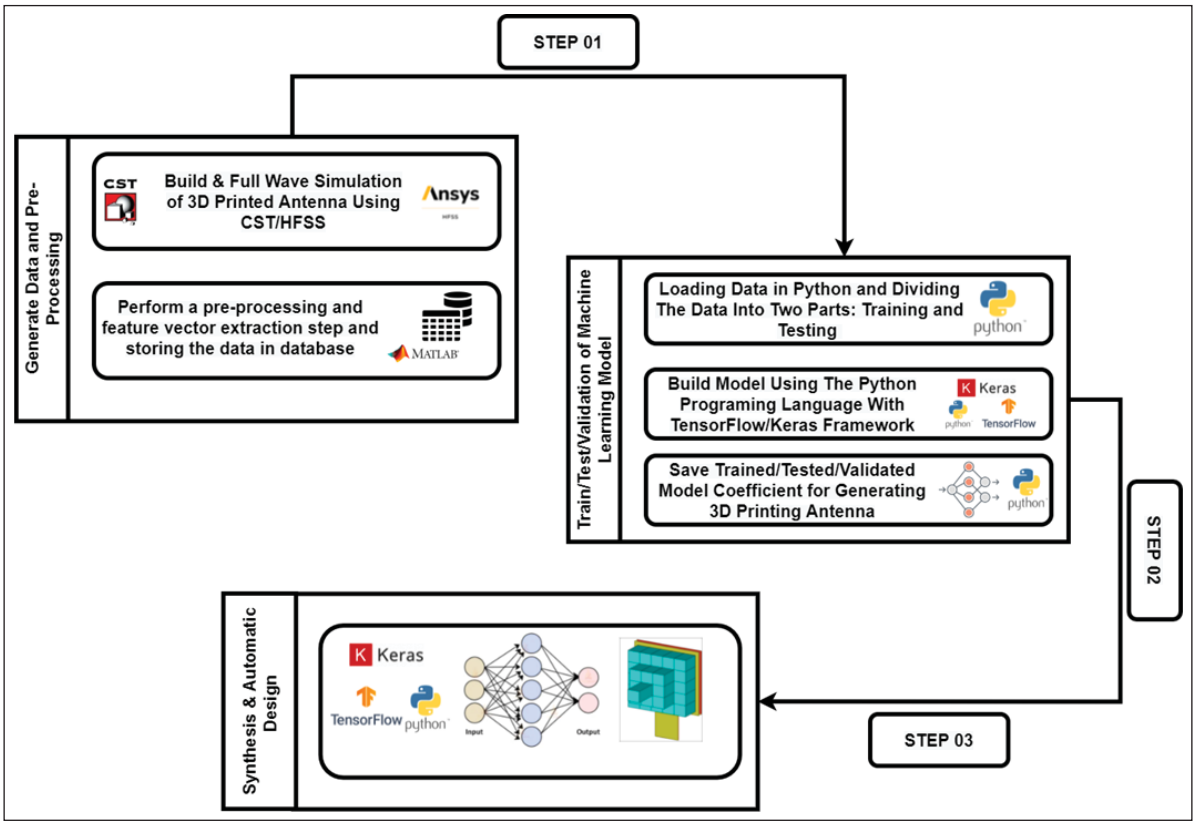

Figure 1.3 Overview Steps of Machine Learning-Based Design Approach

minimal training time and iterations. Moreover, experimental validation showed a negligible prediction error of 0.208%, underscoring the precision of the proposed model. This research builds upon prior work (Sharma, Wu, Xin & Zhang, 2017), where Least Absolute Shrinkage and Selection Operator (LASSO) was applied with an optimization function targeting the fractional bandwidth (FBW) of two reference antenna bands.

Expanding on this, (Sharma, Zhang & Xin, 2020b) investigated the effectiveness of LASSO, ANN, and k-nearest neighbor (k-NN) algorithms in predicting the FBW of a dual-band double T-shaped monopole antenna. By analyzing 2,126,696 design points while training on only 450 samples, the study found that ANN and LASSO outperformed k-NN, which had an error rate of 2.90%.

Beyond classical ML models, hybrid approaches integrating ANN with optimization algorithms have shown promising results. Studies in (Jain, Patnaik & Sinha, 2011; Jain, 2016; Jain, Patnaik & Sinha, 2013; Patnaik & Sinha, 2011)] utilized a trained ANN combined with Particle Swarm Optimization (PSO) to achieve multi-band characteristics for a stacked patch antenna. The methodology involved using PSO to determine the optimal antenna geometrical parameters, followed by an ANN-based black-box function to predict frequencies and bandwidths. Experimental validation confirmed the effectiveness of the model, yielding an error on the order of 10^{-5} GHz.

In parallel, Support Vector Machines (SVMs) have been investigated in (Martinez-Ramon & Christodoulou, 2006; Zheng, Chen & Huang, 2011) for designing rectangular microstrip antennas, patch arrays, and linear/nonlinear beamforming techniques, demonstrating their robustness in handling complex antenna design problems.

Another innovative approach is found in (Dadashzadeh, Kargar, Torabi & Rahmati, 2016), where a clustering method was used to optimize the placement of a shorting post in a microstrip patch array antenna. This ML-based technique successfully identified configurations that optimize bandwidth, scan angle, and polarization.

The potential of deep learning techniques is highlighted in (Nan, Xie, Gao, Song & Yang, 2021a), where a hybrid deep belief network (DBN) combined with PSO was employed for designing a fractal ultra-wideband (UWB) MIMO antenna. Compared to conventional modeling methods trained on the same dataset, this approach demonstrated superior feature learning and nonlinear function approximation, achieving a prediction error of 11.87% and 3.56% for single-element and MIMO antennas, respectively.

Lastly, a fast ML-based approach for synthesizing dielectric-filled Slotted Waveguide Antennas (SWAs) has been proposed in (Naous, Merie, Khatib, Al-Husseini, Shubair & Misilmani, 2022). By leveraging ML algorithms, researchers successfully predicted slot lengths and displacements required for a given resonance frequency, reflection coefficient, and Sidelobe Level Ratio (SLR). This method surpassed both CST simulations and genetic algorithms (GA) in terms of computation time and antenna performance, demonstrating its potential for real-world applications.

1.2.1.1 Challenges and Research Gaps

Overall, these studies illustrate the growing role of ML in enhancing antenna design automation, offering superior performance in terms of prediction accuracy, computational efficiency, and optimization capability. Despite these advancements, existing research has predominantly focused on conventional antennas fabricated using standard PCB techniques, limiting the exploration of ML's full potential in more advanced electromagnetic structures, including those developed through Additive Manufacturing (AM). Notably, no prior work has specifically explored the design and optimization of GW-based structures, revealing a critical gap in the literature.

1.3 Additive Manufacturing (AM) Technology

The advancement of AM technologies is transforming the electronics industry by unlocking the potential of advanced 3D and 4D printing. These innovations enable the development of highly integrated and complex 3D antennas and passive components. AM is projected to drive substantial industrial growth, with market valuations expected to range between $40 billion and $50 billion by 2028 as shown in Figure 1.4 (Atlantic Council, 2011; Bower & Christensen, 1995).

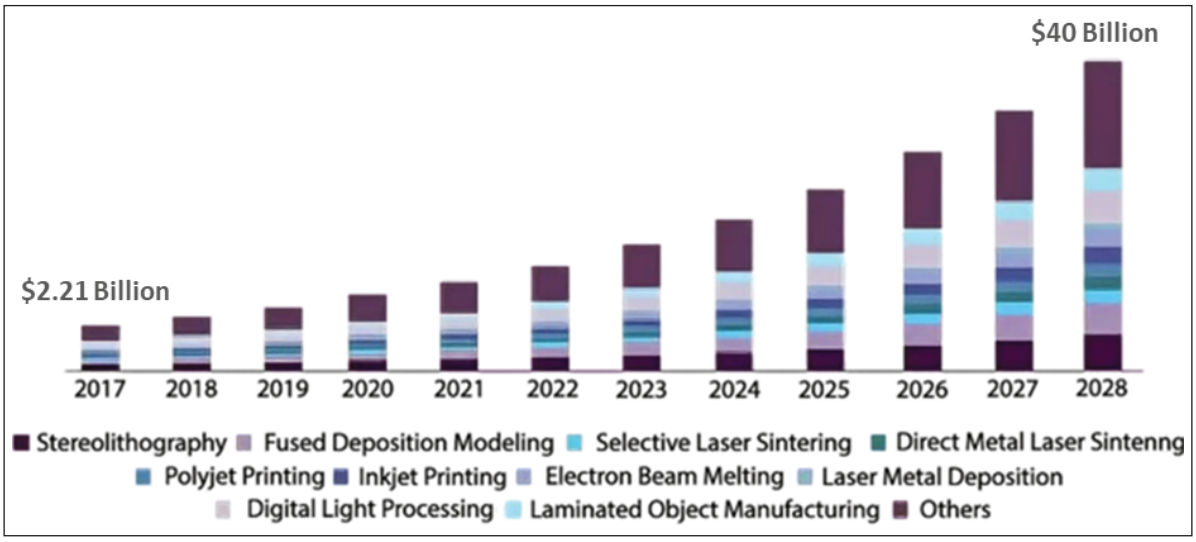

Figure 1.4 North America's Additive Manufacturing Market Growth by Technology (2017–2028) (US$ Billion)
Taken from Atlantic Council (2011)

Future 3D/4D-printed communication systems will integrate electronic components with intricate geometries, incorporating origami or shape-memory structures using emerging dielectric and conductive multi-materials. However, this advancement presents a significant challenge due to the absence of an efficient and systematic design methodology tailored to these unique geometric freedoms. To bridge this gap, a novel approach is required to minimize computational costs and ensure time-efficient design processes. Such an approach is crucial for optimizing circuit performance while accelerating the development cycle.

Compared to traditional manufacturing methods, such as subtractive and formative techniques, AM offers antenna designers greater freedom to create complex geometries and achieve enhanced compactness (Gibson, Rosen & Stucker, 2010). This capability surpasses the limitations of conventional fabrication techniques. Furthermore, AM has become increasingly attractive for researchers and designers due to its key advantages:

- **Reduced Waste:** AM minimizes material waste by using only the necessary amount to construct a part, ensuring a more efficient manufacturing process. In contrast, traditional methods, such as computer numerical control (CNC) milling, remove excess material from a larger block, generating substantial waste.
- **Accelerated Manufacturing:** AM significantly reduces production time by streamlining material usage and fabrication processes. While conventional methods may require days or weeks to manufacture a prototype, AM typically completes this process within hours.

- **Capability to Fabricate Complex Structures:** AM's layer-by-layer process enables the creation of intricate designs that would be challenging or impossible to produce using traditional techniques. This capability fosters innovation and enhances component performance.

AM encompasses a range of technologies, each suited to specific materials, applications, and fabrication processes. The selection of an appropriate AM technique depends on factors such as material properties, resolution requirements, and intended application. The following subsections outline widely used AM technologies, emphasizing their advantages and suitability for RF and microwave applications.

1.3.1 Types of Additive Manufacturing Technologies

In 1986, Charles Hull patented the first additive manufacturing (AM) system, the Stereolithography Apparatus (SLA), later commercialized by 3D Systems (Jacob, 1992). This breakthrough led to the development of the Stereolithography (STL) file format, now the standard for most CAD-based AM systems. Figure 1.5 illustrates a typical AM process. The process begins with creating a 3D model using computer-aided design (CAD) software. This model is then sent to a 3D printer, which reconstructs it layer by layer using the selected material (Rasiya, Shukla & Saran, 2021). Post-processing steps, such as drying, polishing, electroplating, or coating, may be required depending on the material and design specifications.

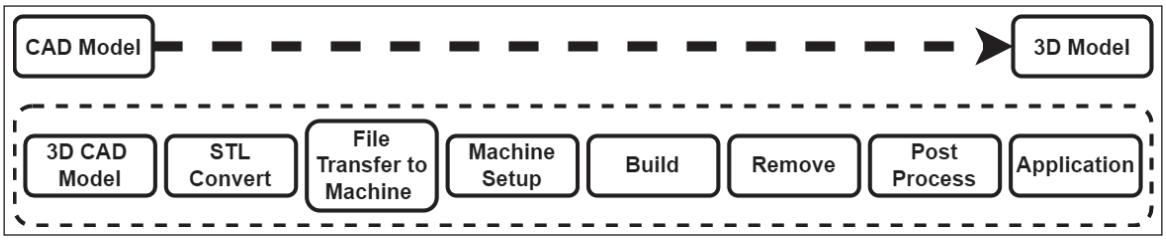

Figure 1.5 The Fundamental Additive Manufacturing Process
Taken from Rasiya *et al.* (2021)

Building upon the foundation laid by SLA, several other AM technologies have emerged, each with distinct material compatibility and fabrication methodologies. These include 3D Printing, Fused Deposition Modeling (FDM), Prometal, Direct Metal Laser Sintering (DMLS), Electron Beam Melting (EBM), Laminated Object Manufacturing (LOM), and PolyJet. AM technologies are generally classified into solid-based, liquid-based, and powder-based methods.

Among these classifications, liquid-based technologies have gained significant traction due to their precision and material flexibility. One such method, Inkjet Printing Technology, offers a low-cost, versatile approach to direct writing fabrication.

1.3.2 Inkjet Printing Technology

Inkjet printing technology, developed by a research group at the Massachusetts Institute of Technology (MIT) in the early 1990s, is a low-cost, flexible direct writing process that enables printing onto various substrates without the need for photomasks (Hon, Li & Hutchings, 2008; Kawase, Moriya, Newsome & Shimoda, 2005; Shah, Lee, Lee & Hur, 2021; Singh, Haverinen, Dhagat & Jabbour, 2010a,1). The process begins by designing a 3D model using 3D CAD software, which is then directly printed onto the selected substrates. This method reduces both printing time and material consumption. Figure 1.6 illustrates a typical drop-on-demand (DOD) inkjet printing workflow, where ink droplets are ejected from the printing nozzle to form both 2D and 3D structures. The 3D model is built through the non-contact deposition of ink droplets onto the substrate.

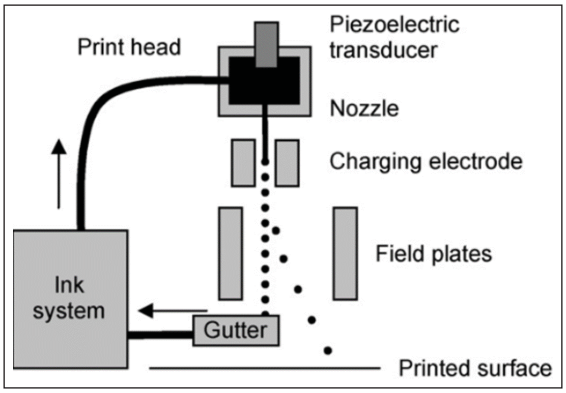

Figure 1.6 Inkjet Printing Technology Working Process Singh *et al.* (2010a)

While Inkjet Printing relies on the deposition of ink droplets to form structures, other liquid-based techniques, such as SLA and DLP, leverage photopolymerization to achieve high-resolution prints with precise material curing.

1.3.3 Stereolithography (SLA) / Digital Light Processing (DLP) Technology

Stereolithography (SLA) and Digital Light Processing (DLP) are both based on photopolymerization, a process in which a light source solidifies liquid photosensitive resin into a solid object (Gross, Erkal, Lockwood, Chen & Spence, 2014; Hull, 1986; Xu, Wu, Guo, Kong, Zhang, Qian, Mi & Sun, 2017). The basic processes of SLA and DLP are illustrated in Figures 1.7 and 1.8.

Each of these two systems (SLA and DLP) uses photopolymerization, but the difference is that in SLA, the 3D model is printed with a laser beam, while in DLP the 3D model is printed layer by layer with a digital projector screen (Kruth, Leu & Nakagawa, 1998). The very small size of the optical spot on a laser beam or a digital projector screen is a key part of figuring out the printing resolution.

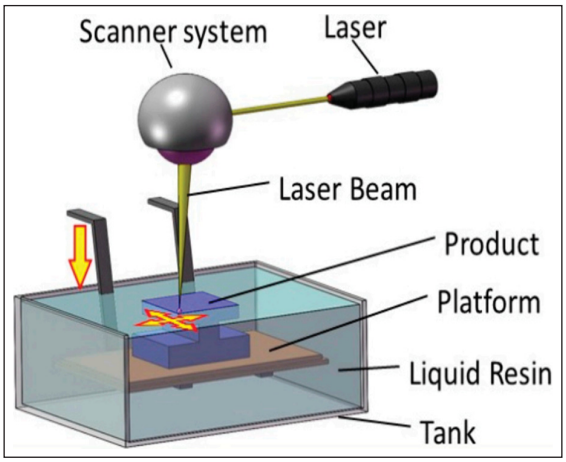

Figure 1.7 Stereolithography Technology

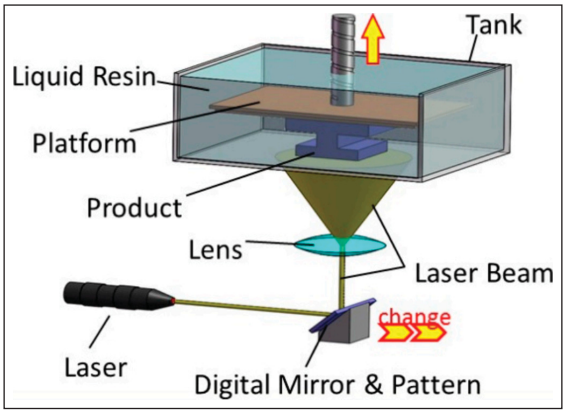

Figure 1.8 Digital Light Processing Technology

1.3.4 Fused Deposition Modelling (FDM)/ Fused Filament Fabrication (FFF) technology

The FDM/FFF technique is better suited for low-cost personal 3D printer machines that use plastic filaments to build the 3D model on a printed bed. The filament material is fed into the extrusion head, which melts it using a heated extrusion head set to the proper temperature. Extruded filament spreads onto the build surface once it has been melted. The model is built by moving the extrusion head vertically and horizontally across the build platform, depositing the heated filament material layer by layer. This procedure is repeated till the 3D model is fully built. The FDM/FFF process is depicted in Figure 1.9 (Song, Wang, Huang & Tsung, 2014; Tong, Joshi & Lehtihet, 2008).

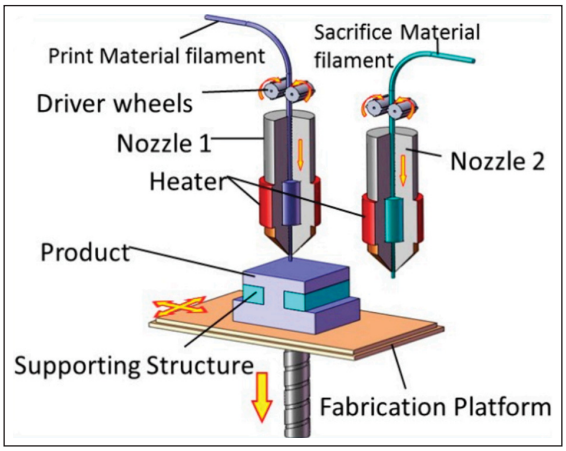

Figure 1.9 FDM & FFF Workflow

1.3.5 Selective Laser Sintering (SLS) / Selective Laser Melting (SLM) technology

The SLS/SLM technique uses laser energy to heat and solidify material powder layer by layer, leading to a turn of a powder into a form with the necessary size and shape (Jun). SLS/SLM can use a variety of materials for 3D part manufacturing such as plastics, metals, polymers, ceramics, and their combinations. It is more efficient for complex shapes than FDM/FFF and FDM/FFF (Bertrand, Bayle, Combe, Goeuriot & Smurov, 2007; Ferrage, Bertrand, Lenormand, Grossin & Ben-Nissan, 2017; Juste, Petit, Lardot & Cambier, 2014; Kruth, Levy, Klocke & Childs, 2007)]. The workflow procedure for SLS/SLM is depicted in Figure 1.10.

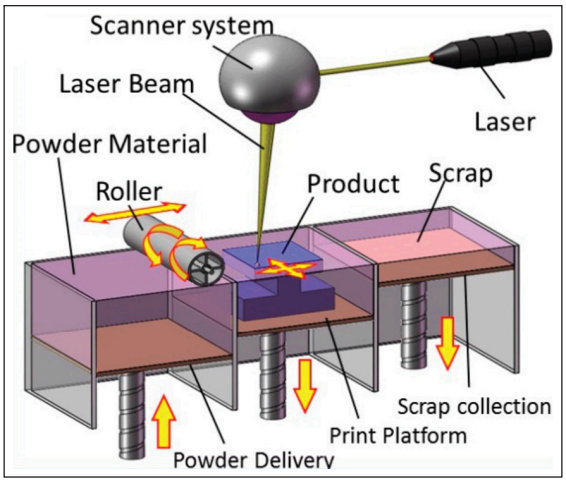

Figure 1.10 Working Process of SLS and SLM Technology

From a designed 3D CAD model, the building platform in the 3D printer machine is increased by a layer of powder on the z-axis each time. The powder layer is evenly spread out by a roller or a blade in the 3D printer machine. After

that, the targeted area of the layer is heated by a carbon dioxide laser beam, which sinters (SLS) or melts/fusions (for SLM) the desired area, and finally, a laser beam is used to selectively sinters (SLS) or melts/fusions (for SLM) the particles of the powder bed. As the building platform descends by a layer thickness on the z-axis, a fresh layer of powder is spread over the surface of the previous layer. Thus, a new layer is added on top of the previously deposited one. This process is repeated layer by layer until the 3D model is done.

1.3.6 Photopolymer Jetting (Ployjet) technology

This method based on the use of photosensitive resin printing material was first introduced by Gothait (Gothait, Peleg & Baharav, 2001). As shown in Figure 1.11, the inkjet nozzle deposits printing material on a mobile platform, which is then cured by UV light and solidified. Different materials and colors can be used at the same time. Because of its high resolution, the Ployjet is ideal for printing very small and sensitive parts, with the drawback of having weak strength. Polyjet is a layer-by-layer process that builds a 3D model after curing all of the model's layers.

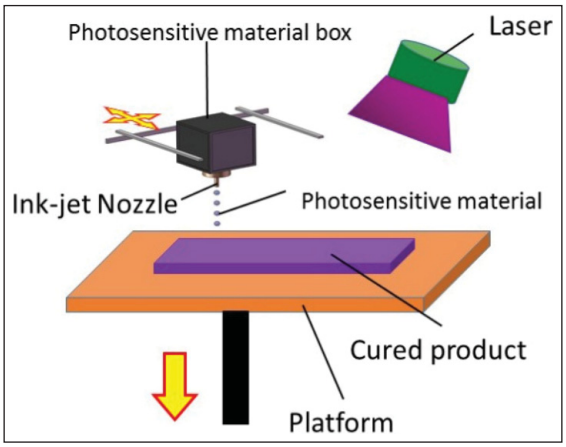

Figure 1.11 The Working Process of Ployjet Technology
Taken from Gothait *et al.* (2001)

1.3.7 Binder Jetting (3DP) technology

The 3D model is created by depositing a special adhesive from an inkjet nozzle onto thin layers of powder, which then join together to form a solid structure. The 3D model is fabricated layer by layer on the print platform when the process is repeated, as shown in Figure 1.12. There is no need for support in 3DP technology because the powders can support themselves, and a variety of materials, including ceramics and plaster, can be printed (Gibson, Rosen & Stucker, 2015).

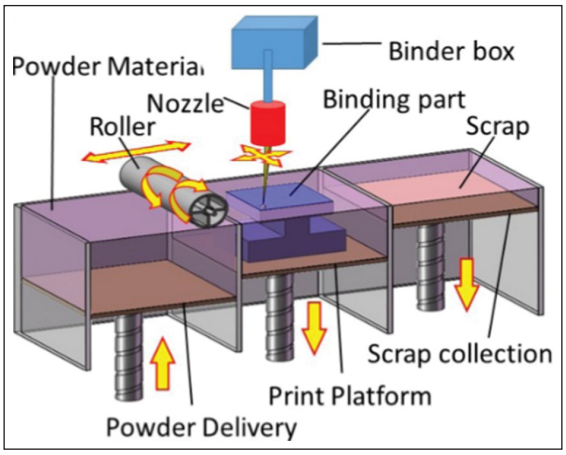

Figure 1.12 Binder Jetting Technology
Taken from Gibson *et al.* (2015)

1.4 Selected Technologies for This Project

In this research, two additive manufacturing (AM) processes are primarily utilized: Laser Powder Bed Fusion (LPBF) for metallic materials and Fused Deposition Modeling (FDM) for polymer materials such as Polylactic Acid (PLA) and Acrylonitrile Butadiene Styrene (ABS). These technologies were selected based on their suitability for RF component fabrication and their availability within the research environment. Specifically, an EOS 3D printer utilizing the LPBF process is available at the Shape Memory Alloys and Intelligent Systems Laboratory (LAMSI) at École de Technologie Supérieure (ÉTS), directed by **Professor Vladimir Brailovski**. Additionally, an FDM-based 3D printer is available at the Laboratoire de Communications et d'Intégration de la Microélectronique (LACIME), where this project is conducted. The key advantages of LPBF and FDM technologies are summarized in Table 1.2.

Table 1.2 Comparison of Additive Manufacturing Technologies

AM Technologies	Advantages
Laser Powder Bed Fusion (LPBF)	- **Reduced material waste:** Excess powder is collected and reused, minimizing material loss. - **Broad material compatibility:** LPBF supports a wide range of metal alloys, making it ideal for high-performance applications. - Enables the fabrication of complex geometries with high precision, surpassing conventional manufacturing constraints. - **Cost-effective for complex designs:** Since production cost is primarily influenced by material volume rather than part topology, LPBF is advantageous for intricate structures.
Fused Deposition Modeling (FDM)	- **Low-cost material:** FDM uses thermoplastics such as PLA and ABS, making it an economical option for prototyping. - **Rapid prototyping:** Provides a quick and efficient way to validate designs before metal fabrication. - **Ease of use and accessibility:** Widely available and requires minimal setup compared to other AM technologies. - **Scalability:** Suitable for fabricating both small-scale and larger parts with consistent layer adhesion.

1.5 Conclusion

This research aims to develop and validate an ML-based inverse design approach for 3D-printed RGW and PRGW components across operating frequencies from 3 to 300 GHz, tailored to specific performance and application needs. The proposed approach is demonstrated through the design of a highly isolated 90°-bent 4-port RGW structure, showcasing its adaptability to complex waveguide geometries. Furthermore, its applicability extends to the design of low-cost, origami-inspired, wideband, 3D-printed MIMO antennas with pattern-reconfigurable capabilities. By integrating ML for design optimization and leveraging AM for fabrication, this approach provides valuable guidance for microwave and antenna engineers, advancing next-generation MIMO antenna technology with a focus on compactness, high isolation, and pattern reconfigurability.

CHAPTER 2

MACHINE LEARNING-AIDED SYNTHESIS APPROACH FOR 3D PRINTED RIDGE GAP WAVEGUIDES

Mohammed Farouk Nakmouche, Dominic Deslandes, Ghyslain Gagnon

Département de Génie Électrique, École de Technologie Supérieure,
1100 Rue Notre-Dame Ouest, Montréal, Québec, H3C 1K3, Canada

Article submitted to the journal
IEEE Transactions on Components, Packaging and Manufacturing Technology
on July 11, 2025.

Abstract: In this paper, we propose a scalable machine learning (ML)-based inverse design approach for the automatic design of ridge gap waveguide (RGW) unit cells, targeting frequency bands and applications ranging from 3 to 300 GHz. This approach aims to improve reliability and reduce the high computational costs typically associated with the trial-and-error method or conventional optimization techniques in electromagnetic (EM) simulators, especially when the target frequency band changes. The proposed ML-based approach significantly reduces computation time, making predictions in less than 1 minute, compared to the 120, 72, and 96 hours required by the trial-and-error method, PSO, and GA optimizers, respectively. To validate this method, we designed a 2-port RGW structure operating within the 24–26 GHz range, tailored for the 5G n258 band (24–24.25 GHz) and midband applications (24.2–25.5 GHz). We conducted an experimental validation by fabricating the 2-port RGW structure with overall dimensions of 15 mm × 15 mm × 5.5 mm using laser powder bed fusion (LPBF) technology and measuring it with standard methods. The results demonstrate a measured reflection coefficient below -25 dB across the operating band and an average insertion loss of ≈ 3.5 dB, underscoring the effectiveness of the proposed ML-based design approach and the potential of 3D-printed technology for RGW-based component prototyping.

Keywords: Ridge Gap Waveguide, Additive Manufacturing, 3D printing, Machine Learning, and Automatic Modeling.

2.1 Introduction

The ridge gap waveguide (RGW), a well-established structure, was initially described by P. S. Kildal of Chalmers University in 2009 (Kildal, 1988a; Kildal, Alfonso, Valero-Nogueira & Rajo-Iglesias, 2009a). It has unique properties that can be utilized to design a wide range of millimeter-wave components (Beltayib & Sebak, 2019a; et al., 2023a; Peng, Pu, Wu & Luo, 2022a; Peng, Pu, Jiang, Chen, Wu & Luo, 2023a). The RGW is based on an electromagnetic band gap (EBG) structure, which is typically a bed of nails enclosed with a metal plate (Dyab,

Ibrahim, Sakr & Wu). The metal plate covering the bed of nails is isolated from the rest of the RGW structure, creating an air gap that confines and directs the electric field, hence the name 'gap-waveguides'(Peng, Pu, Wu, Chen & Luo, 2021a).

In comparison to microstrip line (MSL), substrate integrated waveguide (SIW), and conventional metallic waveguide technologies, the RGW is considered a structure with low loss due to the absence of dielectric material (Berenguer, Fusco, Zelenchuk, Sánchez-Escuderos, Baquero-Escudero & Boria-Esbert, 2016b). Furthermore, the non-contact vertical metallic walls make the RGW easier to fabricate at higher frequencies (Shi, Feng & Cao, 2021b).

A RGW consists of numerous unit cells, as depicted in Fig. 2.1. The stop band of the unit cell determines the working bandwidth of the RGW. Thus, it is crucial to design properly the RGW unit cell to achieve the target application bandwidth.

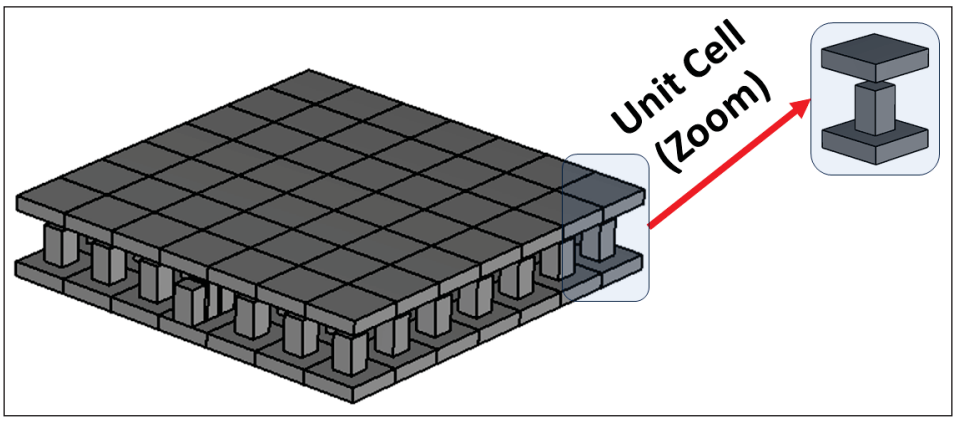

Figure 2.1 Ridge Gap Waveguide (RGW) basic structure

Fan et al. (Fan, Yang, Vassilev & Zaman, 2018) created an RGW unit cell based on a half-height pin to reduce the cost of manufacturing and investigated the stopband properties of this structure. Compared to full-height pins, the authors observed that a wider half-pin does not significantly decrease the stop band. However, in a typical bed of nails, it does reduce the stop band. The proposed pin allows for a thicker and shorter structure, thereby reducing the computational cost compared to a standard bed of nails. Shams et al. (Shams & Kishk, 2017a) proposed another RGW unit cell based on tapered patches printed on a circuit board. They showed how the tapered pins improved bandwidth more than the traditional rectangular pins. Recently, new low-cost RGW structures built on glide-symmetric cells (Ebrahimpouri, Quevedo-Teruel & Rajo-Iglesias, 2017; Ebrahimpouri, Rajo-Iglesias, Sipus & Quevedo-Teruel, 2018) have been used instead of the usual bed of metal pins to make a wider stop band.

While numerous studies have investigated and presented in-depth analyses of innovative RGW unit cells, it is evident from the reported works that the band-stop frequency of these cells is not entirely deterministic. In the

most reported design process of an RGW unit cell, the engineer initially specifies the target stop-band frequency appropriate for their application. Subsequently, the dispersion diagrams that show the first three propagating modes are calculated and plotted. The obtained results give approximated and not accurate start and end frequencies of the stop band. Engineers then need to update these physical dimensions through many iterations (parametric studies) until the objectives are met. This approach is inefficient in terms of computational cost (et al., 2023e,2,2,2). This inefficiency arises from the complexity of the problem, which involves numerous variables, multiple objectives, and constraints that to some extent require several electromagnetic (EM) iteration steps.

To overcome this, some studies have proposed analytical solutions for calculating the dominant quasi-TEM mode in homogeneous RGW (Polemi & Maci, 2010a; Silveirinha, Fernandes & Costa, 2008a). A dispersion equation, which yields accurate results for the stop band in comparison to the CST Studio Suite eigenmode solver findings, has been used and generated. However, while the proposed closed formula for determining the band stop remains valid for particular unit cell parameters, the generalization is not achievable.

A technique to fully automate the design process of an RGW unit cell, serving as the main block for various RGW-based component designs, would be beneficial. However, approaches for automating the RGW design process have not been investigated in the literature.

The main objective of this paper is to introduce an accurate, systematic, and straightforward machine learning (ML)-based inverse synthesis approach for RGW unit cell design. This approach enables the automatic design of the RGW unit cell for any given frequency band, ranging from 3 to 300 GHz, in an accelerated way.

A detailed analysis is done in terms of mean squared error (MSE), the mean absolute error (MAE), and computational time to demonstrate the effectiveness of the proposed approach. Then, it is compared to the conventional trial-and-test approach and the conventional optimization-based approaches available in popular EM simulators, like the genetic algorithms (GA) and particle swarm optimization (PSO). It should be noted that since the proposed approach is based on ML, a slightly higher computational cost is required for data generation initially. However, after training, the model becomes scalable and can be applied to any given frequency band between 3 and 300 GHz. In contrast, conventional approaches require high computational costs each time the target frequency band is changed.

Furthermore, to validate our proposed approach, we apply it to the design of a 2-port RGW structure operating from 24 to 26 GHz. Subsequently, it is fabricated using the laser powder bed fusion (LPBF) process reported in (Singh, Gupta, Tripathi, Srivastava, Singh, Awasthi, Rajput, Sonia, Singhal & Saxena, 2020). The LPBF process overcomes the poor thermal properties associated with the reported work based on polymer-based additive manufacturing and copper plating techniques (Palomares-Caballero, Alex-Amor, Valenzuela-Valdés & Padilla, 2021; Tak, Kantemur, Sharma & Xin, 2018).

The two key contributions of the present research are as follows:

1: Introduction of a new ML-based inverse synthesis approach of RGW unit cells for any given frequency band, ranging from 3 to 300 GHz, in an accelerated and straightforward way.

2: The potential use of LPBF technology in fabricating RGW-based components. This will be attractive to design three-dimensional, highly integrated RGW components for applications with limited space constraints, as observed in Cube Satellites (CubeSat).

The remainder of this article is organized as follows: Section II provides an overview of RGW technology and outlines the main parameters used in the ML model. Section III presents a detailed description of the proposed ML-based inverse synthesis approach, along with its performance validation and comparison to conventional approaches. In Section IV, a test case and experimental validation using LPBF of a 2-port RGW structure operating in K-band are presented. In Section VI, we present a summary of various RGW dimensions for standard applications that can be used as guidelines by engineers. Finally, Section VI concludes the paper.

2.2 Ridge Gap Waveguide Technology and Design Considerations

2.2.1 RGW Working Principle

The working principle of the RGW is to guide the propagation of EM waves via a parallel-plate waveguide (Bayat-Makou & Kishk, 2018a). Traditionally, a parallel-plate waveguide comprises two unconnected perfect electric conductor (PEC) plates, between which the EM wave propagates.

However, when one of the PEC plates is replaced with perfect magnetic conductors (PMCs) at a separation distance of $\lambda/4$, the transmission of EM between them becomes impossible. This is due to the high surface impedance characteristics of the PMC, which cause a cutoff for all propagating modes across an air gap smaller than $\lambda/4$ (et al., 2023d). Changing a segment in this PMC area to a PEC, which can be a ridge, groove, or strip, forces EM waves to follow the designated PEC pathway. The concept described above is illustrated in Fig. 2.2.

While current metallic materials can approximate ideal PEC behavior to a certain extent, real PMCs do not naturally exist. However, they can be artificially engineered, often taking the form of an artificial magnetic conductor (AMC) or a high-impedance surface (Kildal, 1988b).

Clearly, AMC significantly influences the design of RGW. This is because the frequency range within which the local quasi-TEM mode can propagate as the single mode is defined by the presence of a stop band in the parallel-plate modes within that frequency range.

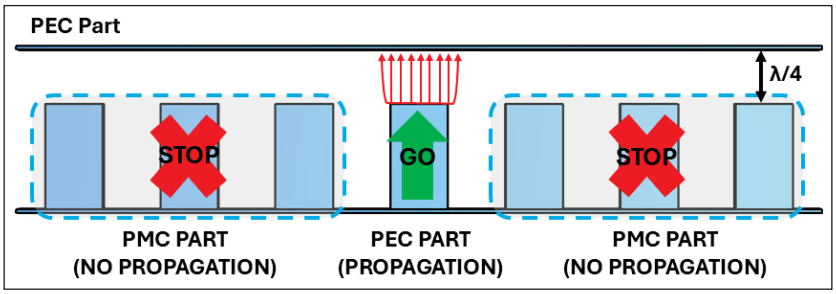

Figure 2.2 RGW working principle

2.2.2 RGW Design Parameters

From the reported works by Iglesias et al. (Rajo-Iglesias & Kildal, 2009,1), we deduce that the critical design parameters for the RGW unit cell, as shown in Fig. 2.3, which influence the stop band, are as follows:

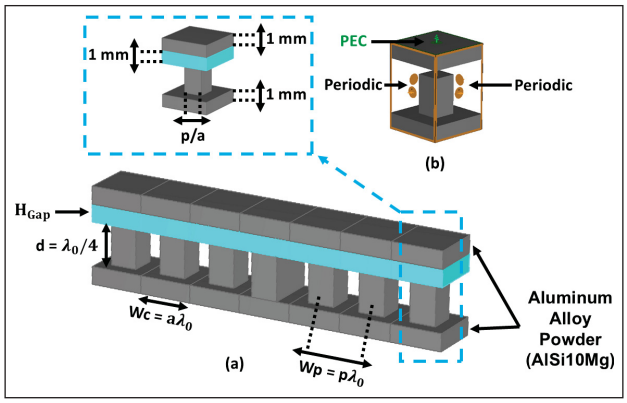

Figure 2.3 Proposed 3D Printed RGW (a) Unit cell (b) Boundary conditions

- The pin height d, governed by the central frequency as $d = \lambda_o/4$, where λ_o represents the center wavelength of the band-stop frequency.
- The coefficient w related to H_{Gap} as $H_{\text{Gap}} = w \times \lambda_o$.
- The coefficient p related to W_p as $W_p = p \times \lambda_o$.
- The coefficient a related to W_c as $W_c = a \times \lambda_o$.

In the study of Iglesias et al. on the start and end of the RGW stop band, the period (p) was adjusted from $0.0625\lambda_o$ to $0.25\lambda_o$ while maintaining a constant pin height (d) at $0.25\lambda_o$. They found that altering the period did not significantly affect the end frequency of the stop band. However, they observed a downward shift in the start frequency as the period increased.

In contrast, decreasing the coefficient w while keeping the period fixed to $\lambda/8$ results in a proportional increase in the end frequency of the stop band. Lastly, it is noteworthy that smaller values of H_{Gap}tend to yield larger stop bands.

2.3 Proposed ML-based inverse synthesis approach

2.3.1 Data Generation Process

ML-based synthesis approaches have found extensive application in the fields of radio frequency (RF), microwave, and millimeter-wave (mmWave) component synthesis (Roy & Wu, 2022, TBD; Roy, Lin & Wu, 2023; Sharma, Zhang & Xin, 2020a; Sharma, Chen, Wu, Zhou, Zhang & Xin, 2022; Wu, Wang & Hong, 2020; Zhao & Wu, 2020). These approaches rely on EM simulations as the initial step to generate datasets, which are subsequently utilized in the ML training process (et al., 2023g).

In this work, a total of 3240 samples were generated, with 2268 (70%) sets of samples for training purposes and 486 (15%) sets of samples for validation. Additionally, a distinct set of 486 (15%) samples, unseen during the training phase, was employed to assess the performance of the trained ML model. The overall approach for automatic data generation shown in Fig. 2.4 outlines the steps described in Algorithm 1.

2.3.2 Implementation Workflow

Using the generated dataset, we apply machine learning (ML) to predict the physical dimensions of the RGW unit cell based on the band stop provided by the engineer, with input frequencies ranging from 3 to 300 GHz. The overall framework of the proposed ML-based inverse synthesis approach, as illustrated in Fig. 2.5, includes the main steps outlined in Algorithm 2.

From a ML perspective, our objective is to predict three continuous values (coefficient a, coefficient p, and coefficient w) from two input variables (F_{Top} and F_{Low}).

To achieve this, we have chosen K-nearest neighbors (k-NN) algorithm (Marsland, 2014a; Srivastava, 2014). The k-NN algorithm is a supervised neighbor-based learning regression algorithm that operates by determining a predefined number of training samples that are closest to the new point (Yang, Chen, Zhao, Pan, Guo & Yang, 2023).

To predict new data points, the algorithm employs "feature similarity," which means that the new point is assigned a value based on how closely it resembles the training set (Cui, Zhang, Zhang & Liu, 2020). The similarity measure is commonly expressed by calculating the distance between data points using various methods, such as the Euclidean,

Algorithm 1 Proposed Data Generation Approach

1: Start Visual Basic (VBA) macro programming platform.

2: Set the boundary condition as shown in Fig. 2.3 (b):

- Periodic boundary conditions along the longitudinal and lateral directions.
- PEC on top and bottom surfaces.
- Set the characteristics of the used material: conductivity, surface roughness, thermal conductivity, and density.

3: Set the main RGW unit cell physical dimensions as follows:

- Set the coefficient a vary from 0.1 to 0.3.
- Set the coefficient p vary from 0.025 to 0.075.
- Set the coefficient w vary from 0.002 to 0.25.
- Set λ_0 = [29.27, 19.98, 13.32, 9.01, 1.81] in mm.

The values for a, p, and w are selected according to findings reported in (et al., 2020; Rajo-Iglesias, Caiazzo, Inclán-Sánchez & Kildal, 2007a), indicating optimal performance when both p and w approach zero. In contrast, λ_0 is randomly chosen for each standard frequency band within the range of 3 to 300 GHz.

4: Execute the VBA macro programming code to automatically run the eigenmode solver.

5: Calculate the three first propagating modes.

6: Extract and plot the dispersion diagram.

7: Identify the lower frequency F_{Low} and upper frequency F_{Top}.

8: Repeat steps 5-7 until all combinations for the different RGW unit cell physical dimensions are executed.

9: Organize the dataset as inputs and outputs.

Algorithm 2 Proposed ML-based inverse synthesis approach

Input: Band stop frequency (F_{Low} and F_{Top})
Output: RGW unit cell physical dimension (a, p, and w)

1: Define target stop frequency band (F_{Top} and F_{Low}).

2: Execute the trained ML model to automatically predict the RGW physical parameters (a, p, and w).

3: Start VBA macro programming platform.

4: Execute the VBA macro programming code to automatically run the eigenmode solver.

5: Calculate the first three propagating modes.

6: Extract and plot the dispersion diagram showing the band-stop frequency.

7: Validate the results with the predefined target objective given by the engineer as input.

8: Execute the VBA macro-programming code for an automatic design of a chosen RGW-based component.

9: Run the transient solver analysis.

10: Extract the performance results (s-parameters, realized gain, etc.) of RGW-based components.

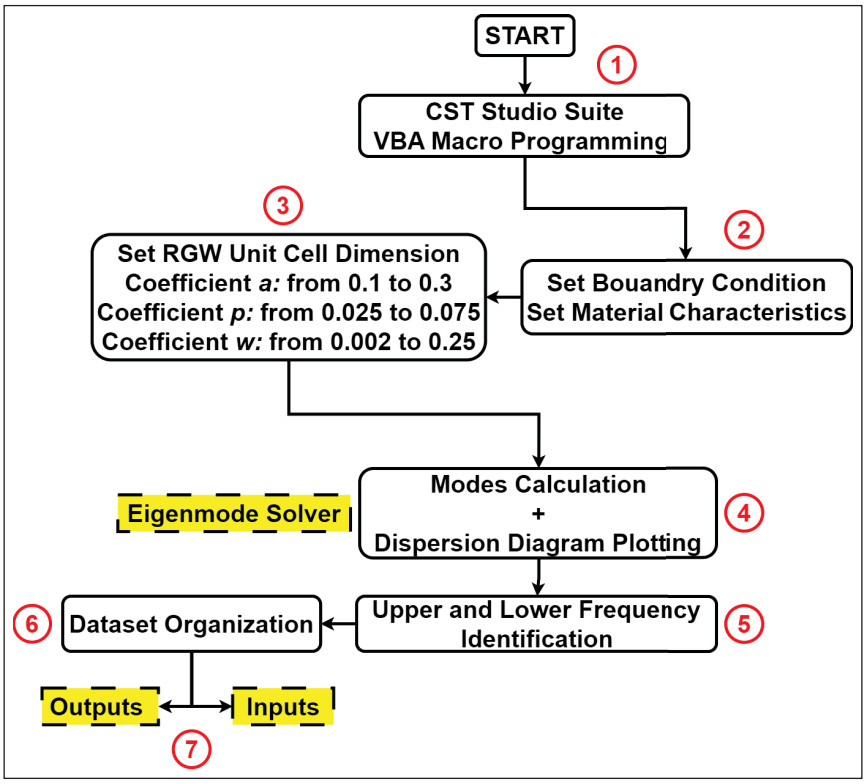

Figure 2.4 Proposed automatic dataset generation approach

Manhattan, or Hamming methods (Vanderplas, Pedregosa & Gramfort, 2011,1). In this work, we chose to employ the Euclidean distance methods defined as follows:

$$\text{Euclidean distance} = \sqrt{\sum_{i=1}^{k}(p_i - q_i)^2} \tag{2.1}$$

where $p = (p_1, p_2, \ldots, p_k)$ and $q = (q_1, q_2, \ldots, q_k)$ are two different neighboring points.

The k-NN can be mathematically represented by equation (2), in which X_i represents the inputs, Y_i the outputs, and k is the number of nearest neighbors used to conduct the prediction (Haykin, 2008). If we consider k as the number of nearest neighbors in the k-NN algorithm and X_0 as a prediction point, then N_0 represents the k training instances that are closest to X_0. The k-NN algorithm estimates $f(X_0)$ by averaging the responses of all instances in N_0.

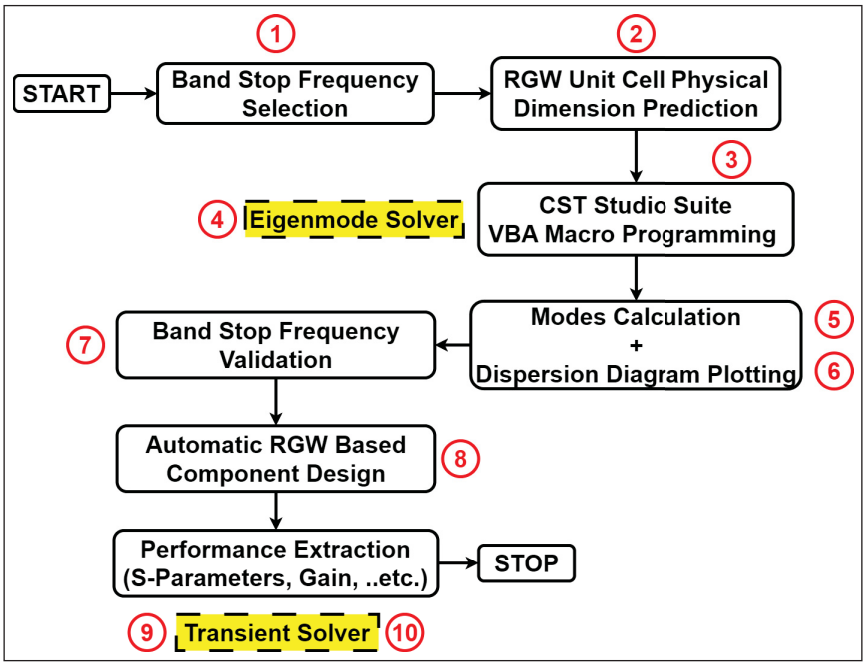

Figure 2.5 Flowchart of the ML-based synthesis approach

$$f(X_i) = \frac{1}{k} \sum_{X_i \in N_0} Y_i \tag{2.2}$$

Fig. 2.6 illustrates our proposed ML model, where the input layer represents the upper F_{Top} and lower F_{Low} frequencies of the RGW stop band. The output layer consists of three primary outputs: the coefficient a, the coefficient p, and the coefficient w, which are related to the RGW's unit cell dimensions.

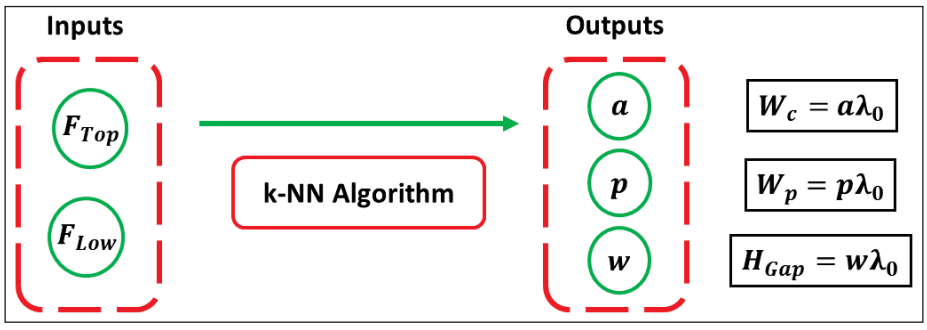

Figure 2.6 Proposed K-Nearest Neighbors (kNN) model

2.4 Model Performance Evaluation

To evaluate the efficiency of the trained k-NN model, we assess its ability to accurately and rapidly predict the RGW unit cell physical dimensions for any specified frequency band ranging from 3 to 300 GHz depending on the applications. The performance of our trained k-NN model using two metrics: mean square error (MSE) and mean absolute percentage error (MAPE), as defined in equations (3) and (4) (Murphy, 2012; Shalev-Shwartz & Ben-David, 2014a).

$$\text{MAPE} = \frac{1}{n}\sum_{i=1}^{n}\left|\frac{y_{\text{true}(i)} - y_{\text{pred}(i)}}{y_{\text{true}(i)}}\right| \times 100 \tag{2.3}$$

$$\text{MAE} = \frac{1}{n}\sum_{i=1}^{n}\left|y_{\text{true}(i)} - y_{\text{pred}(i)}\right| \tag{2.4}$$

$$\text{MSE} = \frac{1}{n}\sum_{i=1}^{n}(y_{\text{true}(i)} - y_{\text{pred}(i)})^2 \tag{2.5}$$

where y_{true} represents the actual value, y_{pred} denotes the predicted value generated by the ML model, and M indicates the size of the dataset used for assessment and comparison. Both MSE and MAPE are used to quantify the error between the output values generated by the k-NN model and the actual values in the dataset.

As with most ML projects, we train multiple k-NN models with different hyperparameters on our dataset to determine the one that performs best. The performance of these models is strongly influenced by their hyperparameters, and since the optimal values cannot be determined in advance, it is necessary to explore all possible combinations to find the best values.

Manually executing this task demands considerable time and resources; hence, we utilize the GridSearchCV technique to automate the tuning of hyperparameters. This technique enables the evaluation of the model's performance by considering a combination of its hyperparameters and determining the optimal values that lead to low MAE and high MAPE values. Through GridSearchCV, we can establish for our dataset a k-NN model utilizing Euclidean distance with k=3 can effectively establish a mapping between the input F_{Top}/F_{Low} and the three output coefficients (a, p, w) that govern the dimensions of the RGW unit cell.

Table 2.1 Comparison of k-NN with other conventional techniques

Algorithms	**GA**	**PSO**	**Trial and-Error**	**Machine Learning Models**				
				k-NN	LR	**SVR**	**ANN**	RF
Average MSE	NA	NA	NA	**0.01**	5.79	0.50	0.47	0.20
Average MAPE (%)	NA	NA	NA	**7.34**	137.61	179.85	44.60	43.92
Data Generation Time	NA	NA	NA	**144 hours (total for all models)**				
Computational Time	96 hours	72 hours	120 hours	**1 minute (total for all models)**				

We investigated other machine learning algorithms, including linear regression (LR), support vector regression (SVR), artificial neural networks (ANN), and random forest (RF), in addition to the selected k-NN model. However, due to the size of the generated dataset, these models introduced higher complexity and required extensive fine-tuning. Despite our efforts, they did not outperform the trained k-NN model in terms of MSE and MAPE, as shown in Table 2.1.

2.4.1 Computational Time Analysis

In terms of computational time, we conduct a comparison with the GA and PSO optimizers, as well as a direct trial-and-test-based approach. This comparison is based on the target stop-band characteristics of the unit cell, which suppresses EM wave propagation in the 20 GHz to 32 GHz range.

As can be seen from Table 2.1, the proposed approach makes predictions in less than 1 minute, whereas the trial-and-test approach, PSO, and GA optimizers require 120, 72, and 96 hours, respectively. Thus, we can conclude that the proposed trained k-NN models offer notable enhancements in computing efficiency compared to the conventional design approach, which is time-consuming and has expensive computational costs. Notably, the training dataset was generated through 144 hours of full-wave simulation, a process commonly implemented in ML applications for EM problems. This computational cost is incurred only once; thereafter, the trained model becomes scalable and can be applied to any target frequency band between 3 and 300 GHz, tailored to diverse application requirements. However, this becomes a constant requirement in conventional approaches whenever the target frequency band changes.

We further extended our computational time analysis to examine the effect of the number of neighbors (k) and the distance metric on computational time and memory usage. Fig. 2.7(a) presents the results for the Euclidean distance metric, while Fig. 2.7(b) shows the results for the Manhattan distance metric.

In Fig. 2.7(a), computational time (blue line) remains relatively stable with slight fluctuations and noticeable dips at k = 40 and k = 100. Memory usage (red line) slightly increases as k grows but stays nearly constant overall.

This result highlights the computational stability and minimal memory overhead associated with the Euclidean distance metric. In Fig. 2.7(b), we observe that the computational time remains relatively stable, though it exhibits more noticeable fluctuations compared to Fig. 2.7(a). Specifically, the computational time dips at k = 40 and k = 100. Meanwhile, the memory usage for the Manhattan distance metric increases slightly with k but remains nearly constant overall.

The analysis shows that the Euclidean distance metric offers better computational stability and slightly lower memory usage, validating the results of GridSearchCV (learn Contributors), thereby confirming it as the preferred option.

All the computations are carried out on a Windows 64-bit Lenovo ThinkStation P320 tower workstation with a 12th Generation Intel® Core™ i7-12700K Processor with vPro® (E-Core Max 3.80 GHz, P-Core Max 4.90 GHz with Turbo Boost, 12 Cores, 20 Threads, 25 MB Cache), 32 GB of RAM, and NVIDIA® T1000 4GB.

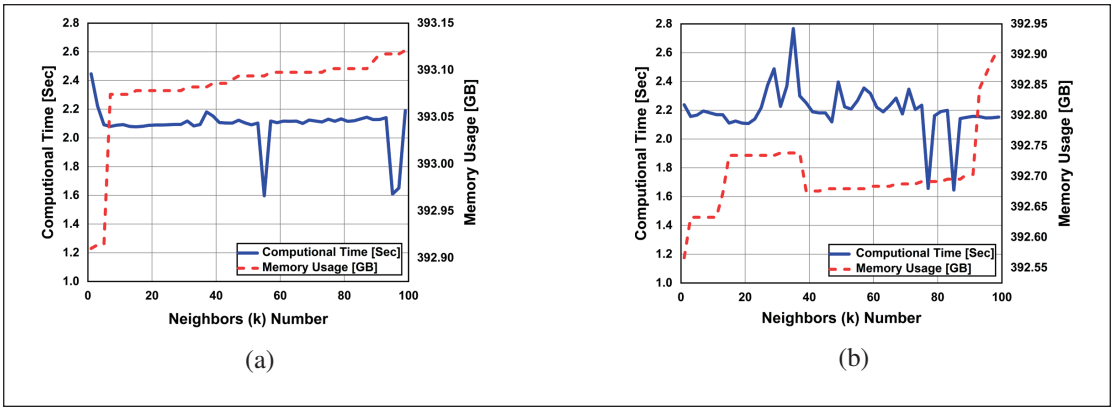

Figure 2.7 Computational time and memory for various k values with (a) Euclidean and (b) Manhattan distance metrics

2.4.2 Ablation Study

We conducted an ablation study to investigate the effect of the number of neighbors and the methods used to calculate their distances on model performance. Specifically, we analyzed the MSE and MAE during both the training and validation phases, using various values of k with Euclidean and Manhattan distance metrics. Fig. 2.8 and Table 2.2 presents a comparison of the MSE and MAE values for the k-NN algorithm across these conditions.

It is evident that as k increases, both the MSE and MAE values worsen, indicating a decline in model performance. This suggests that, for our generated dataset, increasing k results in incorporating more neighbors into the prediction process. However, this can lead to overfitting, ultimately reducing the model's accuracy. Fig. 2.8 further confirms

the results obtained from GridSearch, supporting the choice of selecting the k-NN algorithm with a k value of 3 and the Euclidean distance metric.

Table 2.2 k-NN performance evaluation for different parameters

Evaluation Metrics	**Number of Nearest Neighbors**					
	3	**4**	**16**	**64**	**128**	**256**
Average MSE	**0.01**	0.025	0.15	0.11	1.33	3.68
Average MAE	**0.02**	0.025	0.15	0.11	0.56	1.68

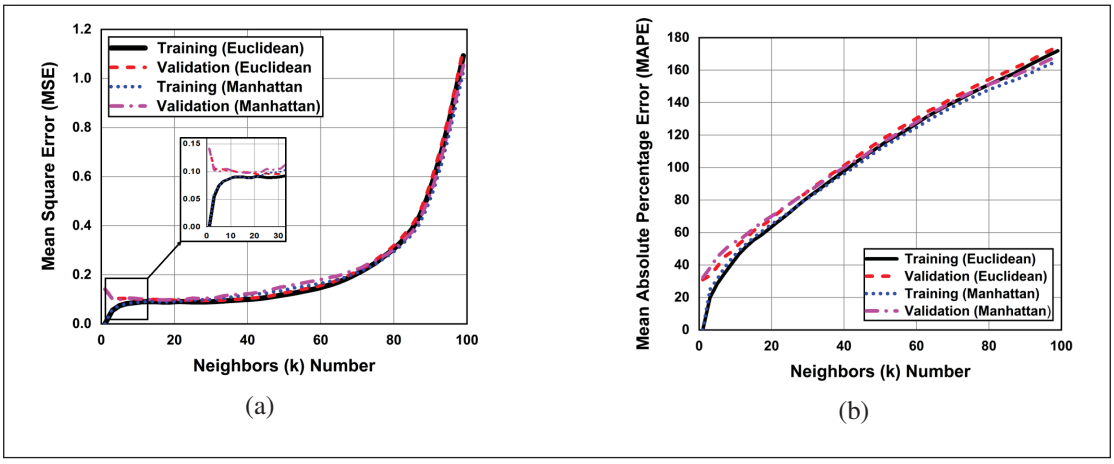

(a) (b)

Figure 2.8 Training and validation MAPE and MSE for KNN regression across varying k values: (a) Euclidean distance and (b) Manhattan distance

2.5 Test Case & Experimental Validation

In this section, we employ our proposed ML-based approach to design a 2-port RGW-based structure for 5G n258 band (24–24.25 GHz) and midband applications (24.2–25.5 GHz) as a test case.

Using the trained k-NN model, we predict the optimal parameters (see Table 2.3 of the 3D-printed RGW unit cell and validate them by analyzing the dispersion diagram using the eigenmode solver available in the EM simulator.

Table 2.3 Predicted optimal dimensions of the unit cell and ridge

Parameter	**Description**	**Values**
Coefficient w	Control the gap ($H_{\text{gap}} = w\lambda_0$)	0.002
Coefficient a	Control the pin size ($W_c = a\lambda_0$)	0.2
Coefficient p	Control the periodicity ($W_p = p\lambda_0$)	0.25
Pin Height (d)	$\lambda_0/4$ with $\lambda_0 = 13.32411$ mm	3.33

As shown in Fig. 2.9, the obtained band stop is between 20 GHz and 32 GHz, which is suitable for our target application frequency band, where the quasi-TEM field is propagated over the ridge, resulting in a dominant mode with minimum dispersion.

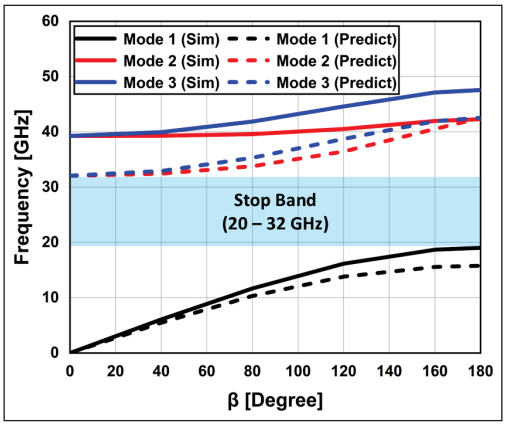

Figure 2.9 Dispersion diagram of the predicted 3D-printed RGW

Using the predicted unit cell, we designed and then 3D print a 2-port RGW-based structure using LPBF technology and aluminum alloy powder (AlSi10Mg) (GmbH, n.d.). The surface roughness was between 3 and 8μm, depending on how the printed parts were treated after they were made. We chose AlSi10Mg due to its characteristics of being low-weight, having good conductivity, and possessing good power-handling capabilities.

To the best of the author's knowledge, the use of 3D printing LPBF technology to fabricate RGW-based structures is being proposed for the first time.

To facilitate feeding the proposed 3D-printed RGW structure, an MSL-to-RGW transition is designed, inspired by the work in (Peng, Pu, Wu, Chen & Luo, 2021b). The designed transition allows easy integration of the RGW-based structure with other monolithic microwave integrated circuits (MMICs).

In our design, as shown in Fig. 2.10, the proposed transition from MSL to RGW has two main parts, namely, the MSL-to-suspended MSL conversion and the suspended MSL-to-RGW conversion. The suspended MSL connects the MSL and RGW, with the MSL positioned directly on the base block and the suspended MSL extending to the end of the ridge.

The 2-D electric field (E-field) distribution of the proposed transition is depicted in Fig. 2.11. The upper field of the suspended MSL looks like the RGW field, while the lower field looks like the standard MSL field. Consequently, the rectangular patch is suitable for a matched and efficient transition from MSL-to-RGW. The simulated E-field distribution of the fully metallic 3D-printed RGW with transition is shown in Fig. 2.12.

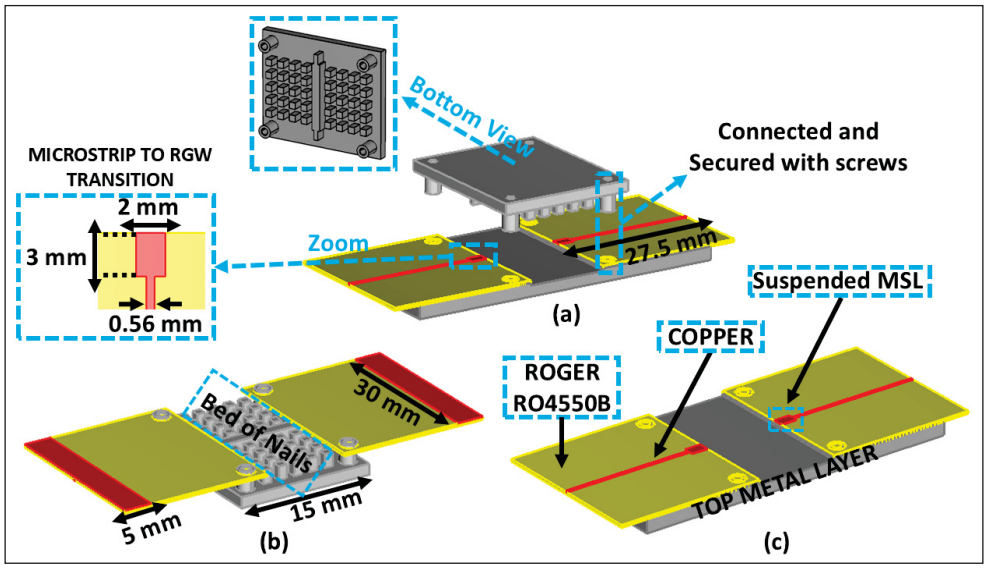

Figure 2.10 3D model of the designed fully metallic 3D printed-based RGW (a) Exploded view (b) The bed of nails layer (c) PEC layer

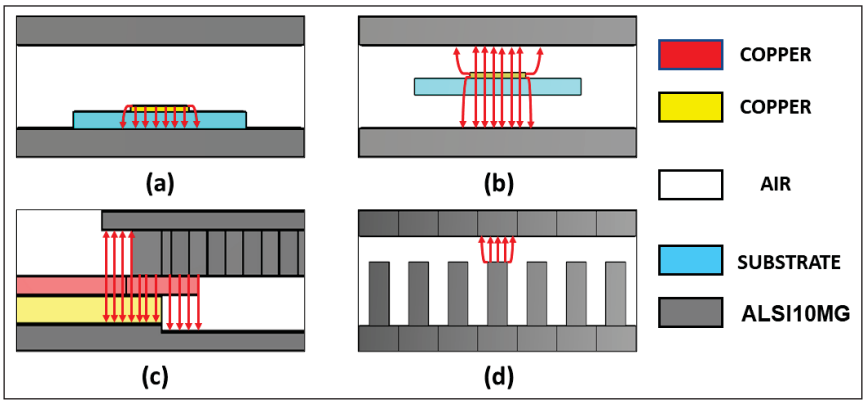

Figure 2.11 2-D E-field distributions of the dominant mode of (a) Conventional MSL (b) Conventional Suspended-MSL (c) Used transition (d) Conventional RGW

2.5.1 Fabricated Prototype

The fabricated waveguide and its different main parts are presented in Fig. 2.13. The connection between the two assembly parts is established using only four screws.

As mentioned before, the prototype was fabricated using LPBF technology, which uses high-powered lasers to melt the metal powder into parts using only the powder material required to build the parts, with the rest being reusable for another fabrication.

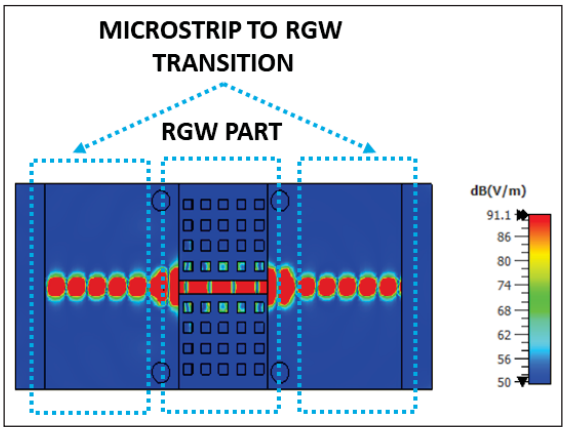

Figure 2.12 E-field distribution of the 3D printed RGW with transition

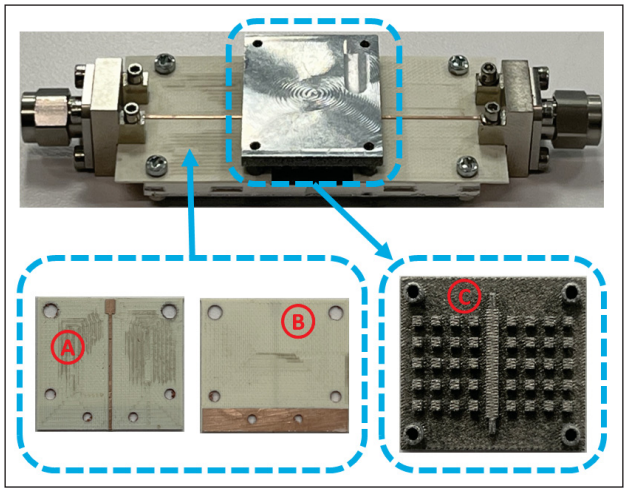

Figure 2.13 Assembled fully metallic 3D printed RGW (a) Top view of the MSL to RGW transition (b) Bottom view of the MSL to RGW transition (c) 3D-printed bed of nails layer

The LPBF technology involves three main steps, as follows (et al., 2017a; Peverini, Lumia, Addamo, Virone & Fonseca, 2023a): First, the EM simulator prepares and generates the SLA files. These SLA files are processed by special build preparation software that breaks them down into slices or layers for 3D printing, generates the printing path, and provides other instructions for the 3D printer to follow.

Next, metal sintering starts, involving a bed of metal powder and high-powered lasers with power up to 1 kW used to selectively fuse metal powder layer-by-layer. This is achieved by gradually lowering the building platform and repeating the process until the final part is complete. Simultaneously, the unused powder is transferred to the collector platform. After the printing is done, the parts are cleaned of the unprocessed powder, along with the entire platform. Then the parts, still connected to the building base, undergo stress-relieving post-processing in an oven.

Lastly, the structures used as supports are removed, and the parts are detached from the building base. The final step involves polishing the LPBF 3D-printed RGW, which has been removed from the building base, to enhance its appearance and quality. However, certain structures might be incapable of enduring the pressure of polishing, especially those that are thin, fragile, or complex, such as the bed of nails. Thus, we proceed with polishing the external surface of the proposed 3D-printed RGW without the bed of nails, as shown in Fig. 2.13.

2.5.2 Measurement Results

The 3D-printed RGW was measured using a two-port Agilent PNA-X 67 GHz Network Analyzer available in the Microelectronics and Communications Research Lab (LACIME) at ETS Montreal. The measured insertion loss (IL) of the waveguide varies between 2 dB and 4.5 dB in simulation with surface roughness (Ra), as illustrated in Fig. 2.14 (a). In comparison to the simulation IL without surface roughness (Ra), the measured IL shows a marginal decline of 1 dB. Despite the presence of an air gap between the RGW main parts, the IL remains acceptable, affirming that the wave propagates along the waveguide without significant loss.

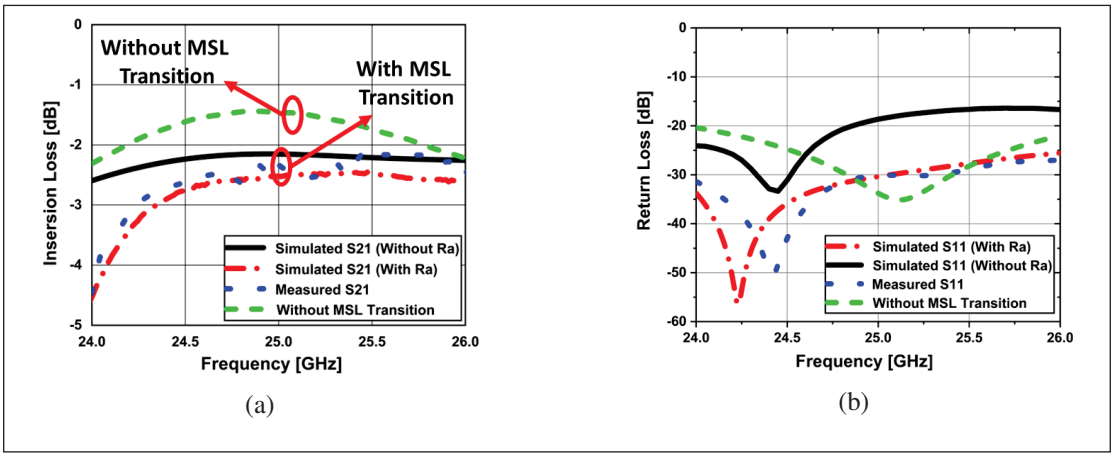

Figure 2.14 Simulated and measured S-parameters [dB]: (a) Insertion loss and (b) Return loss

The simulated and measured return loss (RL) for the 3D-printed RGW structure is depicted in Fig. 2.14 (b). It is clear that over the 24-26 GHz frequency band, the measured results of RL indicate values lower than -25 dB, whereas the simulation results with and without surface roughness (Ra) show values lower than -25 dB and -15 dB, respectively. In summary, the RL is below -25 dB over the operating frequency band (24–26 GHz), and the IL is about 3.5 dB on average. Notably, small discrepancies exist between the measured and simulated RL and IL results. These slight variations between simulation and measurement can be attributed to the following factors:

1: Surface polishing and surface roughness.

2: The misalignment that can occur between the MSL feeding structure and the ridge during the assembly.

3: Lastly, a 1.5 dB loss difference is related to the fact that no standard thru-reflect-line (TRL) de-embedding method was used in the measurement process.

The obtained results show significant promise for designing three-dimensional components based on RGW using 3D-printing technology. These components are particularly relevant for applications that demand highly integrated and isolated communication systems, such as those found in CubeSats, where space constraints are critical.

2.6 Design Guideline

Due to the limitations of our measurement equipment, we were unable to experimentally validate prototype designs for higher frequency bands, such as 74–82 GHz and 200–250 GHz. However, to demonstrate the scalability of our proposed ML-based approach across a broader frequency range, we present in Table III the predicted physical dimensions of an RGW unit cell for various standard frequency bands and applications. These dimensions serve as target inputs, which are subsequently compared and validated through simulations. Specifically, we focused on frequency bands within the Ku-band, K-band, Ka-band, and mmWave spectrum, selected for their critical relevance to radar systems, automotive radar, satellite communications, inter-satellite links, and mobile 5G and 6G applications.

As shown in Table 2.4, simulating with the predicted dimensions causes a slight shift in the frequency band compared to the target input bands. However, the simulated band, based on these predicted dimensions, remains within the target stop band despite minor discrepancies. From an application perspective, we find this discrepancy acceptable, as most studies focus on a specific, limited bandwidth within the stop band of the PRGW unit cell rather than covering the entire stopband frequency range. Combined with the proposed ML-based inverse synthesis method, this summary offers a practical tool for designers to tailor solutions to their specific band application requirements.

Table 2.4 RGW unit cell physical dimensions for various standard frequency bands

Target Inputs	**Predicted Outputs**				**Simulation Validation**	**Band & Application**
F_{Low} - F_{Top}	**Coefficient** w	**Coefficient** a	**Coefficient** p	λ_0	F_{Low} - F_{Top}	
12–15 GHz 15–22 GHz	0.05 / 0.2367	0.1 / 0.3	0.0583 / 0.075	29.97925 / 13.32411	9.04–14.55 GHz / 17.55–22.91 GHz	Telesat Downlink (17.8–20.1 GHz) OneWeb Uplink (12.75–14.5 GHz) Telesat Downlink (17.8–20.1 GHz)
22–28 GHz	0.11	0.1	0.05	13.32411	20.41–28.45 GHz	Radar (24–24.25 GHz) 5G n258 (24.25–27.5 GHz) 5G Mid Band (25.25–27.5 GHz)
26–32 GHz	0.2467	0.3	0.0667	9.01631	26.14–33.29 GHz	5G n257 (26.5–29.5 GHz) Telesat Uplink (27.5–30.0 GHz) Kuiper Uplink (28.35–30 GHz)
55–65 GHz 148.97–285.96 GHz	0.0333 / 0.03	0.1 / 0.1	0.025 / 0.075	9.01631 / 1.81692	30–57.63 GHz / 149.82–239 GHz	Intersatellite (59–64 GHz) Sub-terahertz comm. in 6G (90–300 GHz)

2.7 Conclusion

This paper pioneers a scalable ML-based inverse synthesis approach for automatic RGW unit cell design for any target frequency band from 3 to 300 GHz. These unit cells serve as the main building blocks for various component designs, including filters, couplers, and antennas. The proposed approach demonstrates superiority to conventional approaches such as trial and test, PSO, and GA in terms of reliability and computational efficiency. Our proposed approach can automatically and accurately predict the RGW unit cell's physical dimension. This is achieved by predicting the main controlling parameters of RGW (a, p, and w) in terms of the stop band frequency (F_{Top} and F_{Low}) given by the engineer. Validation through 2-port RGW-based structure fabrication using LPBF technology and measurement demonstrates good alignment between prediction/simulation and measurement results. With a reflection coefficient less than -25 dB and an insertion loss of about $\approx$ 3.5 dB on average across the specified frequency band. Our work enhances the RGW unit cell design process by reducing the computational cost required to design an RGW unit cell and RGW-based components. Additionally, it also highlights the potential use of ML and 3D printing technology for efficient, reliable, highly integrated, and isolated subsystem design.

CHAPTER 3

3D-PRINTED METALLIC 90° BENT RIDGE GAP WAVEGUIDE STRUCTURES: ENABLING COMPACT ANTENNA AND PASSIVE COMPONENT INTEGRATION IN CUBESATS

Mohammed Farouk Nakmouche[1], Dominic Deslandes[1], Ghyslain Gagnon[1], Vladimir Brailovski[2]

[1]Département de Génie Électrique, École de Technologie Supérieure,
1100 Rue Notre-Dame Ouest, Montréal, Québec, H3C 1K3, Canada

[2]Département de Génie Mécanique, École de Technologie Supérieure,
1100 Rue Notre-Dame Ouest, Montréal, Québec, H3C 1K3, Canada

Article submitted to the journal
« IEEE Antennas and Wireless Propagation Letters »
on July 4, 2025.

Abstract: This letter presents, for the first time, the feasibility and potential of fully metallic 3D-printed technology for the implementation of 90° bent ridge gap waveguide (RGW) structures that are unachievable through conventional milling due to their three-dimensional complexity. Experimental validation is provided through the realization of two components: a narrowband, highly isolated 90° bent 4-port RGW-based waveguide bend and a compact slot antenna with an integrated 90° bend, both tailored for compact CubeSat integration. Designed for millimeter-wave (mmWave) Internet of Space (IoS) applications operating between 26 and 28 GHz, the waveguide bend achieves a reflection coefficient between –10 and –20 dB, insertion loss between 1 and 2 dB, and port-to-port isolation exceeding 40 dB. The antenna operates from 27.3 to 28 GHz, achieving a maximum realized gain of 5 dBi and a radiation efficiency of 78%. Beyond demonstrating the feasibility of metal additive manufacturing for complex RGW geometries, the proposed structures offer substantial benefits in footprint reduction, integration flexibility, and structural robustness. These advantages make them strong candidates for next-generation high-density CubeSat RF subsystems.

Keywords: Ridge Gap Waveguide (RGW), 3D-Printed Technology, CubeSats, and Laser Powder Bed Fusion (LPBF).

3.1 Introduction

With the rapid advancement of Internet of Space (IoS) applications, constellations of thousands of mass-produced CubeSats in Low Earth Orbit (LEO) are providing high-throughput broadband services with low latency (Nasr & Kishk, 2019). Millimeter-wave bands have emerged as promising frequency ranges for future communication systems. The increasing demand for miniaturized solutions with bent structures, low-cost manufacturing, and

easy assembly has driven the development of antenna and passive component structures. These solutions must seamlessly integrate with other subsystems, particularly in space-constrained platforms like CubeSats, to address the specific requirements of these platforms.

Ridge gap waveguide (RGW)-based components provide an ideal solution for designing low-loss, cost-effective antennas and components compared to conventional microstrip line (MSL) and substrate-integrated waveguide (SIW) technologies, particularly at millimeter-wave (mmWave) frequencies. RGW-based components outperform conventional MSL and SIW due to their low loss and high power handling, thanks to the absence of dielectric materials (Nasr & Kishk, 2019). Additionally, RGW technology eliminates the need for direct electrical contact between parts, offering greater design flexibility compared to traditional metallic waveguides (et al., 2019). Components based on RGW are typically fabricated using computer numerical control (CNC) machining. While this method works well for simple structures, it falls short when realizing compact, three-dimensional RGW geometries with complex bends—such as those required in CubeSat subsystems. In contrast, metal additive manufacturing enables the direct fabrication of such intricate designs, which are impractical or unfeasible to achieve using conventional milling techniques.

One potential solution is the use of 3D printing technology, which has recently been employed in fabricating various high-frequency components (et al., 2023c). In contrast to CNC technology, 3D printing enables the production of complex structures and reduces challenges associated with pin fabrication (Tamayo-Dominguez, Fernandez-Gonzalez & Sierra-Perez, 2019). Among current 3D printing methods, laser powder bed fusion (LPBF) stands out due to its full metallic powder-based process, eliminating additional steps like copper electroplating required in other methods such as fused deposition modeling (FDM) and stereolithography (SLA).

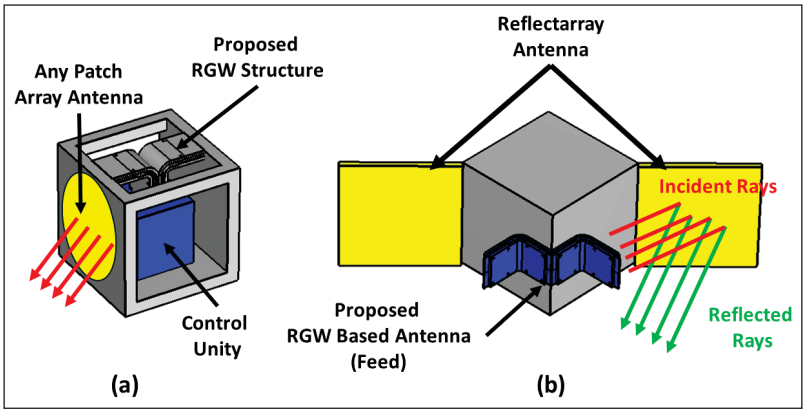

Figure 3.1 Application case and placement of the proposed 90° bent 4-port RGW on a 1U CubeSat (a) Waveguide application (b) Antenna application

Few studies have examined 3D printing for fabricating RGW-based components in mmWave applications. In (Tomassoni, Peverini, Venanzoni, Addamo, Paonessa & Virone, 2020), a monopulse antenna incorporating a radial

line slot array (RLSA) was fed by a 3D-printed RGW-based Butler matrix produced via SLA and coated with copper. Reference (Alonso-González, Rico-Fernández, Vaquero & Arrebola, 2023) introduced 0 dB and 3 dB RGW-based forward couplers, fabricated using SLA and electroplated with a 0.02 mm copper layer. In (Tamayo-Domínguez, Fernández-González & Sierra-Castañer, 2021), a 4 × 4 element cavity slot antenna fed by odd-mode RGW was created using the same SLA and copper plating process. Lastly, Santiago et al. (Beltayib & Sebak, 2019b) proposed a fully metallic 3D-printed low-pass filter based on a groove gap waveguide (GGW), fabricated with LPBF technology using an aluminum alloy powder (ALSi10Mg).

Fully metallic 3D-printed RGW components are rarely explored and are typically limited to simple structures, underutilizing the extensive design flexibility offered by 3D printing. This flexibility is particularly advantageous for the design of 90° bent interconnections and components, including antennas, couplers, and filters, for CubeSat subsystems (Beltayib, Afifi & Sebak, 2019), as depicted in Fig. 3.1, as well as for other systems with limited space. Given the standard CubeSat $10 \times 10 \times 10$ cm^3 dimension, these features require compactness in three-dimensional structures and high-density integrated sub-systems.

Several works on three-dimensional substrate-integrated waveguide bends for reduced-footprint components (Doghri, Ghiotto, Djerafi & Wu, 2014; Khatib, Djerafi & Wu, 2012; Santiago, Laso, Lopetegi & Arregui, 2023; Sun, Cheng, Wang & Fan, 2023), to our knowledge, no RGW-based 90° bent waveguide, passive component, or antennas have been reported.

This letter presents, for the first time, the implementation of a fully metallic 3D-printed technology for the realization of ridge gap waveguide (RGW) antenna and passive components incorporating 90° bends geometries that are inherently challenging to fabricate using conventional subtractive techniques. The presented implementation is particularly well suited for integration within CubeSat platforms, where severe space constraints and the need for high-density packaging impose strict design limitations. Sections II-IV detail the key design principles, additive manufacturing process, experimental validation, and conclusions, respectively.

3.2 Proposed 90° Bent 3D Printed Ridge Gap Waveguide Structures

3.2.1 Design Process

We chose the structure in Fig. 3.2 and Fig. 3.3 to demonstrate the advantages of fully metallic 3D printing, enabling 90° bent RGW-based passive component and antenna fabrication. The design process of the proposed 90° bent RGW structure involved three primary steps:

Step 1: Design a conventional RGW for the target frequency band, then bend the design 90°.

Step 2: Design of the MSL to RGW transition.

Step 3: 3D print the 90° bent RGW components using LBPF technology, then evaluate and analyze the performance.

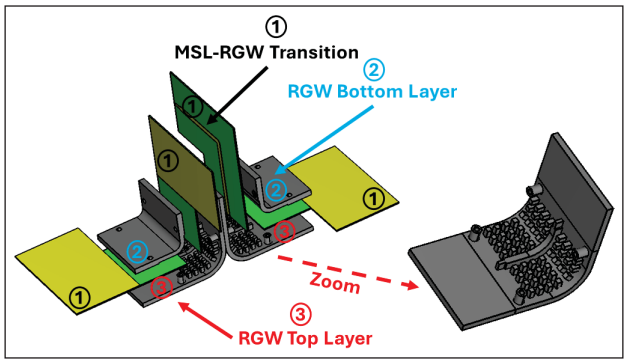

Figure 3.2 3D model of the proposed 90° bent 4-Port 3D Printed RGW

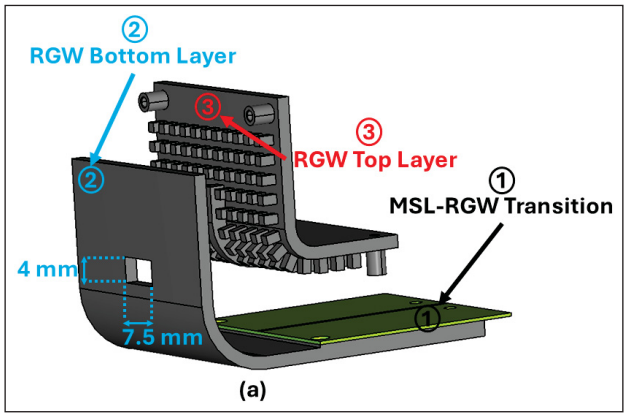

Figure 3.3 Proposed 90° bent RGW slot antenna 3D model

Prior to the design of the proposed 90° bent 3D-printed RGW structures, we utilized a machine learning-based approach described in our previous works (Doghri, Djerafi, Ghiotto & Wu, 2015) to design an RGW unit cell operating from 15 to 30 GHz. The predicted unit cell dimensions are as follows: The gaps have a height of 1 mm, and the period of the unit cell is 4 mm. The width of the pins is 1.5 mm, while the pin height is kept $\approx \lambda_0/4$ (2.5 mm) at 27 GHz. Both the RGW unit cell structure and dispersion diagram are shown in Fig. 3.4. As required, the eigenmode solver for the designed RGW unit cell yields a stop band from 17.5 to 32 GHz (suitable for mmWave applications). The unit cell is then used to design the 90° RGW-based waveguide bend and slot antenna.

In step two, which involves designing the transition from MSL to RGW (see Fig. 3.5 and Fig. 3.6), we propose a transition inspired by the work reported in (Peng, Pu, Wu, Chen & Luo, 2021c; Peng, Pu, Wu & Luo, 2022b; Ren, Zaman, Yang, Vassilev & Bencivenni, 2022). The proposed transition consists of an MSL connected to the RGW via a suspended patch, with the MSL positioned directly on the bottom block, while the suspended patch extends to the end of the ridge.

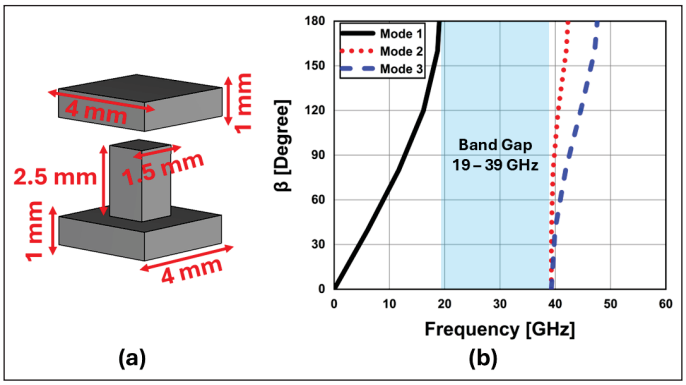

Figure 3.4 The proposed (a) RGW unit cell and (b) dispersion diagram

The 4-port 90° bent interconnection is fed by an L-shaped microstrip line of length 72 mm and width 1.6 mm, realized on Rogers RT/Duroid 5880 substrate (ε_r = 2.2, thickness = 0.508 mm), connected to an optimized suspended patch with a width X_p = 4.23 mm and length Y_p = 3.78 mm, as illustrated in Fig. 3.5. To facilitate measurements using an end-launch connector, the MSL width is tapered and matched through a quarter-wavelength transformer network to ensure smooth impedance transition.

The 90° RGW bent slot antenna is fed by a conventional microstrip line of length 35 mm and width 0.83 mm, realized on Rogers RO4350B substrate (ε_r = 3.66, thickness = 0.254 mm), as shown in Fig. 3.6.

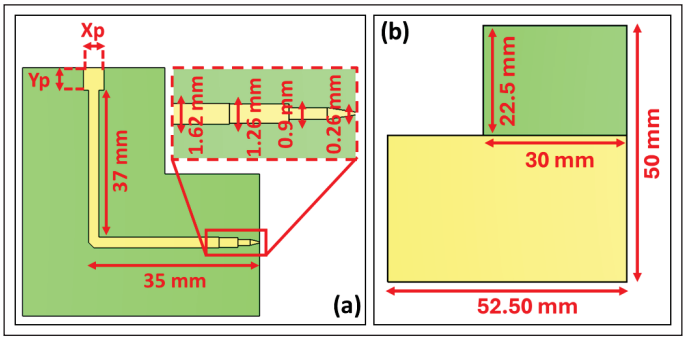

Figure 3.5 The proposed MSL to RGW transition (a) Top view (b) Bottom view

Fig. 3.7 illustrates the 2D electric field (E-field) distribution of the 3D-printed RGW structure with the proposed MSL transition. As can be seen, the electromagnetic (EM) wave propagation is guided from port 1 to the ridge through the MSL, then back to MSL, and lastly to port 2. Consequently, the proposed transition confirms a good fit in the electric field distribution.

Using the pre-designed, 90° bent 2-port RGW structure with the proposed transition, a 90° bent 4-port RGW structure is designed based on two connected 90° bent 2-port RGW structures. To further demonstrate the potential

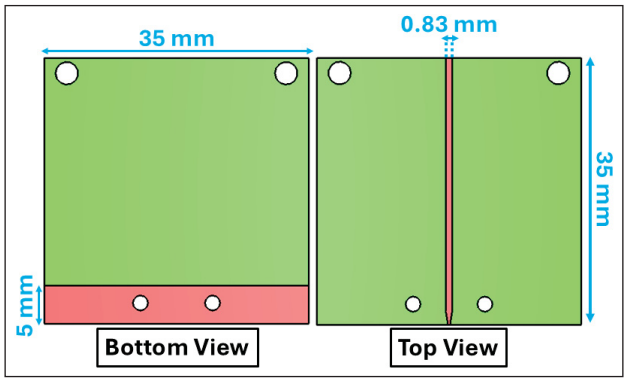

Figure 3.6 Microstrip-to-RGW transition (MSL–RGW) of the proposed 90° bent RGW slot antenna

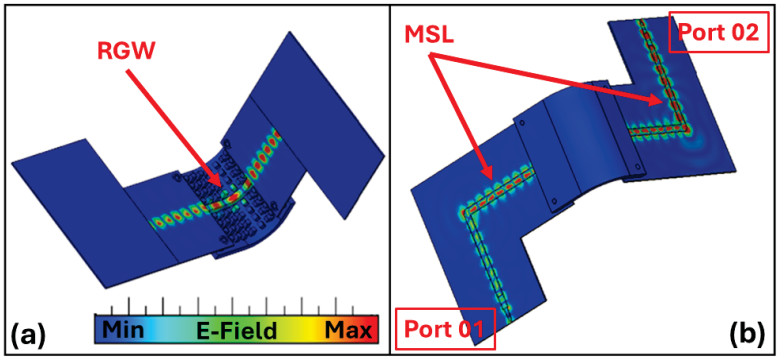

Figure 3.7 E-field distribution at 27 GHz (a) Bottom view (b) Top view

of 3D printing RGW structure, we design and fabricate a 90° bent RGW slot antenna for IoS applications, operating from 27.3 to 28 GHz.

3.2.2 3D-Printed Process

In order to 3D print the proposed 90° bent RGW components, we employ 3D printer machines available in the Shape Memory Alloys and Intelligent Systems Laboratory at École de Technologie Supérieure (ETS). Specifically, the EOSINT M280 and TruePrint Series 1000 machines are utilized, both of which are based on LPBF technology. The AlSi10Mg material is chosen for its low weight, good electrical conductivity, and strong power handling capabilities. The adoption of LPBF technology is motivated by its ability to achieve suitable 3D printing for small components, such as pins, owing to its high tolerances ($\pm 50\ \mu m$). The LPBF technology involves three main steps, as follows (et al., 2017b; Peverini, Lumia, Addamo, Virone & Fonseca, 2023b):

Step 1: The prepared STL files are loaded into the 3D printer, which then generates the path and instructions needed to 3D print the proposed 90° bent RGW structure.

Step 2: Using high-powered lasers, 400 W for the EOSINT M280 and 200 W for the TruPrint 1000, the ALSi10Mg powder is selectively melted layer by layer. This process continues as the building platform gradually lowers until the final part is fully formed.

Step 3: Unused powder is evacuated to the collector platform. Then a stress-relieving post-process using an oven at a temperature ranging from 500 °C to 700 °C is conducted.

Step 4: 3D printed parts are separated from the building platform, and the support structures are detached. Depending on the structure, a polishing process can be applied to the 3D-printed part to enhance the surface roughness which ranges between 3 and 8 μm and quality. However, since the pin in the proposed RGW structure is thin, fragile, and complex, no polishing was conducted.

Fig. 3.8 (a) presents the 3D-printed 90° bent 4-port RGW structure and its different main parts. The connection between the two assembly parts and the proposed MSL transition is established using only four screws, as shown in Fig. 3.8 (b). Furthermore, Fig. 3.9 presents the structure of a 3D-printed 90° bent RGW slot antenna, illustrating its bottom layer with the ridge and bed-of-nails, used MSL, and top layer featuring the slot aperture and bent-waveguide path.

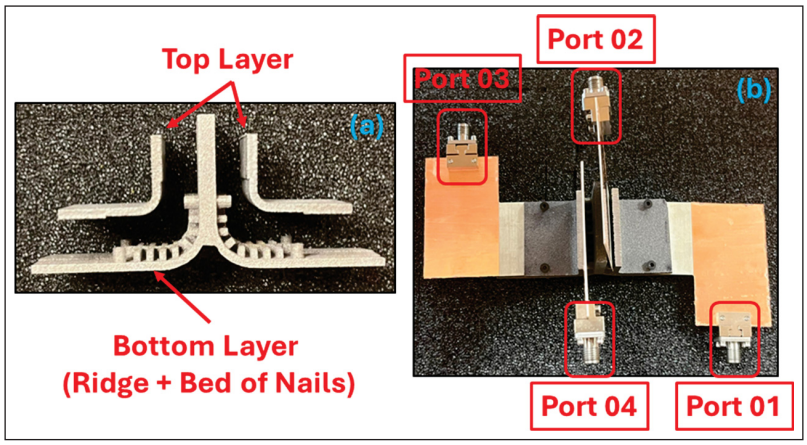

Figure 3.8 3D Printed 90° bent 4-port RGW structure (a) Disassembled without MSL transition (b) Assembled with MSL transition

3.3 Simulation and Measurement Results

3.3.1 90° bent 4-port RGW

We measure the 3D-printed 90° bent 4-port RGW structure using a two-port Agilent PNA-X 67GHz Network Analyzer (VNA) from Keysight available in the Microelectronics and Communications Research Lab (LACIME) at ETS Montreal. We perform the S-parameter measurements sequentially: two ports were connected to the VNA, while the remaining two ports were terminated with 50 Ω loads.

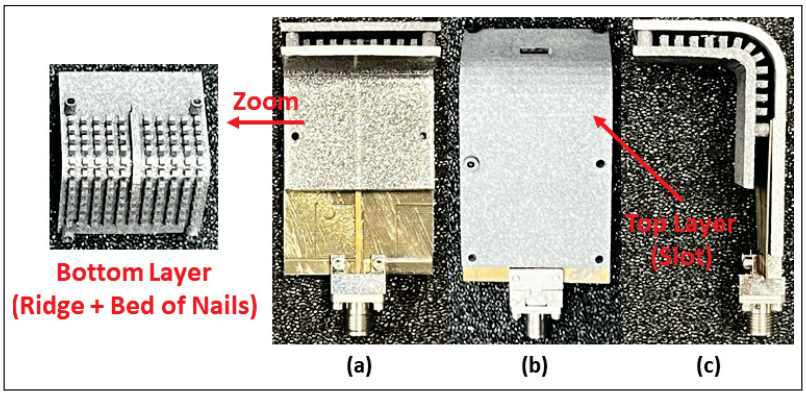

Figure 3.9 3D Printed 90° bent RGW slot antenna (a) Bottom view (b) Top view (c) Side view

Fig. 3.10 (a) depicts the simulated and measured reflection coefficient across the targeted operating frequency from 26 to 28 GHz, demonstrating good agreement between the simulation and experimental results. Notably, the measured reflection coefficient varies between -12 and -30 dB.

Over the same frequency range, isolation between the 4 ports exceeds 40 dB (see Fig. 3.10 (b)), indicating excellent isolation. Fig. 3.11 shows the transmission coefficient results between Port 1 / Port 2 and Port 3 / Port 4. The transmission coefficient $|S_{21}|$ ranges from approximately 1.8 dB to 2.6 dB across the 26–28 GHz band, while $|S_{34}|$ varies from about 2.1 dB to 2.5 dB. To isolate the intrinsic performance of the RGW structure, a reference simulation excluding the transition is included, which shows a transmission coefficient better than 0.5 dB, confirming the low-loss nature of the RGW itself.

The observed additional loss, ranging from 1.5 to 2 dB is attributed to surface roughness, MSL transition effects, possible misalignment during assembly, and surface polishing.

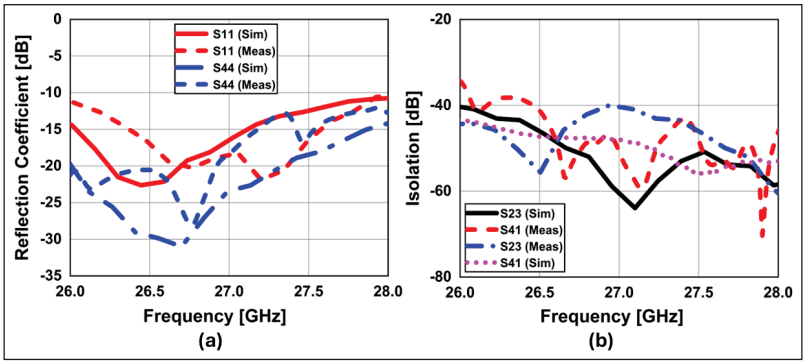

Figure 3.10 Simulated and measured S-parameters (a) Reflection coefficient [dB] (b) Isolation [dB]

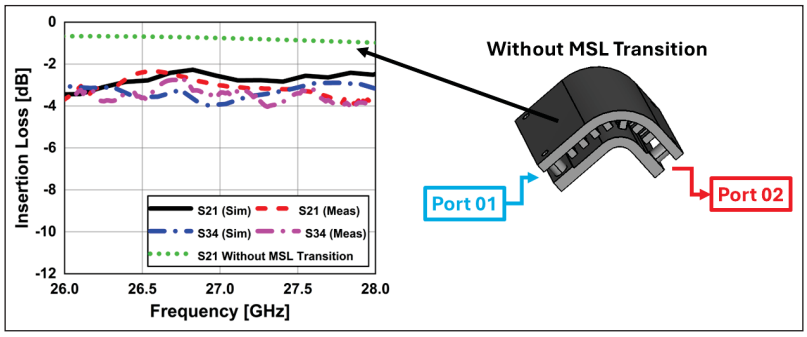

Figure 3.11 Simulated and measured transmission coefficient (S_{21})

3.3.2 90° bent RGW slot antenna

As illustrated in Fig. 3.12(a), the simulated and measured reflection coefficients exhibit a fractional bandwidth from 27.3–28 GHz at $S_{11} \leq -10$ dB. The discrepancy observed between the simulation and measurement results can be attributed to 3D printing process imperfections.

Similarly, Fig. 3.12(b) presents the simulated and measured realized gain and radiation efficiency of the proposed antenna, demonstrating a strong correlation between the two. Within the -10 dB bandwidth (27.3–28 GHz), both the simulated and measured realized gain reach a maximum of 5 dBi at 27.5 GHz, with the simulated values ranging from 4 dBi to 5 dBi and the measured values varying between 3.8 dBi and 5 dBi. The normalized radiation efficiency, ranging from 0 to 1 with an average of 0.78, further validates the antenna's performance. This consistency in performance is maintained despite minor fabrication-related variations such as surface roughness and 3D printing tolerances.

Fig. 3.13 illustrates the radiation pattern cuts in the E and H planes. The measured results demonstrate stable radiation patterns across the entire frequency band, with symmetrical radiation characteristics. A discrepancy between the simulated and measured radiation patterns is observed, which can be attributed to 3D printing tolerances, characteristics, and measurement imperfections.

3.4 Conclusion

This letter demonstrates the viability of fully metallic 3D-printed RGW components with 90° bends for CubeSat integrations. The successful 3D printing and performance validation of both a 4-port waveguide bend and a compact slot antenna for mmWave IoS application (26-29 GHz) confirm the potential of additive manufacturing to realize complex RGW geometries that are otherwise unachievable using conventional techniques.

The results confirm that this approach enables compact, structurally robust, and easily integrable antennas and passive components, making it a promising candidate for high-density CubeSat systems. The proposed 90°

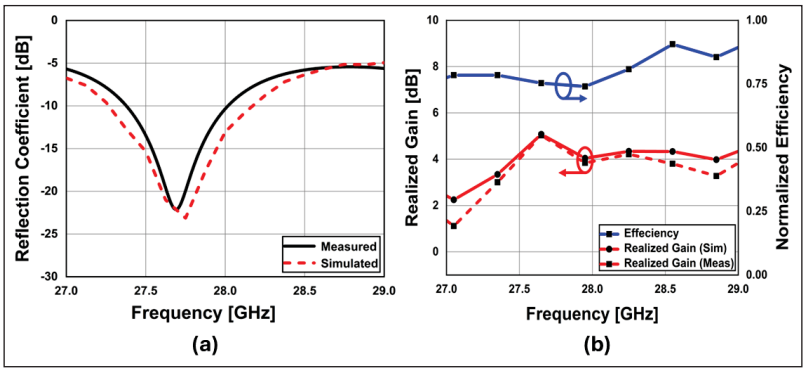

Figure 3.12 Simulated and measured S-parameters: (a) Reflection coefficient [dB], (b) Realized Gain & Efficiency

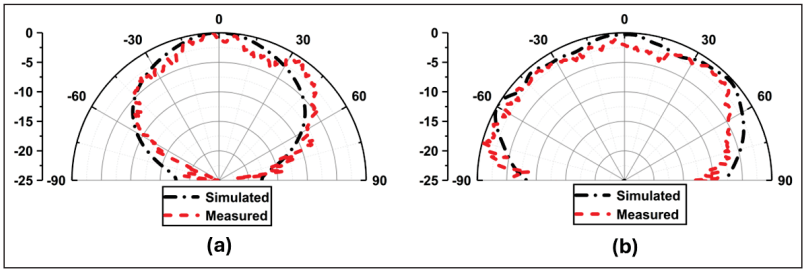

Figure 3.13 Simulated and measured radiation pattern: (a) E-Plane (ϕ = 0°), (b) H-Plane (ϕ = 90°)

bend RGW technology can serve as a foundational platform for the future development of advanced RGW-based subsystems with complex geometries, including couplers, filters, and multi-port antennas.

CHAPTER 4

PRINTED RIDGE GAP WAVEGUIDE SYNTHESIS APPROACH BASED ON GENETIC PROGRAMMING

Mohammed Farouk Nakmouche, Dominic Deslandes, Ghyslain Gagnon

Département de Génie Électrique, École de Technologie Supérieure,
1100 Rue Notre-Dame Ouest, Montréal, Québec, H3C 1K3, Canada

Submitted to the journal
IEEE Journal on Multiscale and Multiphysics Computational Techniques
July 4, 2025.

Abstract: This article introduces, for the first time, a scalable genetic programming (GP)-based approach for the synthesis of a Printed Ridge Gap Waveguide (PRGW) unit cell. The proposed approach is applicable for any given stop-band frequencies ranging from 3 to 300 GHz. GP is used to generate a straightforward mathematical expression to predict the dimensions of the PRGW unit cell in terms of a predefined stop band and used substrate materials. Thus, reliability is improved and computational time is reduced. The proposed approach shows better performance compared to test-and-trial and traditional machine learning techniques in terms of MSE and MAE values as well as computational time. Using the generated mathematical equation, we conducted an experimental validation by designing a two-PRGW-based waveguide specifically for the Internet of Space (12–16 GHz) and mid-band 5G (3–4 GHz) applications. The two waveguides are fabricated and measured. The obtained results confirm the effectiveness of our proposed GP-based design approach in successfully meeting the predefined objectives. The proposed GP-based approach highlights the potential of using GP as an efficient and reliable component and subsystem design process and thus contributes to the various methods used for automatic design and synthesis.

Keywords: Printed Ridge Gap Waveguide, Genetics Programming, Automated Synthesis.

4.1 Introduction

Recently, printed ridge gap waveguide (PRGW), an alternative guiding structure technology to microstrip line (MSL) (Ahmed, Sebak & Denidni, 2012; Ansari, Zhu, Shariati & Guo, 2019) and substrate integrated waveguide (SIW) (Djerafi & Wu, 2007; Geng, Lian, Guo & Ding, 2024; Shen, Wang & Zhang, 2018), has been widely adopted in various component designs (Ali & Sebak, 2018; Ali, Afifi & Sebak, 2020b; Chen, Chen & Hong, 2022a; Chen, Chen, Zhou, Wen & Hong, 2024a). The PRGW allows the propagation of quasi-TEM waves in the center region, consisting of an upper plate and a MSL placed above the artificial magnetic conductor (AMC) surface (Shams & Kishk, 2017b), as shown in Fig. 4.1. The AMC surface, based on a 2D periodic Electromagnetic

Band Gap (EBG) unit cell, creates an AMC boundary condition over a limited frequency range, called stop band (Sievenpiper, Zhang, Jimenez-Broas, Alexopolous & Yablonovitch, 1999). Within the stop band, no propagation of any PEC–AMC parallel-plate modes exists when the height of the air gap is a quarter of a free space wavelength (Berenguer, Fusco, Zelenchuk, Sánchez-Escuderos, Baquero-Escudero & Boria-Esbert, 2016c).

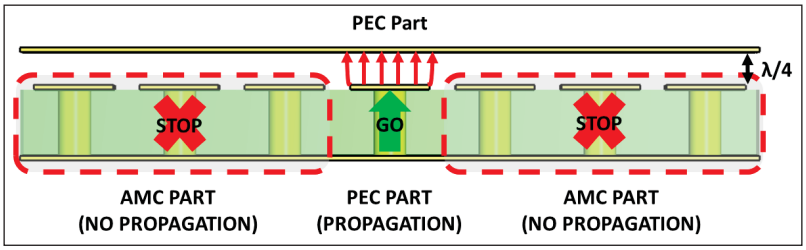

Figure 4.1 The PRGW working principle

As it can be seen, the AMC surface is the main block of PRGW guiding structure, as the operating frequency band that allows quasi-TEM mode propagation is determined by the stop band of the AMC surface. Therefore, an appropriate design of the PRGW unit cell is essential in order to meet the target application bandwidth.

Designing PRGW-based components, including antennas, filters, and couplers, across different target operating frequency bands presents significant computational challenges. This is because the conventional trial-and-test approach involves numerous variables, multiple objectives, and constraints, all of which necessitate several electromagnetic (EM) iteration steps (et al., 2021; Ma, Dang, Watkins, Morris & Beach, 2023).

In pursuit of computational cost reduction and reliability improvements, various machine learning (ML)-based approaches have been successfully implemented for antenna and circuit design applications (Feng, Na, Jin, Zhang, Zhang & Zhang, 2022; Misilmani, Naous, Khatib & Salwa, 2020b; Vai & Prasad, 1993; Zhang, Wei, Kang & Yin, 2024). This is due to its exceptional ability to solve multi-dimensional and multi-objective problems easily.

It has been shown in reported studies that a well-trained ML model is able to rapidly and effectively predict the behaviors of antennas and circuits exhibiting similar characteristics (Creech, Paul, Lesniak, Jenkins, Lee & Calcatera, 1996; Jin, Zhang, Feng, Na, Ma & Zhang, 2019; Watson & Gupta, 1996a,9). Engineers can thus have a computationally efficient workflow based on EM simulations aided by well-trained ML models.

Genetic programming (GP), a symbolic regression method, has recently been used in various engineering applications (Hosseini & Nemati, 2015). GP is an extension of the genetic algorithm introduced by Koza (Koza, 1992), which is based on the biological evolution processes of selection, mutation, and crossover.

Compared to conventional ML-based approaches, which primarily involve optimizing parameters to fit a pre-specified model structure, GP seeks to derive both the model and the suitable parameters directly from the dataset

(Scikit-learn Community, Accessed 2025a), thereby reducing computational time. Additionally, GP provides a mathematical representation of the derived model and its parameters (Scikit-learn Community, Accessed 2025b), which are straightforward for humans to understand and interpret. Thus, GP enhances model interpretability, making the reasoning behind predictions clearer.

In the field of EM antenna and circuit design, no prior applications of GP have been reported to the best of the author's knowledge. In this paper and for the first time, a GP-based approach is used for PRGW synthesis in terms of target stop band frequency. This work proposes a scalable, straightforward mathematical expression for PRGW dimension calculation in terms of the used dielectric material and any given frequency band ranging from 3 to 300 GHz.

To demonstrate the effectiveness of the proposed approach, we conduct a detailed analysis in terms of mean square error (MSE), mean absolute error (MAE), and computational time. We then compare it with the conventional test-and-trial process and other frequently used ML-based approaches. Finally, we design, fabricate, and measure two PRGW guiding structures for the Internet of Space (IoS) and mid-band 5G applications to validate the proposed GP-based approach.

The paper is organized as follows: Section II presents the problem description; Section III details the proposed GP-based approach; and Section IV conducts the experimental validation, which includes the design, fabrication, and measurement of two guiding structures as validation examples. Section V concludes the paper.

4.2 Problem Description

Studies conducted on the behavior of PRGW unit cells (Rajo-Iglesias & Kildal, 2011b; Rajo-Iglesias, Caiazzo, Inclán-Sánchez & Kildal, 2007b) revealed that the PRGW unit cell's primary parameters, depicted in Fig. 4.2, impact the stop band frequency as follows:

- The thickness of the "Gap Substrate" (H_{gap}) influences the end frequency (F_{Top}) of the stop band.
- The period W between neighboring patches has no significant effect on the stop band for small values of H_{gap}. While at a high value of H_{gap}, it effects the stop band.
- The radius of the via impacts both start and stop frequencies, causing them to move in the same direction while having no effect on the width of the stop band.
- The thickness of the 'Main Substrate' (H_{sub}), in which the via is embedded, has a direct effect on the start frequency (F_{Low}) of the stop band. The thicker the substrate, the lower the frequency.

- The dielectric constants ϵ_{r1} and ϵ_{r2} related to the "Main Substrate" and the "Gap Substrate," respectively, influence the width of the stop band.

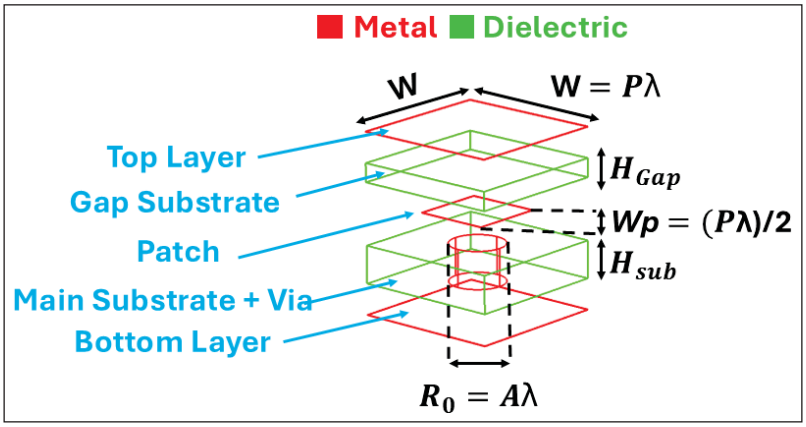

Figure 4.2 Unit cell of the PRGW

Identifying the key parameters influencing the unit cell does not directly enable a straightforward design process; consequently, most reported works rely on a test-and-trial approach. The design process begins with the identification of the start (F_{Low}) and stop (F_{Top}) frequencies appropriate for the target application. Afterward, a parametric study is conducted to update the physical parameters of the PRGW unit cell through many iterations. Finally, the first three propagating modes are calculated and plotted in each iteration, and the process stops when the targets F_{Low} and F_{Top} are achieved. However, as shown in [29–30], engineers and researchers typically use repeatedly well-known, reported unit cells. This is because the test-and-trial approach is time-consuming and labor-intensive, as EM simulators typically run slowly and the number of EM iteration steps can be large.

The objective of this paper is to predict, using GP, two continuous values (A and P) that are related to period (W) and radius of the via (R_0) as shown in Fig. 4.2. The prediction is conducted using predefined input variables:F_{Low}, F_{Top}, H_{sub}, H_{gap}, ϵ_{r1}, ϵ_{r2}.

4.3 Genetics Programming-Based Synthesis Approach

GP is a symbolic regression technique that directly derives both the model and its parameters from the dataset. In contrast, the conventional regression techniques primarily focus on optimizing parameters to fit a predefined model structure. In other words, GP aims to find a mathematical expression that best fits the input and outputs of any given dataset automatically. It represents the solution mathematically and as a tree representation, as shown in Fig. 4.3 using arithmetic operations (+,-, /, ×), trigonometric functions (sin, cos, tan, exp, tanh, log), or boolean operators.

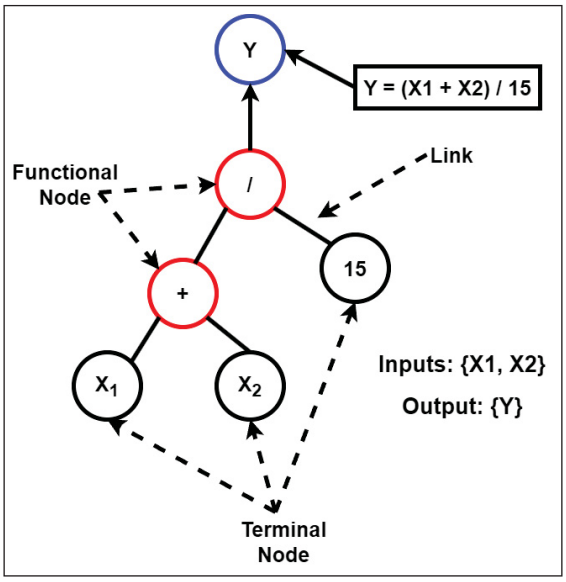

Figure 4.3 Example of a GP tree representation

As shown in Fig. 4.4 (Gandomi, Alavi & Ryan, 2015; Langdon, Poli, McPhee & Koza, 1997), the GP algorithm starts by creating an initial random population of potential solutions, typically in the form of symbolic mathematical expressions and tree representation. Through a process of selection, crossover, and mutation, these models evolve over generations. Each generation creates new models or mathematical expressions by combining successful elements, introducing variation through mutation, and selecting the best-performing ones to form the next generation. This iterative process continues until a suitable model or mathematical expression that fits the dataset is found.

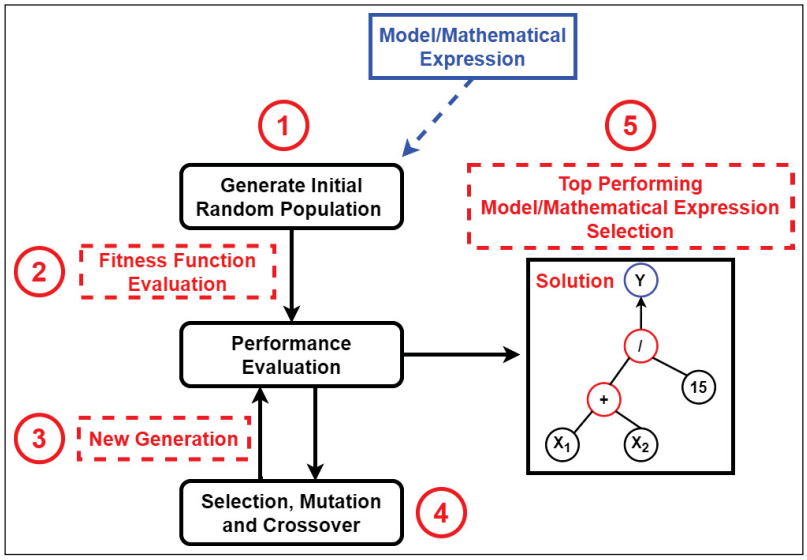

Figure 4.4 Flowchart of GP-based approach

4.3.1 Proposed GP-Based approach

As in any ML-based approach, the first step consists of splitting the dataset into training and testing sets. The training set generates the model/mathematical symbolic representation, and the testing set validates its generalization ability. In this work, a total of 2480 samples were generated, with 1984 (80%) sets of samples for training purposes and 496 (20%) sets of samples unseen during the training phase, which was employed for model performance validation. The dataset generation approach is described in Algorithm 3.

Algorithm 3 Data Generation Process

1: Set the boundary condition

2: Apply Periodic boundary conditions along the longitudinal and lateral directions.

3: Apply PEC on top and bottom surfaces.

4: Set dielectric constant for ϵ_{r2}= [3.66 (RO4350), 2.2 (RO5880), 6 (RO3006) and 3 (RO3003)].

It is noteworthy to mention that the selected ϵ_{r2} are based on reported studies and fabrication capabilities to process the materials to embed plated vias.

5: Set dielectric constant for ϵ_{r2} = [3.66 (RO4350), 2.2 (RO5880), 6 (RO3006) and 3 (RO3003)].

6: Set the physical dimensions of the PRGW as follows:

- Set H_{gap} = [0.252, 0.508, 0.762, 1.52] in mm.
- Set the A to vary from 0.1 to 0.3.
- Set the P to vary from 0.025 to 0.075.
- Set H_{sub} = [0.252, 0.508, 0.762, 1.52] in mm.
- Set λ_0 = [29.27, 19.98, 13.32, 9.01, 1.81] in mm.

The values of A and P are based on the analysis in [27, 28]. Meanwhile, H_{gap}, H_{sub}, ϵ_{r1}, and ϵ_{r2} correspond to standard materials from literature, though alternative materials are also applicable. Lastly, λ_0 is selected randomly for each frequency band between 3 and 300 GHz.

7: Run the eigenmode solver.

8: Calculate the three first propagating modes.

9: Extract and plot the dispersion diagram.

10: Identify the upper frequency F_{Top} and lower frequency F_{Low}.

11: Repeat steps 4-7 while varying the combinations associated with the physical dimensions of the PRGW unit cell.

12: Organize the dataset as inputs and outputs.

Now, using the generated dataset, we employ a GP algorithm to derive a model and a mathematical expression that represents the relationship between the input and output variables of the dataset. This approach is capable of evolving mathematical expressions and tree representations that best capture the underlying data structure. The

generated mathematical expressions of the tree representations for both A and P, shown in Fig. 4.5, are expressed as follows:

$$P = \frac{0.189}{\epsilon_{r2}} \tag{4.1}$$

$$A = 0.164 \tag{4.2}$$

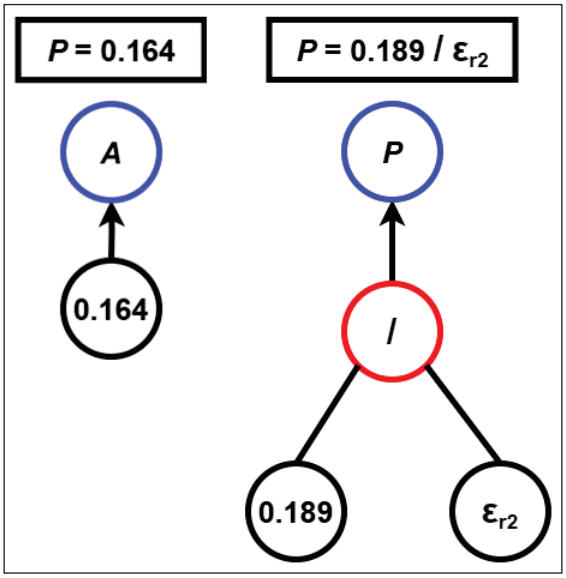

Figure 4.5 GP Tree of the generated solution

Using this mathematical equation, we can easily calculate the PRGW unit cell's physical dimensions for any targeting stop band ranging from 3 to 300 GHz, depending on the input specification following the GP-based approach summarized in Algorithm 3.

Algorithm 4 Proposed ML-Based Synthesis Approach

1: Define target stop band (F_{Low} and F_{Top}).

2: Define dielectric material for main substrate and gap substrate

3: Calculate the PRGW unit cell physical dimensions (h, g, R_{via} and d) using the generated GP equation.

4: Run the eigenmode solver automatically using VBA macro programming code.

5: Calculation of the three first propagating modes.

6: Plot the dispersion diagram and extract the stop band frequency.

7: Validate the results with the trained GP model and predefined target objective given by the engineer as input. Evaluate the results with the results from the trained GP model and the predefined stop band given by the engineer.

8: Execute the transient solver-based analysis.

9: Extract the required performance results of PRGW-based components.

4.3.2 Feature Sensitivity Analysis

To further validate the physical consistency and interpretability of the GP-generated equations, we evaluate the contribution of each input feature using permutation-based sensitivity analysis.

This approach tests whether the learned expressions reflect the dominant variables in the dataset. Each feature is independently shuffled while keeping the others fixed, and the resulting increase in prediction error, measured by the mean absolute error (MAE), is recorded. A higher MAE increase indicates greater model dependence on that feature. Accordingly, features with larger MAE shifts are deemed more influential, while those with smaller shifts are considered less significant.

As shown in Fig. 4.10 (a), permutation importance analysis identifies F_{Top}, F_0, and F_{Low} as the most influential features for predicting P, followed by ε_{r2}. This result may initially appear inconsistent with equation (1), where P depends solely on ε_{r2}.

To clarify this discrepancy and support the symbolic expression's validity, we examine the correlation heatmap in Fig. 4.7. It reveals that ε_{r2} is moderately correlated with both F_{Top} and F_{Low}, while these frequency features themselves exhibit strong intercorrelations. Because permutation importance measures the effect of randomly

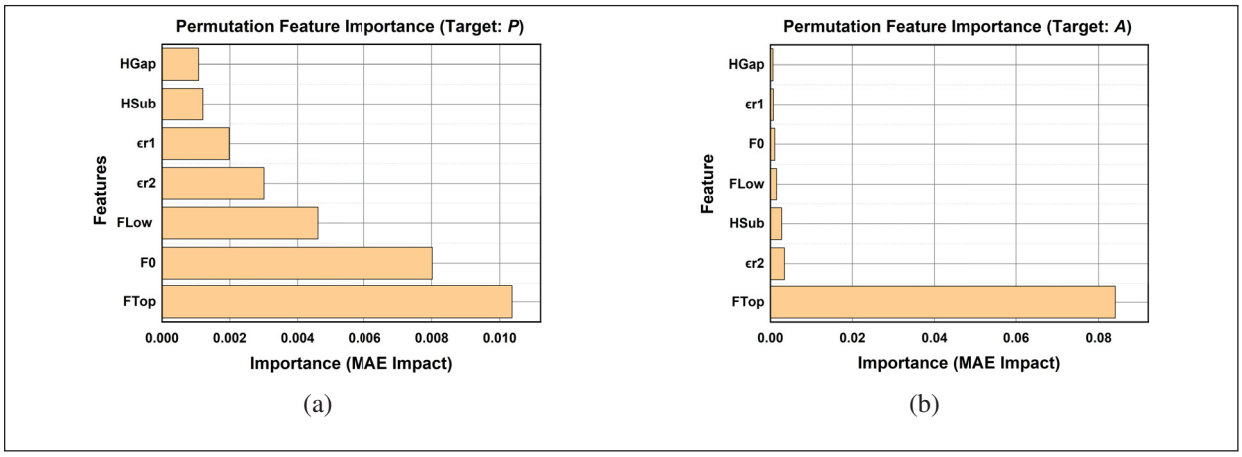

Figure 4.6 MAE Between original and perturbed predictions (a) for P (b) for A

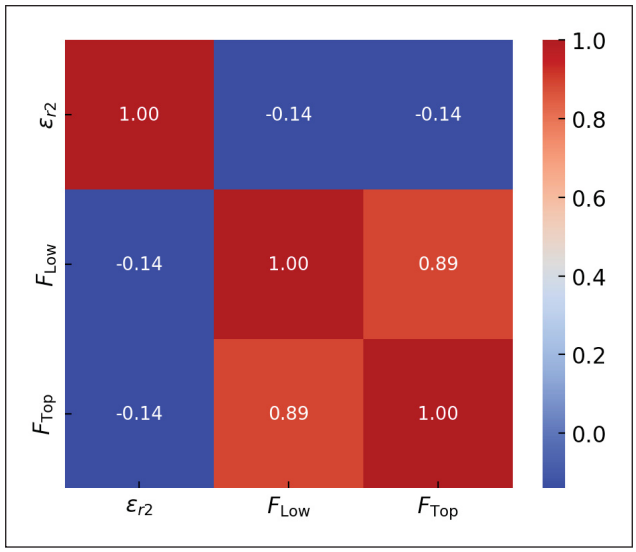

Figure 4.7 Correlation heatmap between ε_{r2}, F_{Low} and F_{Top} in the permutation sensitivity analysis of P

shuffling a feature on model accuracy, disrupting any of these correlated inputs impacts the model's internal structure and predictive power, even if some do not explicitly appear in the symbolic equation.

This analysis confirms that the GP-derived expression accurately captures the fundamental physical dependency. While permutation importance reflects the model's sensitivity to correlated predictors, the GP formulation reveals the true underlying physical relationship, thereby confirming the model's consistency and interpretability.

For target A, Fig. 4.10 (b) indicates minimal sensitivity across all features, which aligns with the GP-generated constant value in (2). The uniformly low MAE impact confirms that A remains invariant with respect to the input parameters within the explored design space.

Overall, the permutation-based analysis not only corroborates the symbolic GP equations but also highlights the robustness and physical relevance of the proposed modeling framework for practical design applications.

4.3.3 Performance Analysis

The performance or quality of a generated model/mathematical equation is evaluated through its fitness function value, which assesses how well the model aligns with the provided dataset and generalizes to new data. The evaluation of fitness varies depending on the specific problem, and the choice of fitness function greatly influences GP performance. GP employs various fitness functions, including Root Mean Squared Error (RMSE), Mean Squared Error (MSE), Mean Absolute Error (MAE), and Coefficient of Determination (R^2) value. In this paper, we choose to validate our proposed GP performance using both MSE and MAE, as defined below.

$$\text{MAE} = \frac{1}{M}\sum_{m=1}^{M}\left|y_{\text{true}(m)} - y_{\text{pred}(m)}\right| \tag{4.3}$$

$$\text{MSE} = \frac{1}{n}\sum_{i=1}^{n}(y_{\text{true}(i)} - y_{\text{pred}(i)})^2 \tag{4.4}$$

It's important to note that choosing the initial population size requires careful attention to attain a balance between computational time, performance evaluation, and optimal model identification. Thus, we investigate using GridSearchCV (Scikit-learn Community, Accessed 2025c), MSE, and MAE scores for different initial population sizes, as shown in Figs. 4.8 and 4.9. GridSearchCV is a hyperparameter tuning technique that consists of training the model iteratively on a specified range of parameters. This approach enables us to evaluate the model's performance with each parameter combination and determine the optimal values that yield low MAE and MSE values.

The results in Figs. 4.8 and 4.9 show the relationship between population size (64 to 1024) and the performance metrics MSE and MAE for *Coeff P* and *Coeff A*. Both coefficients stabilize at population sizes of 512 and higher, indicating that the optimization process has converged and further increases yield minimal improvements.

The stabilization of MSE at 512 suggests that the model has successfully minimized large errors and is consistently performing well. While MSE is more sensitive to outliers, this stabilization indicates that the model has achieved an optimal balance between accuracy and computational cost. Similarly, the stabilization of MAE indicates consistent average error between predictions and actual values. Beyond this point, increasing population size provides only marginal improvements, making a population size of 512 the efficient choice for both coefficients.

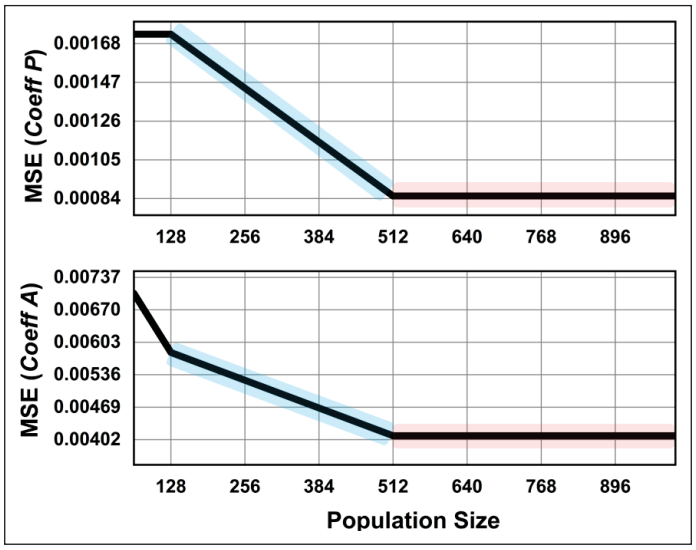

Figure 4.8 MSE value in terms of various population sizes for P and A

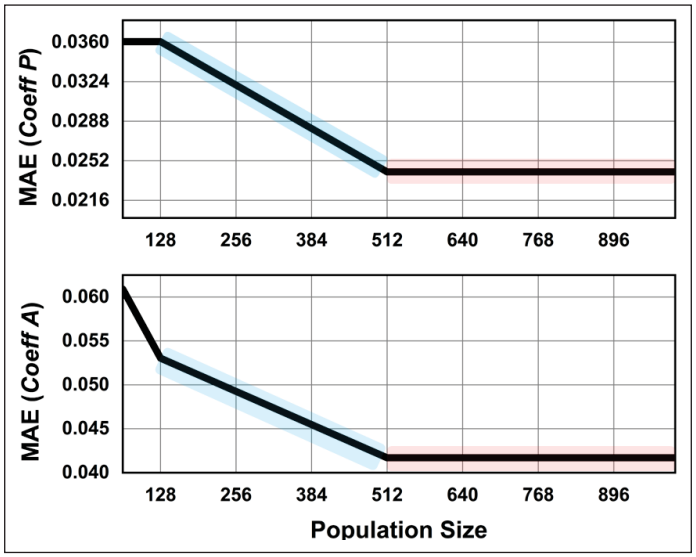

Figure 4.9 MAE value in terms of various population sizes for P and A

4.3.4 Sensitivity Analysis

To evaluate the model's robustness, we performed the Monte Carlo Sensitivity Distribution analysis, which involved introducing random noise to the dataset and computing the MAE between original and perturbed predictions across multiple simulations.

For target P as shown in Fig. 10 (a), the sensitivity distribution shows a similar behavior, with the MAE values clustering tightly around 0.00090. The distribution is slightly more compressed, indicating even higher stability in

predictions for *P*. The low MAE values further reinforce the model's robustness and consistency, indicating that small perturbations in the input features have minimal impact on the model's performance.

For target *A*, as shown in Fig. 10 (b), the Monte Carlo sensitivity analysis reveals a narrow MAE distribution, with most values clustering around 0.0105. This indicates that the trained model and derived equation exhibit stability against small input perturbations, confirming low sensitivity.

Both distributions demonstrate the model's resilience to noise and its ability to maintain accurate predictions even under small changes to the input features.

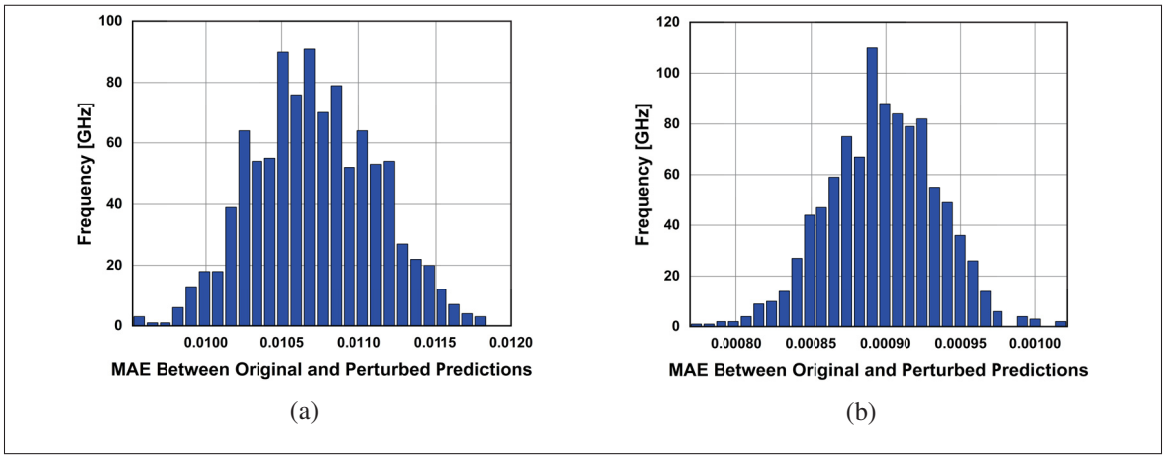

Figure 4.10 MAE between original and perturbed predictions (a) for *A*, (b) for *P*

4.3.5 Computational Efficiency and Time Analysis

We further evaluate the computational time to demonstrate the superiority of our proposed GP-based approach over the test-and-trial approach for the following objectives: (F_{Low}) = 18 GHz and (F_{Top}) = 32 GHz.

Table 4.1 Comparing optimization algorithms: evaluating MSE, MAE, data, and computational time

Algorithms	**Test/Trail**		**GP**		**Random Forest**		**Ridge Regression**		**Linear Regression**	
Target parameters	**A**	**P**	**A**	**P**	**A**	**P**	**A**	**P**	**A**	**P**
Average MSE	NA	NA	0.0041	0.001	3.08	4.62	7.5	4.69	4.24	4.62
Average MAE (%)	NA	NA	0.0417	0.0277	1	2.52	1.5	2.56	1.18	2.53
Data Generation Time	NA	NA	84 hours		120 hours					
Computational Time	2-48 hours		1 minute							

As shown in Table 4.1, the proposed approach makes predictions in less than one minute. In contrast, the test-and-trial method demands hours of simulation, with the simulation time varying based on the available computational power and the designer's level of expertise.

It should be noted that the dataset used for training was generated through 84 hours of full-wave simulation. This process is commonly employed in ML applications for electromagnetic (EM) problems. Unlike the continuous computational demands of the trial-and-error approach, this single computational expense is incurred only once. Furthermore, it is notably lower compared to the 120 hours required to generate large datasets for random forest, ridge regression, and linear regression. All computations are executed on a Lenovo ThinkStation P320 workstation, featuring a 12th Gen Intel® Core™ i7-12700K Processor with vPro®, 32 GB RAM, and an NVIDIA® T1000 4GB GPU.

4.3.6 Implementation Workflow

In this section, we outline the implementation workflow for the proposed GP-based approach. To design a unit cell tailored to a target frequency band, we follow the procedure shown in Fig. 4.11, which is based on the mathematical equations (1) and (2). The steps involved include:

1. Define the F_{Low} and F_{Top} covering the target frequency band applications.
2. Define ϵ_{r1}, ϵ_{r2}, H_{sub} and H_{gap} related to the used materials for "Gap substrate" and "Main Substrate".
3. Using either the generated equation or equivalent model, predict or calculate both A and P which are related to the via's radius and period (W) values.

4.4 Experimental Validation

In this section, we employ the proposed GP-based approach to design a two-PRGW-based waveguide tailored for IoS and mid-band 5G applications. Subsequently, a fabrication and measurement process is conducted to validate the effectiveness of our derived GP-based equations. The two structures are designed to meet the following design objectives:

1. Example I: 90° PRGW structure, operational between 12 and 15 GHz.
   - PRGW unit cell operates within the 8–15 GHz frequency range.
   - Maintains a return loss (S_{11}) < -15 dB across the 12–15 GHz band.
   - Exhibits an insertion loss (S_{21}) ≥ 2 dB within the operational frequency band.
2. Example II: Classic PRGW structure, operating between 3 and 4 GHz.
   - PRGW unit cell operates within the 3–8 GHz range.
   - Achieves a return loss (S_{11}) < -15 dB across the mid-band 5G band.
   - Demonstrates an insertion loss (S_{21}) ≥ 2 dB within the operational frequency band.

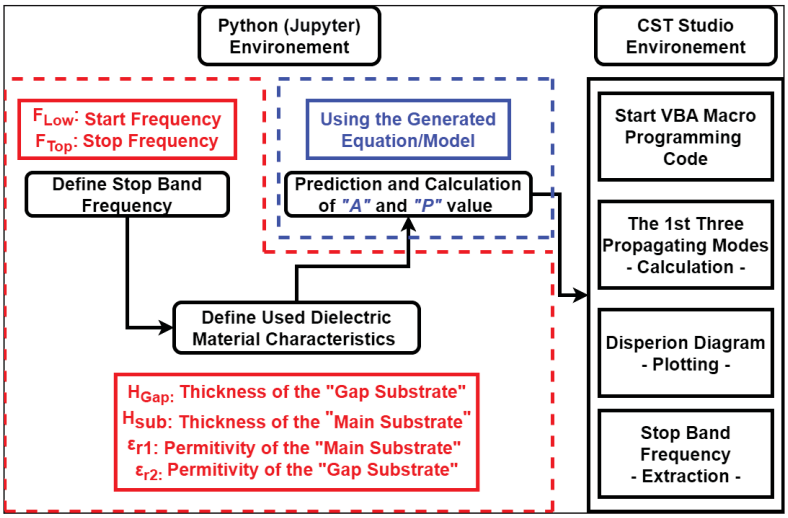

Figure 4.11 Implementation Workflow of the proposed GP-based equation/model

4.4.1 Design I

Fig. 4.12 shows the dispersion diagram, predicted PRGW unit cell geometrical dimensions, and suitable material that achieves the target stop band frequency (8–15 GHz). We utilized RO4350 material for the ”Main Substrate” and RO3006 for the ”Gap Substrate,” with thicknesses of 0.25 mm and 1.52 mm, respectively. Now the PRGW unit cell is used for a 90° waveguide design and fabrication, as shown in Fig. 4.13. In Fig. 4.14, we present the simulated and measured reflection and transmission coefficients of the fabricated PRGW structure.

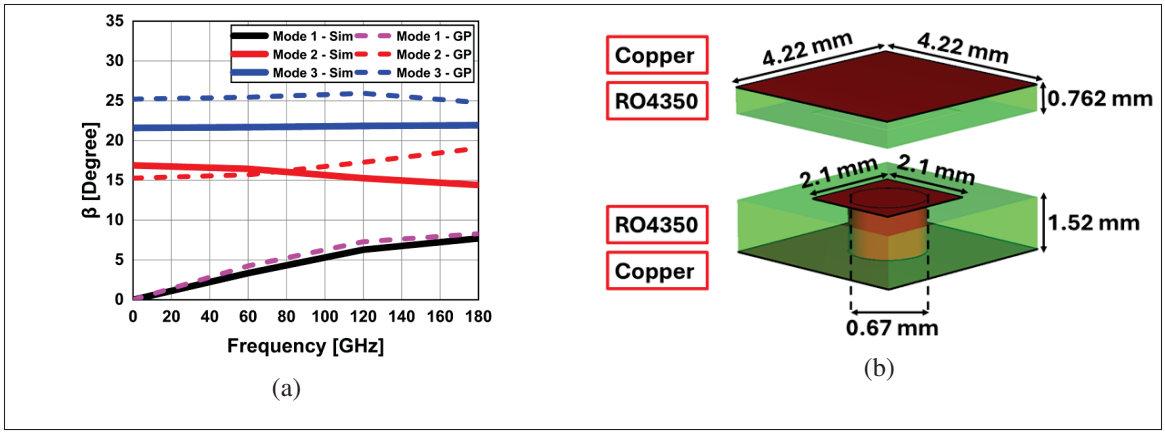

Figure 4.12 The proposed unit cell for IoS band application (a) Dispersion Diagram (b) Predicted Unit Cell

Referring to Fig. 4.14 (a) and Fig. 4.14 (b), it is clear that S11 < -15 dB, while S21 fluctuates between ≈ 0.8 and ≈ 2.2 dB, respectively. The simulated and measured results confirm the efficiency of our proposed GP-based approach in successfully meeting the predefined objectives for "Design I."

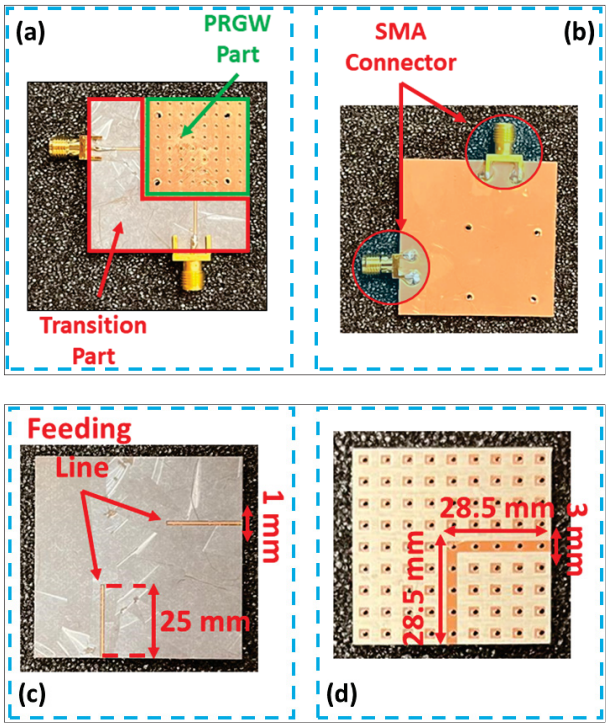

Figure 4.13 The fabricated 2-port PRGW for IoS application: (a) Bottom Layer (b) Top Layer (c) Gap layer with feeding MSL (d) Main layer with PRGW with EBG

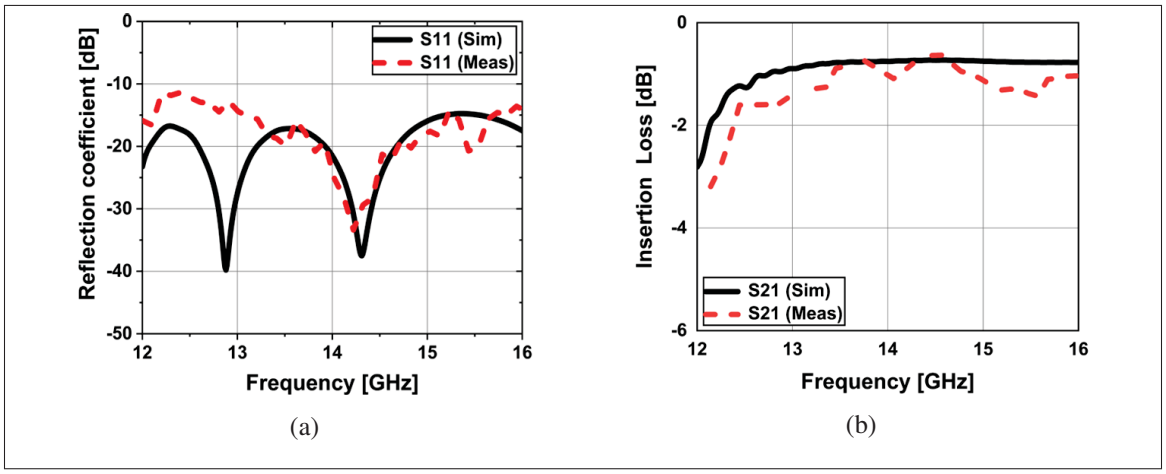

Figure 4.14 Simulated and measured S-parameters for the IoS band application (a) Reflection Coefficient [dB] (b) Insertion Loss [dB]

4.4.2 Design II

To further demonstrate the effectiveness of our GP-based approach, we employed it to predict the physical dimensions of a unit cell for various stop band frequencies ranging from 3 to 8 GHz.

The unit cell comprises two layers based on standard RO4350 dielectric material used to print the mushroom/ridge and RO3006 used as the gap layer. The predicted physical dimension of the unit cell with its related dispersion diagram using the GP-based equation for the mid-band 5G unit cell is shown in Fig. 4.15.

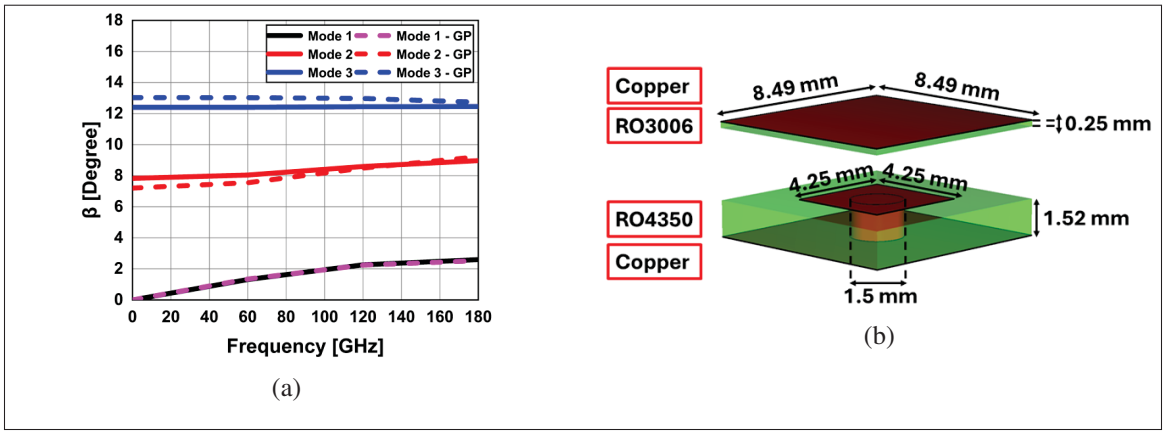

Figure 4.15 The proposed unit cell for mid-band 5G application (a) Front View (b) Back View

We design and fabricate a waveguide with a frequency band from 3.25 to 4.25, suitable for mid-band 5G band applications, using the predicted PRGW unit cell design, as illustrated in Fig. 4.16. Using the same measurement setup employed previously, the achieved reflection coefficient is < -15 dB (see Fig. 4.17 (a)), with the insertion loss between ≈ 0.8 dB and ≈ 2 dB (see Fig. 4.17 (b)). Once again, the achieved outcomes meet the target objectives and confirm the effectiveness of our proposed GP-based approach.

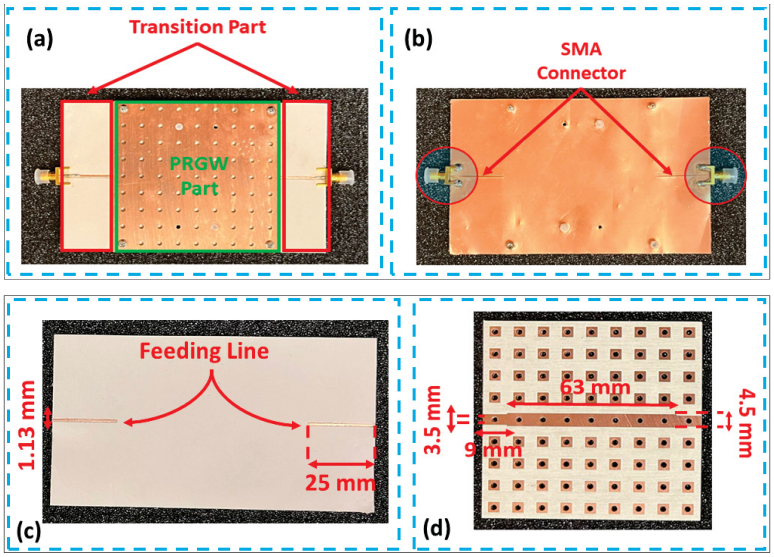

Figure 4.16 The fabricated 2-port PRGW for Mid-Band 5G application (a) Bottom Layer (b) Top Layer (c) Gap layer with feeding MSL (d) Main layer with PRGW with EBG

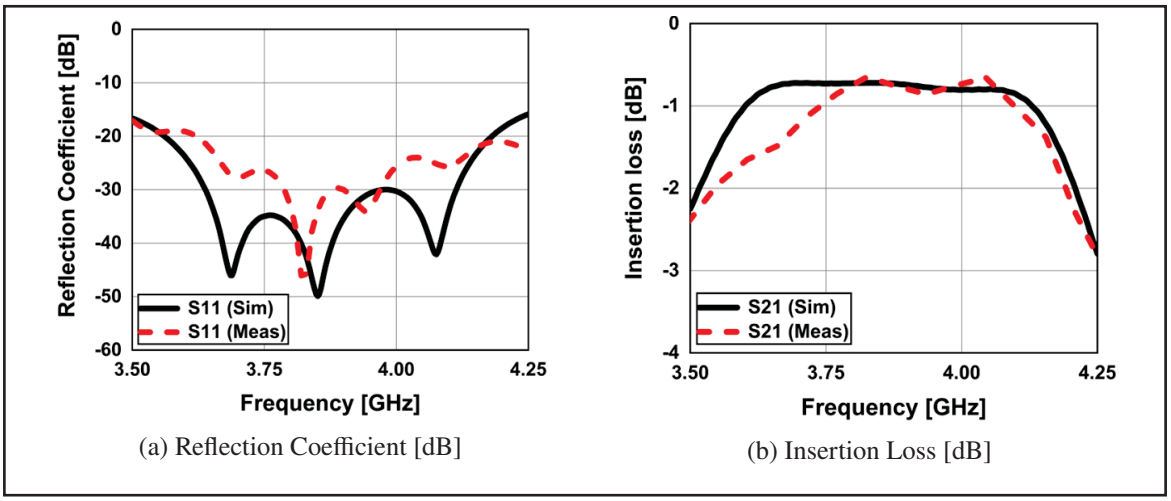

(a) Reflection Coefficient [dB]

(b) Insertion Loss [dB]

Figure 4.17 Simulated and measured S-parameters for the mid-band 5G application

4.5 Comparative Study

Table 4.2 presents a comparative analysis between the reference stop-band frequencies of PRGW unit cells reported in the literature and those predicted using the proposed GP-based synthesis approach. This approach utilizes both a trained GP model and its derived mathematical expressions. The comparison examines a wide range of frequency bands, incorporating both the predicted and simulated stop-band limits and the corresponding physical parameters for each unit cell configuration. The results demonstrate the model's ability to generalize across different substrate materials and dimensional settings while maintaining high predictive fidelity.

As shown in Table 4.2, the predicted stop-band frequencies (F_{Low} and F_{Top}) exhibit good agreement with the target stop-band found in the literature, with deviations remaining within acceptable engineering tolerances. It is worth noting that the actual operating frequency bands of the antennas in these references are considerably narrower than their corresponding EBG stop bands. For example, the antennas in (Ali *et al.*, 2020b), (Al-Alem, Sifat, Antar & Kishk, 2023b), and (Sokunbi & Kishk, 2023) operate over 26–34 GHz, 28–32 GHz, and 50–70 GHz, respectively. Likewise, (Nakmouche, Deslandes, Nedil & Gagnon, b) and (Chen, Chen, Zhou, Wen & Hong, 2024b) report operational bands of 5–16 GHz and 24.17–30.14 GHz. Despite slight deviations between the predicted and target stop-band frequencies, the predicted stop-band fully encompasses the antenna operating bands in all cases.

These findings confirm that the proposed GP-based synthesis approach accurately and efficiently predicts PRGW unit cell dimensions tailored to specific band requirements. By leveraging symbolic regression instead of exhaustive full-wave optimizations, the method enables a fast and scalable design pipeline for the PRGW unit cell, the fundamental building block of PRGW-based components used across various technologies and operating frequency bands.

Table 4.2 Comparison of standard PRGW unit cell physical dimensions with our predicted GP-based approach

Target Stop Band Frequency [GHz]	**Predicted Stop Band Frequency [GHz]**	**Calculated Stop Band Frequency [GHz]**	**Unit Cell Physical Dimension [mm]**							
			Gap Substrate	***Main Substrate***	H_{gap}	H_{sub}	**Predicted *A***	**Calculated *A***	**Predicted *P***	**Calculated *P***
24-40 [6]	22.22-48.27	22.02-48.06	RT6002 (ε_2 = 2.94)	RT6002 (ε_1 = 2.94)	0.254 mm	0.762 mm	0.16446793	0.164	0.06419278	0.0643
23-48 [32]	26.5-52.95	26.57-52.70	RT6002 (ε_2 = 2.94)	RT6002 (ε_1 = 2.94)	0.508 mm	0.762 mm	0.16446793	0.164	0.06419278	0.0643
49-98 [33]	48.13-120.44	48.25-120.82	RO5880 (ε_2 = 2.2)	RT6002 (ε_1 = 2.94)	0.6 mm	2 mm	0.16446793	0.164	0.08578489	0.0859
5–16 [34]	5.31-13.44	5.20-13.25	RO4350B (ε_2 = 3.48)	RO4350B (ε_1 = 3.48)	0.2 mm	1.52 mm	0.16446793	0.164	0.05423183	0.0543
16.5–37 [35]	17.67-46.88	17.9-47.91	Taconic TSM-DS3 (ε_2 = 3)	Taconic TSM-DS3 (ε_1 = 3)	0.25 mm	1.52 mm	0.16446793	0.164	0.06290892	0.063

4.6 Conclusion

This paper discussed for the first time the use of a scalable GP-based synthesis approach as an alternative design approach for PRGW unit cells at various stop band frequencies from 3 to 300 GHz. A GP-based synthesis approach is utilized to automatically generate a straightforward mathematical expression. This equation predicts two continuous values, a and p, using predefined input variables such as F_{Top}, F_{Low}, H_{sub}, H_{gap}, ϵ_{r1}, and ϵ_{r2}. The proposed approach shows superiority in terms of MSE and MAE value as well as computational time in comparison to the test-and-trial approach and other conventional ML-based approaches. We conducted an experimental validation by designing a waveguide for IoS and mid-band 5G applications using a generated GP mathematical equation. We observed good agreement between the predicted and simulated results. Our work enhances the PRGW unit cell design process by reducing computational time and cost, demonstrating the potential use of GP for an efficient and reliable component and subsystem design process.

CHAPTER 5

MACHINE LEARNING-AIDED DESIGN OF DEFECTED GROUND STRUCTURES FOR PRGW-BASED MIMO ANTENNAS

Mohammed Farouk Nakmouche[1], Dominic Deslandes[1], Mourad Nedil[2], Ghyslain Gagnon[1]

[1]Département de Génie Électrique, École de Technologie Supérieure,
1100 Rue Notre-Dame Ouest, Montréal, Québec, H3C 1K3, Canada

[2]Département de Génie Électrique, Université du Québec en Abitibi-Témiscamingue (UQAT),
Val-d'Or, Québec, Canada

Published in the journal
IEEE Transactions on Antennas and Propagation
July 2, 2025.

Abstract: This paper introduces a scalable machine learning (ML)-based inversed design approach of a newly shaped Defected Ground Structure (DGS) for isolation enhancement of a 2-port Multiple-Input Multiple-Output (MIMO) antenna based on Printed Ridge Gap Waveguide (PRGW) technology. The proposed approach employs an artificial neural network (ANN) to predict the dimension and position of the proposed DGS in terms of the isolation and gain. As a test case, the proposed approach is applied to a 2-port MIMO antenna design with very low antenna element separation of 0.36λ, enhanced isolation of 30 dB, an average high gain of 8 dBi, and a radiation efficiency of >85%. Following a unique data generation phase of 96 hours, the target objectives are computed in $\approx$ 1 minute with a low mean squared error (MSE) of 0.0014. This is a significant improvement compared to conventional Genetic Algorithms (GA) and Particle Swarm Optimization (PSO) available in the commercial CST EM simulator, which require repeated computations of more than 72 and 46 hours, respectively. The proposed approach proved to be an attractive choice that can be adapted to design 4×4, 16×16 as well as more element MIMO systems for Internet of Space (IoS) downlink applications.

Keywords: Machine Learning (ML), Printed Ridge Gap Waveguide (PRGW), Multiple Input Multiple Output (MIMO), Artificial Neural Network (ANN), Defected Ground Structure (DGS).

5.1 Introduction

The exponential growth of wireless communication systems, including radar, mobile communication, and satellite technology, requires high data rates, large channel capacities, and a high level of reliability (Yang, Jiao, Wu, Lu & Zhang, 2022). In the last decade, Multiple-Input Multiple-Output (MIMO) systems have emerged as a highly attractive and useful technology for applications that require large capacity, high transfer rates, and stable

performance (Yin, Chen, Chang, Li & Khamas, 2021a). Furthermore, MIMO systems can also mitigate the effects of the multipath, perform diversity gain, and maximize multiplexing efficiency (Gautam, Yadav & Rambabu, 2018).

Recently, and due to the above-mentioned advantages, MIMO technology has been introduced for satellite communication systems (Arapoglou, Liolis, Bertinelli, Panagopoulos, Cottis & Gaudenzi, 2011). In this area, MIMO systems can benefit from the use of orthogonal polarizations, multiple satellites, and multiple ground terminals (Attia, Abdalrazik, Sharawi & Kishk, 2023; Ramamurthy, 2018).

To enhance the performance of a MIMO system, high isolation between the antenna elements is required, since insufficient isolation may degrade the radiation pattern of each element, leading to low antenna performance such as gain (Attia, Kishk, Abdalla, Gaya, Hamza & Mahmoud, 2021). Thus, reducing the mutual coupling between antennas is a key consideration for an efficient MIMO system. One way to accomplish this is by increasing the separation distance between elements. However, this will lead to a physically larger MIMO antenna system.

Several RF/microwave approaches have been introduced for reducing the mutual coupling in MIMO systems while keeping a low profile, including the antenna's orientation and location adjustment. For instance, the embedding of noncontact patch elements between the MIMO antenna elements has been proposed to provide an out-of-phase canceling current without disturbing the antenna performance (Liu, Liang, Zhu, Liu, Liu & Sun, 2023; Su, Lee & Chang, 2012; Sufian, Hussain, Abbas, Lee, Park & Kim, 2022). Similarly, metamaterials with negative permittivity or permeability have also been suggested in recent works (Celik, Yarovoy & Aslan, 2023; Chen et al., 2022c) to decrease the distance between two antennas. Furthermore, frequency-selective surfaces (FSS) and electromagnetic band gap (EBG) structures were also suggested to filter out the coupling surface currents (Khan, Zhang, Ali & Wu, 2023; Yang, Liu, Xu & Gong, 2017) between MIMO antenna elements.

Defected Ground Structure (DGS) stands out among the decoupling approaches due to its straightforward implementation and low profile (B-Suwailam, Siddiqui & Ramahi, 2010). It suggests cutting different-shaped slots between antenna elements without adding any additional components. DGS has the effect of a bandgap filter for rejecting coupling waves (Nan, Xie, Gao, Song & Yang, 2021b; Qian, Chen & Kishk, 2021). However, the conventional synthesis technique of the DGS structure is based on intensive parametric studies that involve significant computational cost and energy (Deng, Zhu & Ouyang, 2023).

Numerical approaches based on conventional optimization algorithms such as Genetic Algorithm (GA) and Particle swarm optimization (PSO) can be used. However, they rely on conducting numerous simulations, searching for the targeting decoupling performance while maintaining gain stability across the operating frequency band. This exhaustive simulation process presents a considerable challenge to achieving target designs within a reasonable time frame for optimization.

Recently, the integration of Machine Learning (ML) as a tool in the design process of antennas has emerged as a new synthesis approach due to its ability to easily fit the complex nonlinear relationships between antenna dimensions and parameters such as S-parameters, gain, radiation efficiency, and directivity (An et al., 2022). In fact, ML-based methods have proven to outperform conventional numerical approaches in terms of accuracy and computing efficiency (Xiao, Shao, Jin & Wang, 2018).

Qian et al. (Qian, Huang, Chen, Abdullah, Zhao & Kishk, 2022) propose an ML-based synthesis approach to fine-tune DGS parameters with reduced design time. The optimized DGS can achieve both E- and H-plane coupling reductions. However, the proposed configuration is a simple array patch antenna with a simple H-shaped slot-based DGS geometry operating at low frequencies. Aside from the work by Qian et al., most published studies (Gao, Cao, Fu, Quan & Chen, 2020a; Liu, Zhu & Lu, 2024; Qian, Chen, Zhao, Chen & Kishk, 2023) propose DGS structures that can reduce the coupling between two antennas in either the E-plane or the H-plane, but not in both planes unless multiple DGSs are employed.

In this paper, an efficient and low-computing-time-demand ML-based inverse design approach is proposed for a newly shaped DGS. The goal is to achieve target isolation between MIMO antenna elements and target gain based on the requirements defined by the engineer. The proposed design approach is tested and validated on a 2-port MIMO antenna based on a Printed Ridge Gap Waveguide (PRGW) and operating at a Ku and X-bands suitable for Internet of Space (IoS) downlink applications. A detailed performance analysis is performed in terms of error rate, regression value (R^2), and computational time. Lastly, a comparative analysis is conducted between the proposed approach and the conventional optimization algorithm-based approach, such as GA and PSO, available in commercial EM software, in terms of computational time and accuracy. The proposed approach can be adapted to design a 4×4, 16×16, as well as more elements in MIMO systems operating at X and Ku band applications. The key technical contributions of this study are outlined below:

1- We develop a scalable, low-compute-time, ML-based inverse synthesis method that automatically generates newly shaped DGS to meet user-specified isolation and gain targets.

2- We demonstrate the method on a distinct 2-port PRGW antenna operating in Ku-and X-bands for IoS downlink.

3- The proposed approach can be adapted to design a 4×4, 16×16, as well as more elements in MIMO systems for any given operating frequency band application.

Section II presents the proposed ML-based synthesis approach, including the problem description, the inverse design methodology, the mitigation strategy for the 1-to-N problem, and the configuration of the ANN hyperparameters. Section III evaluates the performance of the proposed approach in terms of prediction accuracy, computational time, convergence dynamics, and model complexity. Section IV applies the developed method to a test case involving the design and fabrication of a 2-port PRGW-based MIMO antenna operating at the Ku-band. Section V investigates

the scalability of the proposed approach to larger MIMO configurations, while Section VI provides a comparative analysis against conventional optimization techniques. Section VII presents the discussion and future directions. Finally, Section VIII concludes the paper.

5.2 Machine Learning Synthesis Approach

This section introduces the problem description and the proposed ML-based inverse design approach in detail.

5.2.1 Problem Description

Fig. 5.1 illustrates the proposed DGS structure (in black), positioned between two slots located at the top and bottom of the DGS within an overall blue box limit. The selected geometry of the proposed DGS consists of both vertical and horizontal slots, with the objective of reducing the coupling of E- and H-plane waves between adjacent slots. Through suitable DGS dimensions and positions, it is possible to manipulate the behavior of electromagnetic waves, resulting in distinct frequency-filtering characteristics. This manipulation could subsequently lead to a reduction in isolation levels and changes in gain.

To construct an ML model, the input feature vector X is composed of two distinct features X = [Ant_{Isol}, Ant_{Gain}], which represent the isolation between the MIMO antenna elements and the gain of the MIMO antenna, respectively. The output feature vector Y is composed of six distinct features Y = [X_{DGS1}, Y_{DGS1}, X_{DGS2}, Y_{DGS2}, X_{Pos}, Y_{Pos}] that include the DGS geometrical parameters and position. Accordingly, the objective of the proposed ML-based inverse design approach is to find the most suitable dimensions and positions (X_{DGS1}, Y_{DGS1}, X_{DGS2}, Y_{DGS2}, X_{Pos}, Y_{Pos}) of the proposed DGS that achieve the target Ant_{Isol} and Ant_{Gain}.

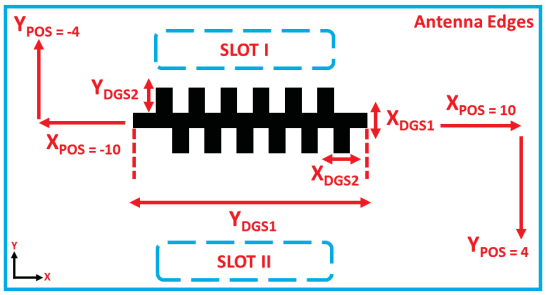

Figure 5.1 Synthesis parameters of the proposed DGS structure

5.2.2 Proposed ML-Based Synthesis Approach

In this work, we employ an inverse-modeling strategy that reverses the traditional cause-and-effect paradigm, rather than predicting antenna performance from a specified geometry (forward modeling), the model directly

determines the geometry needed to satisfy predefined performance targets (inverse modeling) (Na, Bai, Jin, Xie, Zhang & Zhang, 2025).

The proposed ML-based inverse design approach consists of the following steps, as illustrated in Fig. 5.2 and Fig. 5.3:

1. A dataset is generated by running multiple simulations using the VBA programming tools of the 3D EM analysis software with various values for the dimension and the position of the DGS.
2. Using a Matlab program based on the Scikit-Learn library, the ML model is trained, tested, and validated.
3. The trained, tested, and validated ML model is used to predict the most suitable dimension and position of the DGS in terms of target isolation and gain. It is noteworthy to highlight that the target isolation and the gain given as input are based on the requirements provided by the antenna engineer.

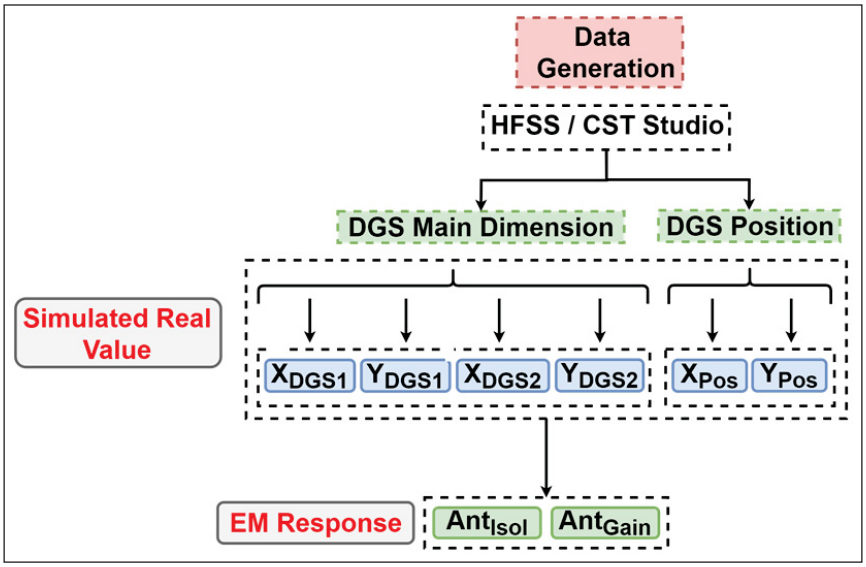

Figure 5.2 Proposed data generation process

Among the various ML techniques reported in the literature, the Artificial Neural Network (ANN) is selected because of its strong universality and suitability for mapping complex features between the antenna dimensions and performance (Zhang, Gupta & Devabhaktuni, 2003a), as well as the ease of implementation (Liu, Peng & Shao, 2022; Shalev-Shwartz & Ben-David, 2014b).

An ANN model can be created by learning from detailed (accurate) data of the RF/microwave component, resulting in a model that accurately represents the original component behaviors (Rizzoli, Costanzo, Masotti, Lipparini & Mastri, 2004; Sharma, Zhang & Xin, 2020c).

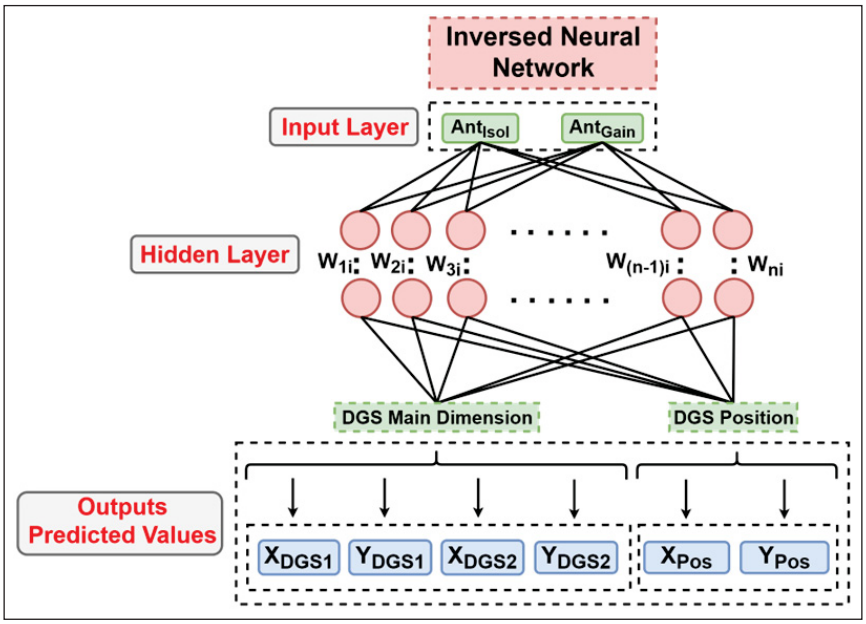

Figure 5.3 Proposed ML-based inverse design approach

Input X_i is transmitted to the hidden layers from the input layer. In the hidden layer, neuron j calculates its output by adding up its input X_i after multiplying weights W_{iJ} based on respective connections from the input layer. The neuron then processes its output Y_j using the function g of the sum, along with a bias value B_j added to it. This process is illustrated in equation 1 below (Misilmani, Naous & Khatib, 2020c):

$$Y_j = g(\sum_i W_{ij} \cdot X_j) + B_j \tag{5.1}$$

where $g(\sum_i W_{ij} \cdot X_j)$ represents the activation function such as a sigmoid, hyperbolic tangent, radial basis function, etc. We chose to use the sigmoid activation function detailed in (Marsland, 2014b). Four different numbers of hidden layers: 8, 16, 32, and 64 have been taken into consideration and investigated with three different well-known learning algorithms, namely: Levenberg-Marquardt (LM), Bayesian regularization (BR), and Scaled Conjugate Gradient Backpropagation (SCGB) (Demuth, Beale & Inc., 2001).

The procedures for the training and testing phases related to the proposed ANN model are illustrated in Fig. 5.4. During the training phase, the objective is to minimize the discrepancy between the predicted and real values (from 3D EM analysis software) by fine-tuning the internal weights of the model. Subsequently, in the testing and validation phases, the trained model is capable of simultaneously processing the (Ant_{Isol}, Ant_{Gain}) as inputs to yield corresponding outputs X_{DGS1}, Y_{DGS1}, X_{DGS2}, Y_{DGS2}, X_{Pos}, and Y_{Pos} that align with various DGS structure dimensions and position values. Once the model has been trained, tested, and validated, it will be able to predict

the dimension and position of the proposed DGS structure. This prediction is made by considering specifications related to target gain and isolation, which are given as inputs and pre-defined by the antenna engineer.

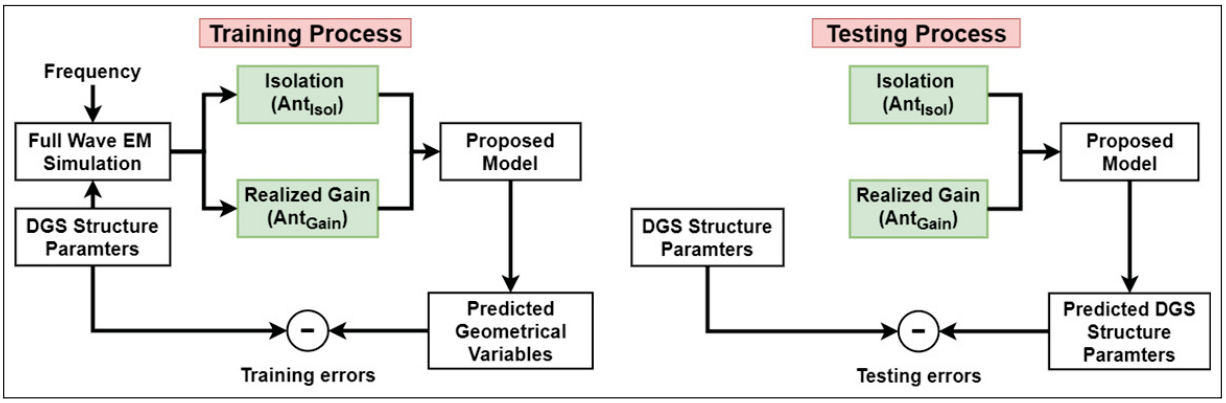

Figure 5.4 Training and testing processes of the proposed ANN model

5.2.3 Mitigation of the 1-to-N Problem

In the context of the proposed inverse EM design approach, the 1-to-N problem refers to the non-uniqueness of solutions, where multiple distinct geometrical configurations can produce similar EM performance metrics. To mitigate this ambiguity and ensure stable model convergence, the design space is deliberately constrained to technology, namely the PRGW, and a controlled range of DGS geometrical variations. By restricting the degrees of freedom to physically meaningful modifications within a constrained parameter space, a quasi-one-to-one mapping between the target specifications (isolation and gain) and the DGS design parameters is achieved.

Furthermore, to ensure that the synthesized designs satisfy the intended performance objectives, all ANN-predicted geometries are validated through full-wave EM simulations using CST Microwave Studio. This validation step serves a role comparable to surrogate-assisted optimization frameworks, guaranteeing the physical realization of the predicted designs without incurring the additional computational overhead typically associated with surrogate model training or offline optimization iterations. This strategy preserves the computational efficiency and practical deployability of the proposed method while maintaining high prediction fidelity.

5.2.4 ANN Hyperparameter Configuration and Software Environment

All experiments were implemented in MATLAB® R2023a using the Deep Learning Toolbox. Feedforward neural networks were built with the `fitnet` function, configured with two input neurons and six output neurons. We evaluated hidden-layer sizes of 8, 16, 32, and 64 neurons to assess the impact of model complexity. Networks were trained using LM (`trainlm`), BR (`trainbr`), and SCGB (`trainscg`) algorithms, employing default

performance functions (MSE for LM and SCG; MSE plus weight decay for BR). Input and output data were preprocessed with `removeconstantrows` and `mapstd`. Training proceeded for up to 1 000 epochs, with a performance goal of 1×10^{-5}, a minimum gradient of 1×10^{-7}, and early stopping after six validation failures. A fixed learning rate of 0.09 was used, and the dataset was randomly partitioned into 70 % training, 15 % validation, and 15 % testing subsets. A complete summary of these settings is provided in Table 5.1.

Table 5.1 ANN Hyperparameter Settings

Hyperparameter	**Value**
Neurons in Input Layer	2
Neurons in Output Layer	6
Neurons in Hidden Layer	8, 16, 32, 64
Training Algorithm	Levenberg–Marquardt (LM) Bayesian Regularization (BR) Scaled Conjugate Gradient (SCG)
Learning Rate	0.09
Number of Epochs	1000
Input Processing Functions	removeconstantrows, mapstd
Output Processing Functions	removeconstantrows, mapstd
Data Split (train/val/test)	70% / 15% / 15%
Performance Function	MSE (LM, SCG) MSE + weight decay (BR)

5.3 Performance of the Proposed ML-Based Inverse Design Approach

The 3D EM analysis software generates the dataset by performing a parametric study where X_{DGS1} and X_{DGS2} are chosen in terms of λ = 21.72 mm (at 13.8 GHz) to be $< \lambda/10$, Y_{DGS1} is chosen to be from 0.25λ to 2λ, Y_{DGS2} from $< \lambda/20$ to $\lambda/10$, X_{POS} around 0.5λ, and Y_{POS} around 0.25λ as shown in Table 5.2. The dataset generation process requires 72 hours to produce 1200 samples. This dataset is then divided into three subsets: 70% for training and 15% each for testing and validation. Before model fitting, the raw dataset was cleaned by excluding any samples whose feature values lay beyond three standard deviations from the mean (outlier removal) and by discarding rows containing NaN entries (missing-value handling).

It should be noted that the dataset used for training was generated considering a Ku-band operation centered around 13.8 GHz. The geometrical parameter variations were selected to meet target isolation and gain specifications within the Ku-band frequency range (12–18 GHz). Nevertheless, once trained, the model exhibits scalability and can be applied to other frequency bands without requiring retraining.

To evaluate the performance of the trained ANN model, statistical measures are employed. Specifically, the Root Mean Squared Error (RMSE), Mean absolute percentage error (MAPE), standard deviation, and the R-squared (R^2) are adopted as evaluative metrics [34]. These measures serve to evaluate how closely the predicted values of

Table 5.2 Definition of training and testing dataset

Geometrical Parameters	Training Data (mm)			Geometrical Parameters	Training Data (mm)		
	Min	Max	Step		Min	Max	Step
X_{DGS1}	0.5	2.5	0.1	Y_{DGS2}	0	3.5	0.1
Y_{DGS1}	10	35	0.5	X_{POS}	-10	10	0.5
X_{DGS2}	0.25	3.5	0.1	Y_{POS}	-4	4	0.25

Table 5.3 Comparison with other optimization algorithms in terms of RMSE, MAPE, and computational time

Algorithms	**GA**	**PSO**	**LM Model**				**BR Model**				**SCGB Model**			
			8	**16**	**32**	**64**	**8**	**16**	**32**	**64**	**8**	**16**	**32**	**64**
Average RMSE	NA	NA	0.82	1.04	0.83	1.92	0.24	**0.02**	0.68	0.13	1.30	4.47	10.10	5.80
Average MAPE (%)	NA	NA	3.36	4.17	3.72	7.66	0.82	**0.24**	2.38	0.48	5.31	11.36	22.01	42.12
Data Generation Time	NA	NA	**96 hours**											
Computational Time	74 hours	46 hours	**1 minute**				**1 minute**				**1 minute**			

the ANN model align with the actual values from the dataset. In addition, we recorded the runtime for training each network and for evaluating it on the test subset for each algorithm. Furthermore, to validate the efficiency of the proposed ML-based approach, a comparison with the GA and PSO optimization algorithm-based approaches available in commercial EM software is conducted in terms of computational time. The GA and PSO-based approaches are in the same order as the generation of all datasets for ML.

To give a thorough assessment of the performance of the trained ANN model, we structure our evaluation into four focused analyses covering predictive accuracy, computational efficiency, convergence dynamics, and model complexity.

5.3.1 Performance Metric Analysis

From Table , we can clearly see that the BR algorithm delivers the best accuracy, achieving a minimum RMSE of 0.02 and MAPE of 0.24% at 16 neurons. Its R^2 values exceed 0.99 for training, validation, and testing with 16 neurons, as Fig. 5 illustrates. The LM model performs competitively at smaller scales (for example, RMSE = 0.82, MAPE = 3.36%, R^2 = 0.88 with 8 neurons), whereas the SCGB model yields the highest error metrics (for example, RMSE = 1.30, MAPE = 5.31%, R^2 = 0.79 with 8 neurons), which indicates reduced reliability for inverse synthesis in this context.

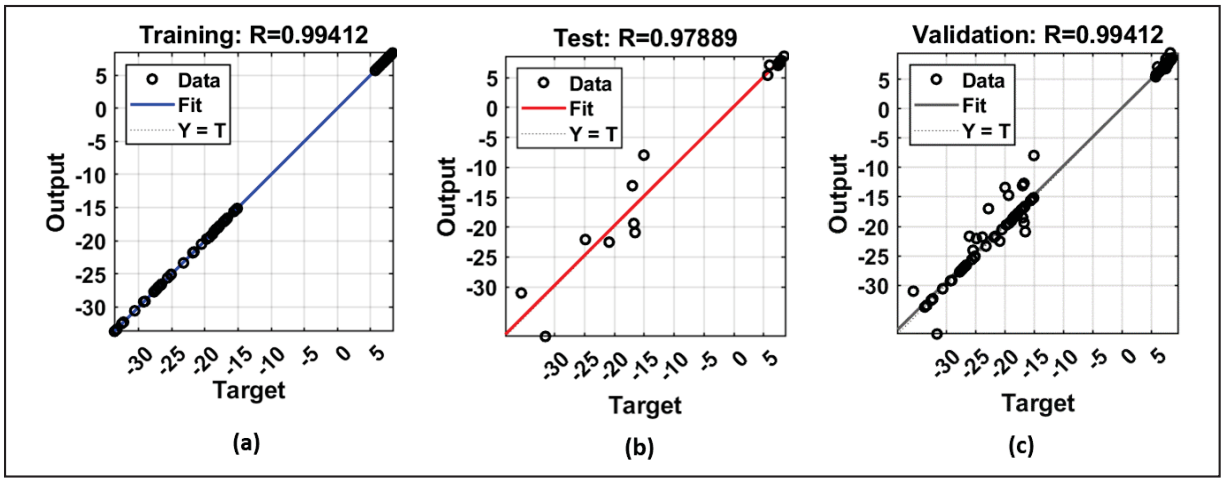

Figure 5.5 Regression value (R^2): (a) Training R^2 value, (b) Testing R^2 value, (c) Validation R^2 value

5.3.2 Computational time Analysis

Including the standard deviation allows us to quantify each model's consistency: the BR algorithm achieves its lowest standard deviation of 0.78 at 16 neurons, while the LM and SCGB models exhibit larger variability (up to 1.87 and 2.76, respectively). These results show that BR not only produces the most accurate predictions but also maintains the greatest stability across repeated trials.

In terms of training and testing time, the LM algorithm converges in under one second across all network sizes. Specifically, it trains in 0.62 s at 8 neurons, 0.48 s at 16, and roughly 0.55–0.58 s at 32 and 64, with testing latencies of 4–12 ms. In contrast, BR incurs longer training times 0.82 s at 8 neurons, 3.5 s at 16, and up to 9.8 s and 40.3 s at 32 and 64 because it integrates hyperparameter re-estimation and regularization via approximate Hessian inversions, whose cost scales superlinearly with network size. That extra computation, however, yields superior predictive performance (e.g., at 16 neurons BR achieves an RMSE of 0.02 and $R^2 > 0.99$). Finally, SSCGB is the lightest overall, training in 0.56–0.66 s and testing in 3–5 ms. However, it incurs the largest errors among the three methods. We also compared the computational time of GA and PSO in CST Studio with that of our ML-based method for the following objectives:

1. Edge to Edge Distance of $0.36\lambda_0$
2. Isolation (Ant_{Isol}) 30 dB in the frequency ranges of 12.75-13.5 GHz
3. Maximum gain (Ant_{Gain}) > 8 dB at 12.75-13.5 GHz

Table III demonstrates the scalability of the ANN model by predicting the target solution for any frequency band in less than 1 minute. In comparison, GA and PSO took over 74 hours and 46 hours of continuous iterations

to solve the synthesis problem, a process that must be repeated for each new frequency band. The reduction in computing time provided by the ANN model is a significant improvement over the classical design techniques aided by heuristic optimization algorithms, which require an intensive and expensive synthesis process.

It is worth mentioning that the dataset generation process required a one-time 96-hour full-wave simulation, a computational cost comparable to that of the repeated and constant requirements in conventional approaches.

All the computations are conducted using a Windows 64-bit Lenovo ThinkStation P320 tower workstation with a 12th Generation Intel® Core™ i7-12700K Processor with vPro® (E-Core Max 3.80 GHz, P-Core Max 4.90 GHz with Turbo Boost, 12 Cores, 20 Threads, 25 MB Cache), 32 GB of RAM, and NVIDIA® T1000 4GB.

5.3.3 Convergence Dynamics

To conclude, Fig. 5.6 presents the evolution of training and testing mean-square error over epochs for the proposed ML-based inverse design approach, illustrating its rapid convergence and strong generalization. As shown in Fig. 5.6, the learning curve plotting training and testing MSE versus epoch can be divided into three phases. During the first three epochs, both curves decline steeply (training MSE from ≈ 260 to ≈ 20; testing MSE from ≈ 50 to ≈ 40), indicating rapid acquisition of the underlying mapping. Between epochs 4 and 10 the rate of decrease slows and both curves gradually approach their minima (training MSE ≈ 2˜3; testing MSE ≈ 4˜5), signifying convergence. Beyond epoch 10, the errors remain essentially constant, demonstrating stable performance. The small, consistent gap between the two curves and the absence of any widening confirms strong generalization and lack of overfitting.

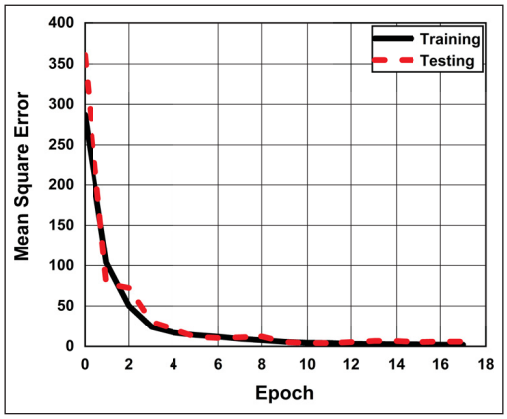

Figure 5.6 Learning curve: training and testing MSE versus epoch

5.3.4 Complexity Analysis

Table III confirms that the proposed ANN outperforms the 46–74 h iterative optimization cycles of PSO and GA with a one-time 96 h data-generation step and a prediction latency below 60 s for any new target specification, representing $10^3\times$ a magnitude speed-up.

Among the training algorithms investigated, BR applied to a 16-neuron network delivers the best accuracy-cost trade-off: RMSE = 0.02, MAPE = 0.24%, and R^2 = 0.999, with only 3.5 s of training time and a 5 ms test latency.

The learning curves in Fig. 6 converged by epoch 10, maintaining a narrow and consistent train–test gap. This indicates stable generalization and confirms the absence of overfitting, crucial for the network's reliable real-time performance.

Consequently, the 16-neuron BR configuration offers the best possible trade-off between accuracy and computation time, enabling real-time synthesis without the iterative burden imposed by heuristic optimisers.

5.4 Test and Validation Case

The PRGW technology used in this work, as reported in various works in the literature (Al-Alem, Sifat, Antar & Kishk, 2023a; Liu, Yue, Jia, Xu & Xue, 2021), is suitable for high-frequency applications due to its low dissipation. The utilized PRGW unit cell, along with the dispersion diagram, are illustrated in Fig. 5.7. As can be seen in Fig. 5.7(a), the PRGW demonstrates the capability to support quasi-TEM mode propagation along the ridge from 10 to 17 GHz. Based on the proposed PRGW unit cell illustrated in Fig. 5.7(b), a 2-port MIMO antenna is designed with 2 slots, as shown in Fig. 5.8. Our proposed DGS structure is added between the slots to enhance isolation.

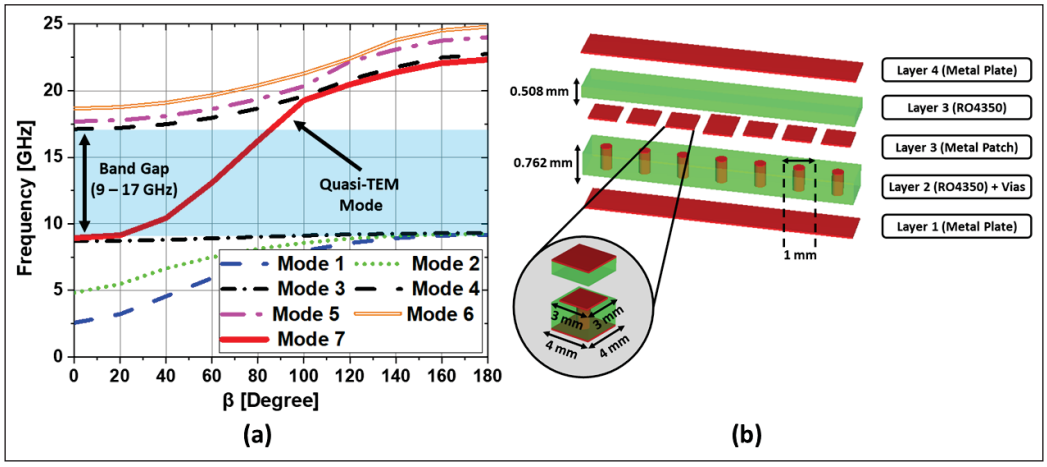

Figure 5.7 The used PRGW structure (a) Dispersion diagram (b) Proposed unit cell

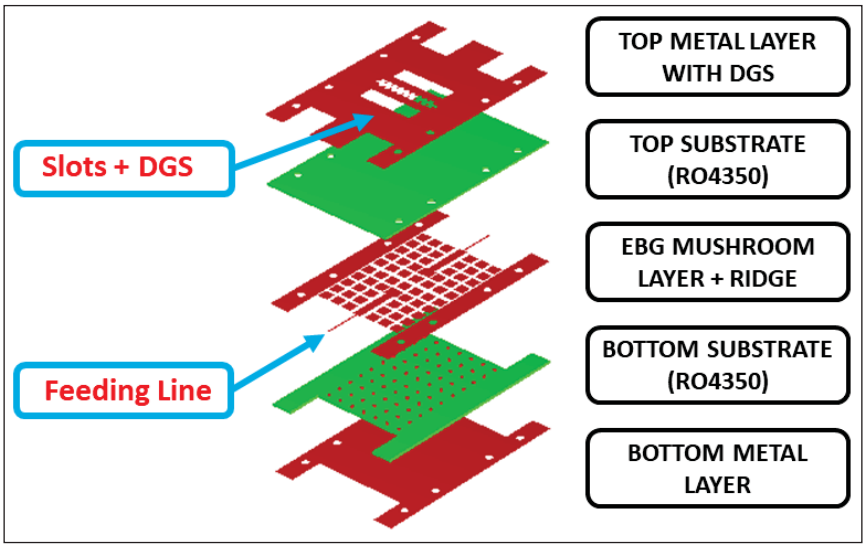

Figure 5.8 The proposed 2-port PRGW-based MIMO antenna

5.4.1 2-Port PRGW Based MIMO Antenna Without DGS

Prior to employing the trained ANN model through the integration of the newly proposed DGS structure between two radiation slots, we explore the mutual coupling effects in a 2-port PRGW-based MIMO antenna configuration without DGS structure. We chose distances between adjacent slots (edge to edge) that measure 8 mm, equivalent to 0.36λ at 13.8 GHz, as illustrated in Fig. 5.9.

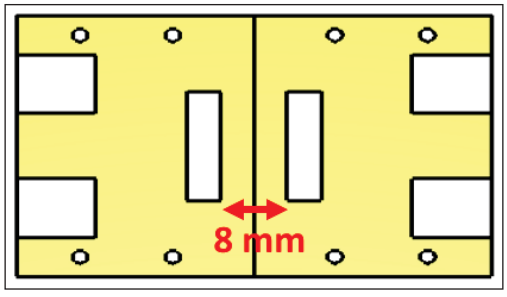

Figure 5.9 Proposed 2-Port MIMO antenna without DGS

Fig. 5.10 depicts the simulated and measured S-parameters related to the configuration without DGS structure. As expected and due to the distance between the radiating slots, a high mutual coupling of > -20 dB over the full-frequency spectrum is noticed. A high mutual coupling is occurring, characterized by high surface currents resulting from the lack of a physical or solid substrate supporting the two radiating slots. Consequently, near-field propagation between the adjacent slots and the PRGW top metallic plate is considered for the observed mutual coupling.

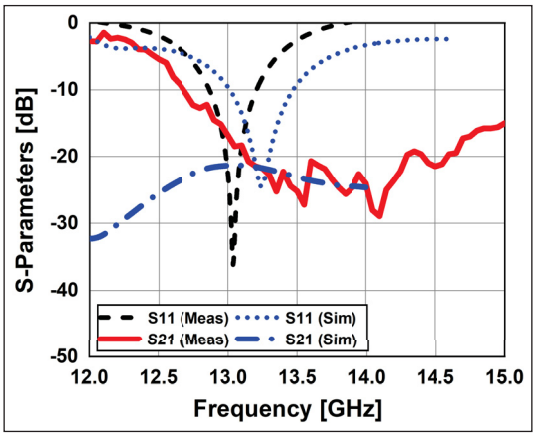

Figure 5.10 Simulated and measured results of S-parameters of the proposed 2-port MIMO antenna structure without DGS

Now, in order to systematically evaluate and validate the proposed ML-based inverse design approach, we have chosen to employ this configuration with the proposed DGS structure as a test case study with the same objectives used before with GA and PSO to maintain consistency.

5.4.2 2-Port PRGW Based MIMO Antenna With DGS

To decrease the mutual coupling, the newly proposed DGS structure is embedded between adjacent slots to minimize the surface current on the top metallic surface of PRGW, as shown in Fig. 5.11. Thus, the effect of various values of X_{DGS1}, Y_{DGS1}, X_{DGS2}, and Y_{DGS1} of the proposed DGS structure is investigated on the isolation (Ant_{Isol}) and realized gain (Ant_{Gain}) of the proposed MIMO antenna.

Observing Table 5.4, it is evident that changes in the parameters X_{DGS1}, Y_{DGS1}, X_{DGS2}, and Y_{DGS2} significantly influence the transmission coefficient. Regarding antenna gain, varying the values of X_{DGS1} and Y_{DGS1} results in slight variations in gain, while the variations in X_{DGS2} and Y_{DGS2} have negligible impact. Nevertheless, as shown in Fig. 5.12, the variations in all proposed DGS dimensions simultaneously affect both isolation and realized gain. Consequently, such adjustments facilitate improvements in isolation and realized gain. The three plotted cases in Fig. 5.12 are defined as follows:

- Case 1: X_{DGS1} = 20mm, Y_{DGS1} = 0.75mm, X_{DGS2} = 0.5mm, Y_{DGS2} = 1mm
- Case 2:X_{DGS1} = 15mm, Y_{DGS1} = 0.75mm, X_{DGS2} = 1mm, Y_{DGS2} = 0.5mm
- Case 3:X_{DGS1} = 35mm, Y_{DGS1} = 1.75mm, X_{DGS2} = 0.25mm, Y_{DGS2} = 1mm

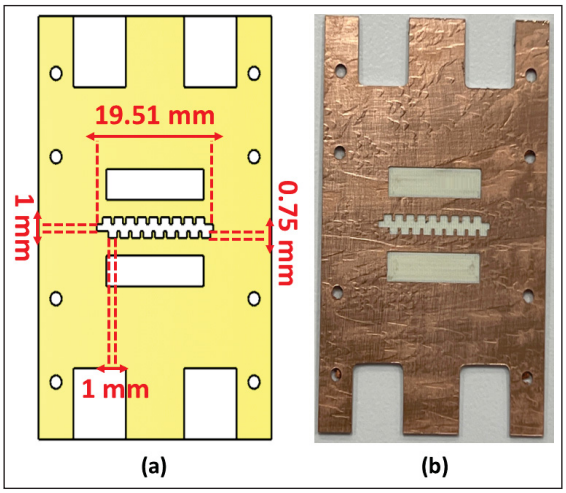

Figure 5.11 Proposed 2-Port MIMO antenna with proposed DGS (a) 3D model with physical dimensions (b) Fabricated prototype

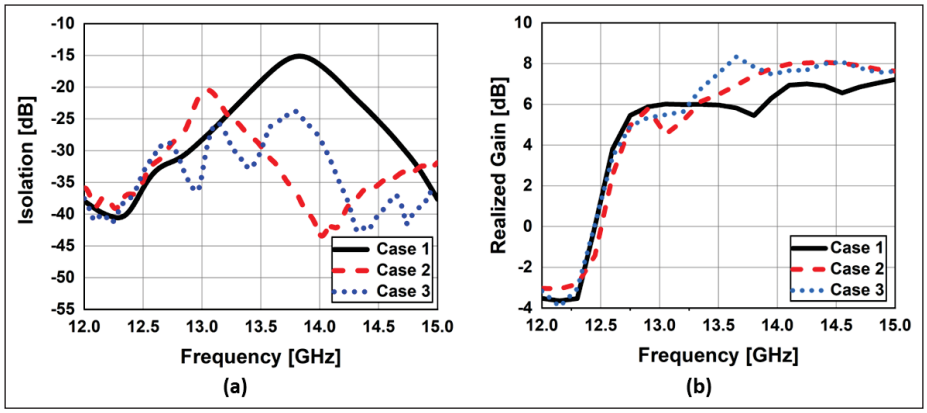

Figure 5.12 The effect of the variation of the proposed DGS structure on both isolation gain

For the previously defined target objectives and utilizing the trained ANN model, the predicted optimal values for X_{DGS1}, Y_{DGS1}, X_{DGS2}, Y_{DGS1}, X_{POS}, and Y_{POS} are 1 mm, 19.51 mm, 1 mm, 0.75 mm, 0, and 0, respectively.

The simulation using the predicted values from the proposed approach and heuristic algorithms-aided design approaches (GA and PSO), along with the measured results, can be seen in Fig. 5.13(a). As it can be seen, the proposed ML-based inversed design approach performs better in achieving the same design objectives. Besides, the predicted optimal DGS parameters achieve a gain enhancement of 2 dB (8 dBi compared to 6 dBi) over the configuration without a DGS structure, as shown in Fig. 5.13(b), along with a radiation efficiency of >85% across the operating frequency band.

Table 5.4 Summary of the parametric study

Parametric study cases	Variation of X_DGS1 values	Variation of Y_DGS1 values	Variation of X_DGS2 values	Variation of Y_DGS2 values
Isolation (S21/S12)	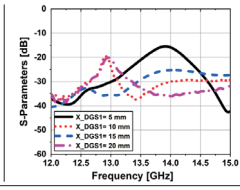	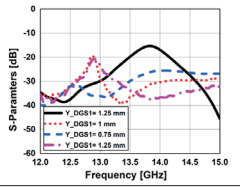	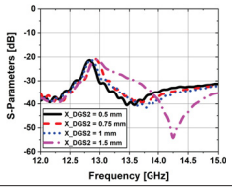	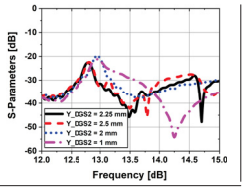
Realized gain	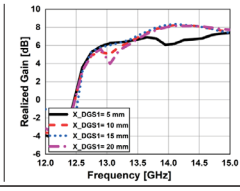	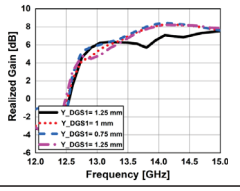	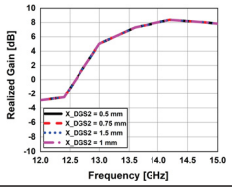	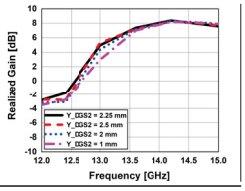

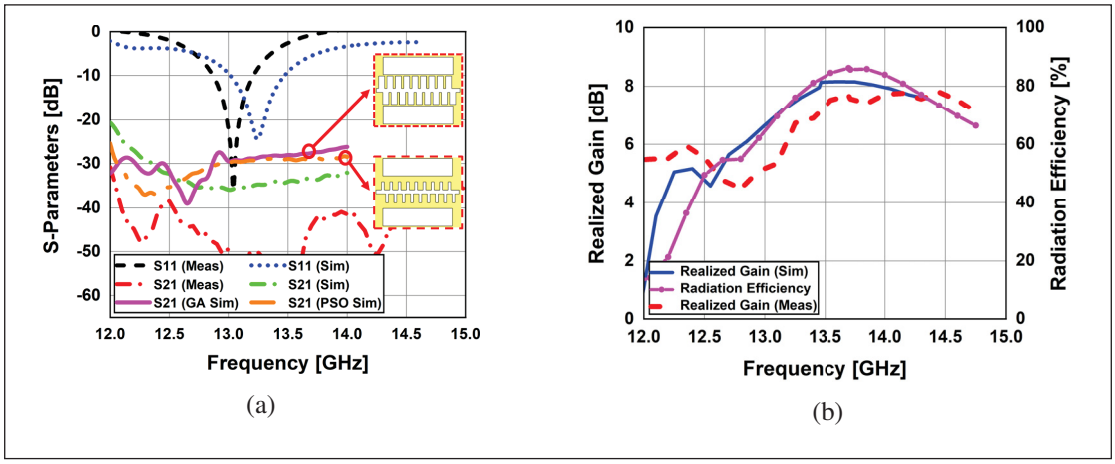

Figure 5.13 (a) Simulated and measured S-parameters with predicted dimensions from ML, GA, and PSO; (b) Realized gain [dBi] and radiation efficiency [%] with optimal DGS dimensions from ML

Fig. 5.14 illustrates the simulated current density distribution (from a 3D EM simulator) with and without DGS to evaluate the MIMO design concept of the added DGS structure to increase the isolation and keep a low distance between elements. As can be noticed from Fig. 5.14, adding the DGS structure suppresses surface current at the neighboring radiating slot. The measured radiation characteristics of the proposed 2-port PRGW-based MIMO antenna at 13.5 GHz with DGS structure in the H-plane and E-plane, respectively, are shown in Fig. 5.15. A slight discrepancy between the simulated and measured radiation patterns is observed, mainly due to the addition of connectors required for measurement, along with imperfect contact and alignment of the metallic plates.

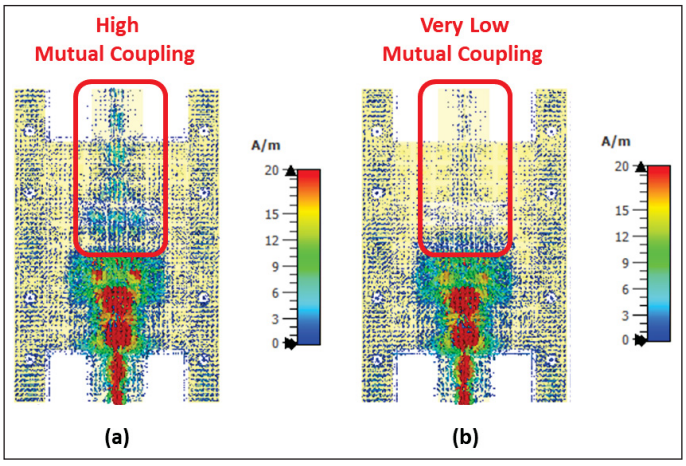

Figure 5.14 Surface current distribution (a) With DGS (b) Without DGS

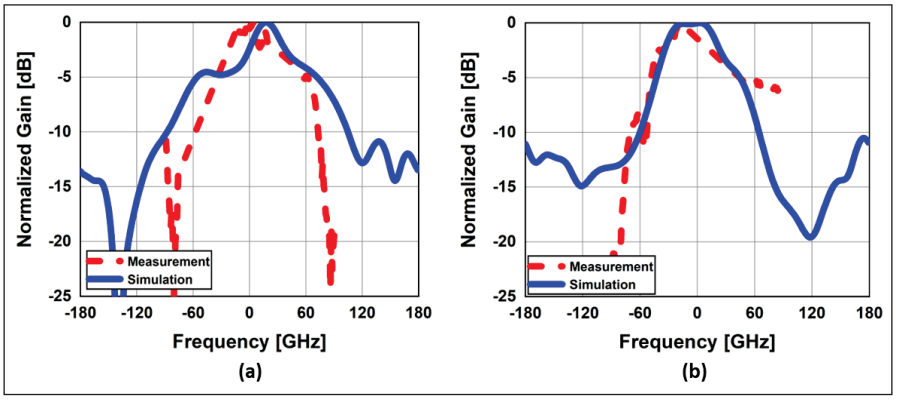

Figure 5.15 Simulated and measured radiation patterns (a) H-Plane (b) E-Plane

5.5 Scalability Investigation

In this section, we demonstrate the scalability of our proposed approach by using the trained ML model to efficiently design another highly isolated 2-port PRGW-based slot antenna for X band applications with the following target objectives:

1. Edge to Edge Distance of $0.25\lambda_0$.
2. Isolation (Ant_{Isol}) 20 dB in 8-9 GHz frequency band.
3. Maximum gain (Ant_{Gain}) > 7 dB at 8-10 GHz.

It should be mentioned that a new PRGW unit cell, shown in Fig. 5.16, is used for the target frequency band. The stop band ranges from 8 to 9 GHz, making it suitable for our targeted applications.

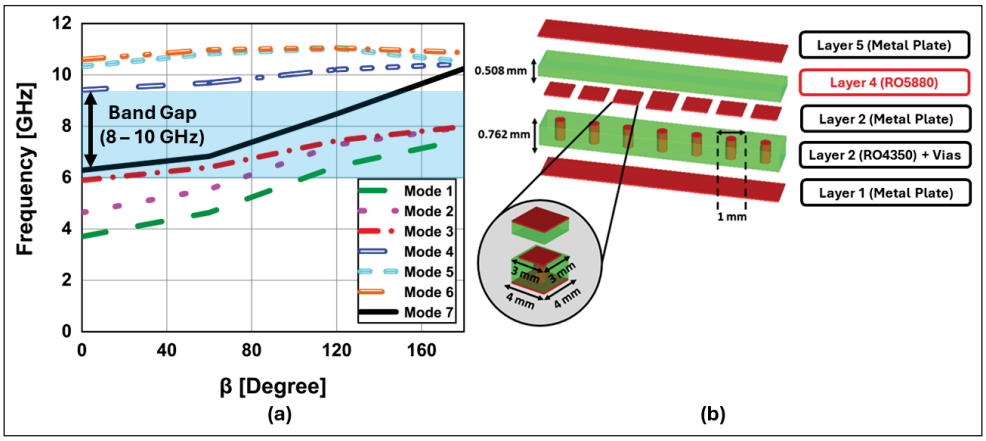

Figure 5.16 The used PRGW unit cell for X-band application : (a) dispersion diagram ; (b) structure of the unit cell

Fig. 5.17 illustrates the 3D model and the fabricated prototype of the designed 2-port PRGW-based MIMO antenna intended for X-band applications. This design includes DGS structures designed using the trained ANN model. The predicted dimensions for the DGS structures are as follows: X_{DGS1} = 2.26 mm, Y_{DGS1} = 25.32 mm, X_{DGS2} = 0.88 mm, Y_{DGS2} = 2.11 mm. The S-parameter results for the simulation and measurement using the predicted DGS dimension can be seen in Fig. 5.18(a). As illustrated, the proposed ML-based inverse design approach effectively meets the target design objectives with an isolation of 20 dB and an edge-to-edge distance between the slots of $0.229\lambda_0$. The DGS structure, as predicted by the trained ANN model, achieved a peak realized gain of 7.7 dBi at the resonance frequency band, as depicted in Fig. 5.18(b). The same figure also shows that the radiation efficiency is >80% throughout the operating frequency band.

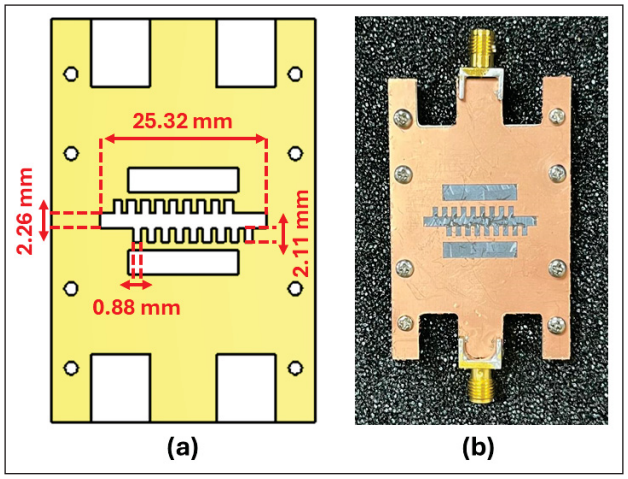

Figure 5.17 Proposed 2-port MIMO antenna for X-band application : (a) 3D model ; (b) fabricated prototype

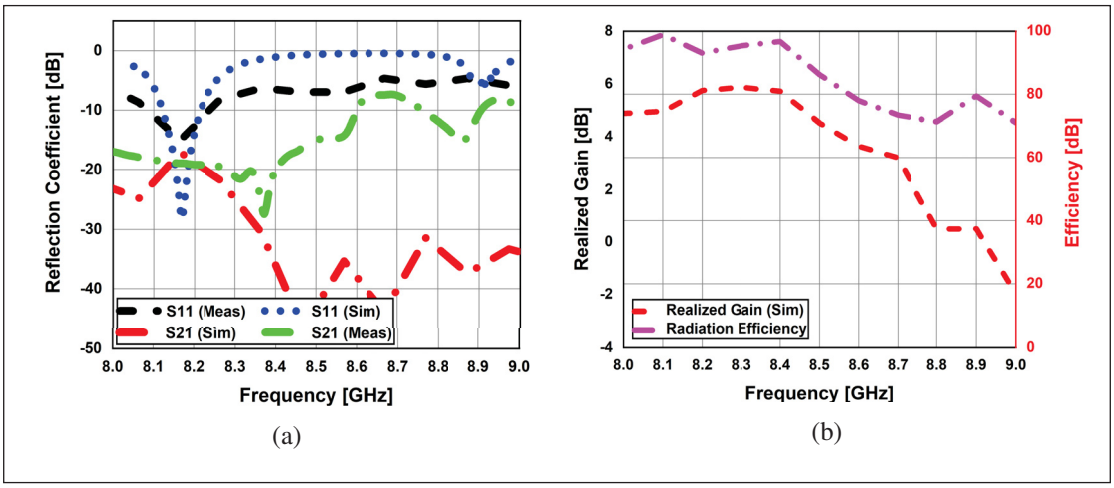

Figure 5.18 (a) Simulated and measured S-parameters (b) Realized gain [dBi] and radiation efficiency [%]

5.6 Discussion and Future Directions

The proposed ML-based inverse design achieves a compact 2-port PRGW MIMO antenna with enhanced isolation and realized gain. Benchmarks against other Ku-band MIMO designs Table 5.5) confirm its superiority. Although trained on a single-band Ku-band dataset, the framework is scalable to other bands (e.g., C-, Ka-band, mmWave) but not yet to dual- or ultra-wideband target design cases.

Integrating dual-band and ultra-wideband objectives into the ANN's training pipeline enables the synthesis of antenna designs for multi-standard and wide-coverage applications, such as satellite downlinks, 5G/6G base stations, and broadband IoT networks. Inspired by the k-means clustering-based ANN approach reported in (Cai, Chen, Qi et al., 2025), we propose to implement a hierarchical, cluster-aware architecture that partitions the frequency-response dataset into K clusters using k-means. Although applied in a different domain, the clustering methodology demonstrated in (Cai *et al.*, 2025) can transferable and provides a suitable framework for tailoring ANNs to specific frequency bands in antenna synthesis. For each cluster, we train a dedicated ANN to map performance targets to geometry parameters. During inference, a k-nearest-neighbor classifier will assign new targets to their nearest cluster centroid and route them to the corresponding ANN. This strategy enables interpolation and extrapolation across clusters, supporting dual-band and wideband synthesis.

Temporal attention mechanisms in prior work (Cai, Li, Liu, Wu, Zhu, Chen, Lei, Hou, Guo, Jiang, Guo, Wang, Huang, Zhu, Fan & Tao, 2024) have demonstrated enhanced sequence modeling by prioritizing informative time steps, particularly in biomedical time series. In (Cai *et al.*, 2024), the authors introduced a late-temporal attention module within an LSTM framework to improve robustness against noise and temporal shifts. Although originally developed for biomedical signals, the underlying principle of dynamic feature prioritization is directly applicable

to our future multi-band and wideband antenna synthesis. Specifically, this late-temporal attention can guide the model to focus on critical frequency regions without substantially increasing network complexity.

In future study, we will leverage these directions, k-means clustering for hierarchical ANN specialization, and later-temporal attention for frequency-segment prioritization to extend our scalable ML-based inverse design of the newly shaped DGS to dual-band and ultra-wideband MIMO antenna synthesis.

5.7 Comparative Analysis

Finally, to conclude the paper, the 2-port MIMO antenna system chosen as the test case is compared to other works on Ku-band MIMO systems reported in the literature (see Table 5.5). Several comparative metrics are considered, including the edge-to-edge distance, isolation, and the synthesis/decoupling method. Even though their edge-to-edge distance is shorter, our proposed MIMO antenna design outperforms works reported in (Alibakhshikenari, Khalily, Virdee, See, Abd-Alhameed & Limiti, 2019; Attia *et al.*, 2021; Huang, Yang & Wang, 2023) in terms of isolation and gain. Moreover, compared to (Amillia, Setijadi & Hendrantoro, 2022; Gao, Cao, Fu, Quan & Chen, 2020b; Zhang, Deng, Li, Sun & Guo, 2019b), it is shown that our proposed design is more compact and presents higher performance in terms of isolation and gain. It is essential to emphasize that the proposed design's simplicity makes it applicable to the design of vast MIMO systems with more radiating elements (4×4, 16×16) that can be used for IoS applications in the X and Ku frequency bands.

Table 5.5 Comparison with other reported works in literature

Ref.	Gain (dB)	Edge-to-Edge Distance (λ_0)	Isolation (dB)	Optimization/Decoupling Methods
[7]	10	0.28	17	DGS + Test & Trial
[37]	6	0.20	18	Pixel DGS + K-means
[38]	6.5	0.65	17	EBG Fractal + Test & Trial
[39]	5.43	0.76	20	Parasitic Patches + Test & Trial
[40]	NA	0.40	24	Metal Strip + Test & Trial
[41]	NA	0.50	31	Barbell Array DGS + Test & Trial
Our Work (Ku-Band)	8.0	0.36	40	DGS + ANN
Our Work (X-Band)	7.7	0.229	25	DGS + ANN

5.8 Conclusion

This paper presents a scalable ML-based inverse design approach for a newly shaped DGS to enhance the isolation between the PRGW-based MIMO antenna elements for IoS downlink applications. The proposed method employs ANN to predict the dimensions of the proposed DGS as output, considering key antenna characteristics like edge-to-edge distance, isolation, and realized gain as input defined by the engineer. The results demonstrate the

effectiveness of this approach in designing a compact 2-port MIMO antenna for Ku and X band applications with two predefined target objectives set.

Comparative analysis with the conventional optimization techniques (GA and PSO) available in the commercial 3D EM simulator validates the superiority of the proposed ML approach, achieving a low MSE = 0.0014 with reduced computational time (≈1 minute). Unlike GA and PSO, which require repeated and constant computations of more than 72 and 46 hours, respectively, our proposed approach requires only a 96-hour data generation phase.

Experimental validation further confirms the agreement between measured and predicted/simulated results over the operating frequency band. This research shows how ML could be used to synthesize DGS structures in a way that is reliable and saves both computational time and energy. In future studies, it is possible to make improvements to the dataset in order to cover other frequency bands.

CHAPTER 6

LOW-COST ORIGAMI PRINTED RGW WIDEBAND MIMO ANTENNA WITH ADDITIVELY MANUFACTURED DIELECTRIC RESONATOR

Mohammed Farouk Nakmouche[1], Dominic Deslandes[1], Mourad Nedil[2], Ghyslain Gagnon[1]

[1]Département de Génie Électrique, École de Technologie Supérieure,
1100 Rue Notre-Dame Ouest, Montréal, Québec, H3C 1K3, Canada

[2]Département de Génie Électrique, Université du Québec en Abitibi-Témiscamingue (UQAT),
Val-d'Or, Québec, Canada

Submitted to the journal
IEEE Transactions on Components, Packaging and Manufacturing Technology
June 11, 2025.

Abstract: This work introduces, for the first time, a wideband, low-cost, foldable Printed Ridge Gap Waveguide (PRGW) origami antenna with an additively manufactured dielectric resonator (DR) for multi-input multi-output (MIMO) applications, operating from 12 to 15 GHz. The mechanical foldability is achieved using a conventional surrogate hinge architecture, allowing the antenna to fold nearly 360° without mechanical or electromagnetic (EM) failure, thus enabling beam reconfigurability. Using a multi-permittivity DR based on low-cost polylactic acid (PLA) materials with ϵ_{r1} = 2.72 (100% infill) and ϵ_{r2} = 1.24 (18% infill), the TE11, TE21, and hybrid mode B are excited, and thus wideband impedance bandwidth is achieved. The proposed compact MIMO antenna achieves high isolation of 40 dB, with a gain of 7.5 dBi at 13.5 GHz and a radiation efficiency of 85%. Experimental validation confirms that the measured results align well with the simulated results over the operating frequency band.

Keywords: Origami, Foldable, 3D Printing, Printed Ridge Gap Waveguide (PRGW), MIMO Technology, and Dielectric Resonator Antenna (DRA), Additive Manufacturing.

6.1 Introduction

Dielectric resonator antennas (DRAs) are an attractive choice due to their numerous advantages over conventional radiating elements. Their high radiation efficiency, attributed to the absence of conductor-related surface wave losses, makes them a compelling alternative. Additionally, DRAs offer ease of excitation, a nearly constant gain, wide impedance bandwidth, and compact size when designed appropriately (Li, Chen, Li, Lin & Yin, 2020; Petosa, 2007; Petosa & Ittipiboon, 2010). One effective approach to achieving a broad impedance bandwidth is through multi-permittivity Dielectric Resonators (DRs) (Chaudhary, Srivastava & Biswas, 2015; Pan & Zheng, 2016). In this context, 3D printing has emerged as a promising fabrication method for multi-permittivity DRAs, offering

rapid prototyping with reduced material waste compared to traditional techniques (et al., 2018; Hehenberger, Caizzone & Yarovoy, 2023; Huang, Chen, Xue, Withayachumnankul & Fumeaux, 2018a). Several studies (Diaz, Diaz, Rajo-Iglesias & Pizarro, 2024; Huang, Chen, Xue, Withayachumnankul & Fumeaux, 2018b; Xia, Leung & Lu, 2019; Xia, Leung, Gu & Chen, 2022) have explored 3D-printed multi-permittivity DRAs, demonstrating their potential for various applications. For instance, (Diaz *et al.*, 2024) presents a high-gain multi-permittivity DRA with an endfire symmetrical radiation pattern for sub-6 GHz applications, while (Huang *et al.*, 2018b) focuses on wideband, end-fire performance. Additionally, (Xia *et al.*, 2019) introduces a 3D-printed multi-ring DRA for wideband operation, and (Xia *et al.*, 2022) proposes a dual-frequency DRA with two ports for S- and X-band vehicular communications. Despite these advancements, most reported designs rely on expensive, high-permittivity materials such as ceramics, which are both costly and challenging to process, thereby limiting their practical adoption. To address these limitations, we investigate the feasibility of low-cost multi-permittivity polylactic acid (PLA)-based filaments for additive manufacturing, offering a cost-effective and scalable alternative to conventional high-permittivity material-based DRAs that are widely accessible and compatible with standard low-cost 3D printing machines.

Furthermore, conventional feeding techniques, such as microstrip line (MSL) and substrate-integrated waveguide (SIW)-coupled slot antennas, suffer from high losses (Ali, Shams & Sebak, 2019; Kim & Rahmat-Samii, 2015). To overcome these challenges, we propose the use of printed ridge gap waveguide (PRGW) technology, initially introduced by Kildal et al. (Kildal, 1990). PRGW enables controlled electromagnetic (EM) wave propagation between metal plates, minimizing radiation losses and improving overall efficiency.

As communication technology advances, particularly with the rise of LEO satellite constellations, there is an increasing demand for expanded spectrum allocation, greater channel capacity, and robust multi-path interference mitigation (Chen, Row & Wong, 2007; Gallo, Antonino-Daviu, Ferrando-Bataller, Bozzetti, Molina-Garcia-Pardo & Juan-Llacer, 2012; Ourir, Rachedi, Phan-Huy, Leray & de Rosny, 2017). Multi-Input Multi-Output (MIMO) technology has emerged as a key solution, leveraging multiple antennas to enhance spectral efficiency and signal reliability (Boas, Ribeiro, de Figueiredo & Mejía-Salazar, 2024; Chen, Ke, Yang & Yang, 2022b). However, conventional MIMO systems often rely on fixed beam configurations, limiting adaptability in dynamic environments. While beamforming networks, whether passive or active, offer reconfigurability, they introduce additional complexity, increased insertion loss, and higher implementation costs (Liu, Wu, Zhuang, Wang & Liu, 2018; Zheng, Vandenbosch & Yan, 2020).

As an alternative solution, origami-based structures provide a promising approach, offering reconfigurability, compactness, and multifunctionality. Previous works have explored origami-inspired designs for antenna applications, such as the Kirigami-based flexible MIMO antenna in (Kiani, Marey, Rafique, Shah, Bashir, Mostafa, Wong & Parchin, 2022) for Sub-6 GHz operation and the thick origami-based reconfigurable patch array in

(Hamza, Zekios & Georgakopoulos, 2020) for beam steering at 2.45 GHz. While these studies successfully leverage origami-inspired concepts for reconfigurability, their designs remain limited in operating frequency and electromagnetic performance. Drawing inspiration from [24], the proposed design integrates origami principles with Printed Ridge Gap Waveguide (PRGW), which inherently offers lower losses and higher efficiency at high frequencies (12–15 GHz) compared to the microstrip line (MSL) used in [24]. Additionally, the incorporation of a multi-permittivity dielectric resonator enhances bandwidth, overcoming the narrowband limitations found in [23, 24]. These advancements position the proposed design as a high-performance solution for dynamic wireless environments, further distinguishing it from prior implementations.

In this communication, we present an origami foldable, low-cost, and lightweight 8-port 3D-printed DRA MIMO antenna based on PRGW technology with wideband and high-performance characteristics. The key contributions of this work are summarized as follows:

1. For the first time, a low-cost, mechanically foldable, and packable PRGW-based MIMO antenna is proposed. This configuration enables transformation from a planar to a non-planar state, achieving beam reconfigurability.
2. This work characterizes and integrates 3D-printed PLA-based DRs as a low-cost alternative to conventional high-permittivity materials, despite PLA's largely unexplored dielectric properties at high frequencies.
3. A wideband impedance bandwidth is achieved by exciting different modes using low-cost PLA material with two different infill ratios.

This paper is organized as follows: Section 2 details the configuration of the 4-port 3D-printed DRA MIMO antenna, the characterization of the PLA material, and an analysis of the modes in multi-permittivity DR. Section 3 explains the mechanism for pattern diversity in the proposed 8-port origami foldable MIMO antenna. Section 4 presents both the simulated and measured results. Section 5 offers a comparison with similar works. Finally, Section 6 concludes the paper.

6.2 Proposed Antenna Configuration

6.2.1 PLA Material Characterization

To achieve accurate design and simulation of multi-permittivity and lightweight PLA-based 3D-printed DRA structures, it is imperative to quantify the impact of different infill densities on relative permittivity and weight. In pursuit of this objective, different PLA-based samples were 3D printed based on the rectilinear pattern. These samples were created with varying infill density: 10%, 18%, 33%, 40%, 50%, 60%, 70%, 80%, and 100%. The dielectric characteristics of these PLA samples, with regard to changing infill density, were measured using the

WR-90 standard waveguide-based technique and the Nicolson-Ross and Weir (NRW) method described in (Weir, 1974).

The measurement results of permittivity and weight are presented in Fig. 6.1 (a) and Fig. 6.1 (b), respectively. The WR-90 standard waveguide is utilized to facilitate the transmission and reception of signals across the various PLA samples, enabling the measurement of dielectric properties. The measured results in Fig. 6.1 (a) show that the relative permittivity linearly increases with an increase in the infill density of PLA samples from 20% to 80%. The increase in infill density also has a clear impact on the weight (see Fig. 6.1(b)), which is proportional to the production cost and fabrication time. In this work, 18% and 33% infill densities were selected to create a significant disparity in effective permittivity, creating a high refractive index gradient within the multilayer DRA.

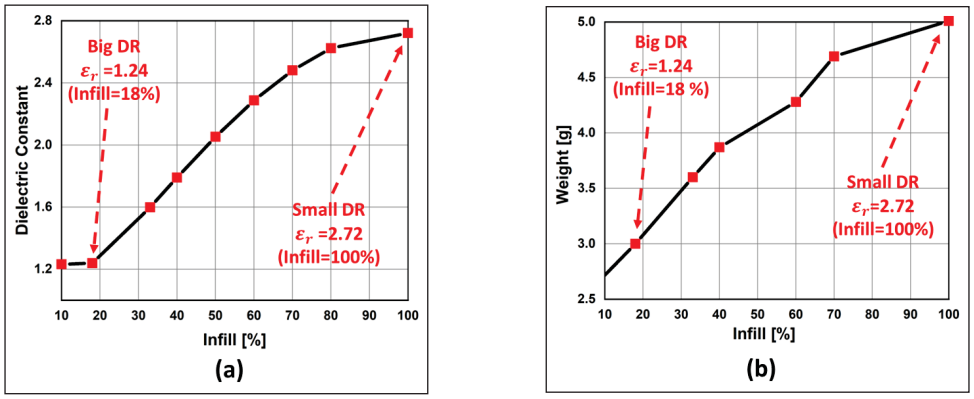

Figure 6.1 PLA material characterization (a) Dielectric constant vs infill densities (b) Weight vs infill densities

6.2.2 Feeding Antenna Configuration

Fig. 6.2 depicts the layout of the used PRGW structure. The first layer (from the bottom) consists of a simple metal plate. Whereas, the second layer consists of embedded conductor-plated vias covered by square patches, often known as a mushroom bed, which includes the printed guiding ridge and feeding line. This layer is constructed using a dielectric substrate, specifically RO4350 with a relative permittivity of ϵ_r = 3.48, and a thickness of 0.762 mm. The third layer consists of a 0.508 mm thick RO4350 dielectric layer (ϵ_r = 3.48), which is designed to support quasi-transverse electromagnetic (Q-TEM) mode propagation along the ridge within the dielectric-filled gap while minimizing dispersion. Finally, the top layer consists of a metal plate. It is worth mentioning that the proposed PRGW unit-cell configuration and associated design approach closely follow well-established approaches previously reported in the literature.

The initial design steps for the PRGW-based antenna involve evaluating the dispersion characteristics of the primary unit cell to identify the band gap, where no propagating modes exist. The band gap of a conventional unit cell

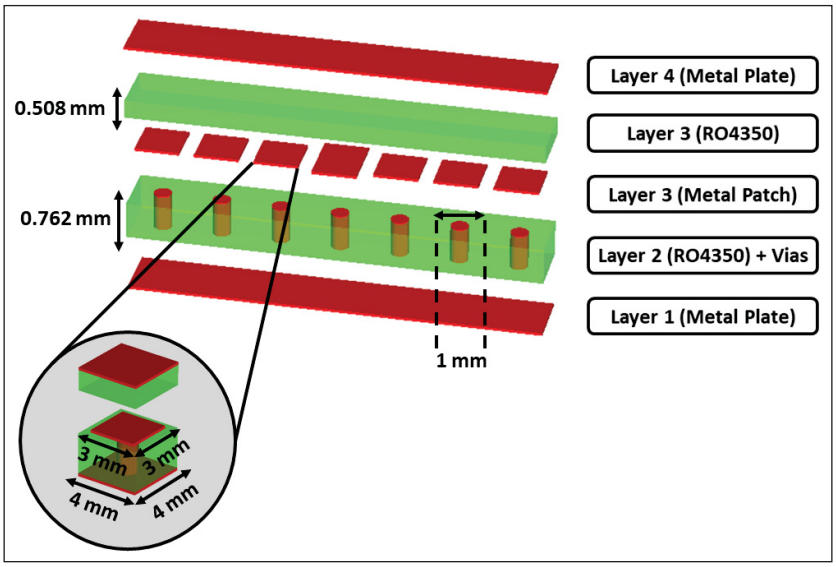

Figure 6.2 Layout of the used PRGW unit cell structure

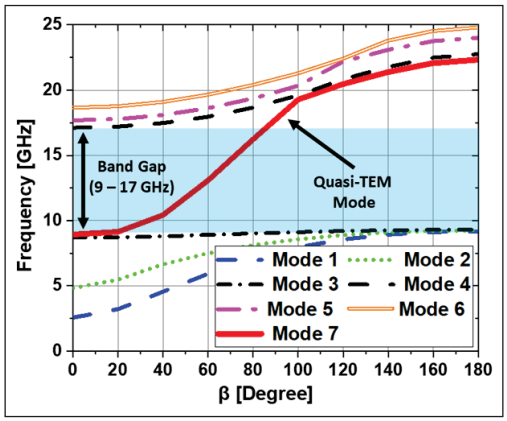

Figure 6.3 Dispersion diagram of the proposed PRGW unit cell

can be characterized using an eigenmode solver, a numerical technique available in 3D electromagnetic analysis software such as CST and HFSS.

For the eigenmode simulation of the PRGW unit cell, periodic boundary conditions are applied along the transverse directions to emulate an infinitely periodic structure. Perfect electric conductor (PEC) boundaries are imposed along the propagation axis to ensure proper wave confinement and mode behavior. This eliminates the need for Floquet ports, which are typically used in frequency-domain simulations. The eigenmode solver extracts the dispersion diagram, allowing for the identification of the stopband, where no propagating modes exist.

As shown in Fig. 6.3, the stopband covers a frequency range from 9 to 18 GHz, making it suitable for both X-band and Ku-band applications. The obtained stopband is in good agreement with the desired bandwidth of 3 GHz around the central frequency of 13.5 GHz, suitable for downlink satellite applications. Fig. 6.4 shows the electric field distribution at the central frequency of 13.5 GHz for a simulated waveguide, illustrating the PRGW's working principle. The electric field is entirely confined within the MSL ridge, with no propagation along the mushroom bed.

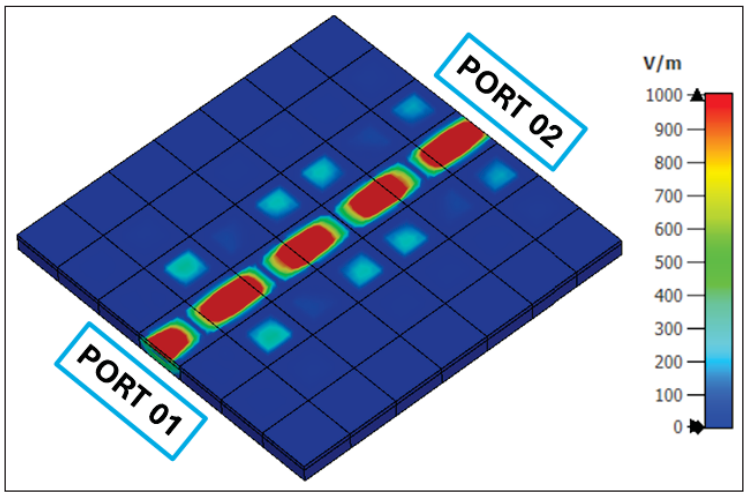

Figure 6.4 Electric field distribution of a simulated PRGW line

6.2.3 Proposed 3D-printed DRA MIMO Antenna Configuration

Based on the proposed PRGW unit cell described previously, a 4-port MIMO antenna configuration is designed with 4 slots and a DGS structure added between the slots element in order to enhance the isolation. The added DGS is based on our previous works in (Nakmouche, Deslandes, Nedil & Gagnon, c), where the DGS structure and position are automatically predicted using a developed ML-based inverse design approach for the highest isolation. The fabricated 4-port MIMO pre-assembled and assembled are shown in Figs. 6.5 and 6.6, respectively. As can be seen, all the layers must be properly aligned and attached using stainless screws.

In order to enhance the impedance bandwidth response, a 3D-printed multi-permittivity DR is placed above the four slots. To ensure accurate alignment between the slots and the DRs, we print four small DRs with a thin, optimized 0.5 mm height layer, having a permittivity of ϵ_r = 2.72, as shown in Fig. 6.6. The DRA is X-polarized because the excitation occurs in a Y-directed slot. Two different DRs prototyped using a low-cost desktop 3D printer are used in this work, namely: a small DR based on PLA material of ϵ_r = 2.72 (loss = 0.008) integrated into an alignment thin layer. The second one is a big DR having an air space underneath that is placed on top of the previous small DR as LEGO (one inside the other), and it is based on PLA material ϵ_r = 1.24 (loss = 0.004), as shown in Fig. 6.7. The

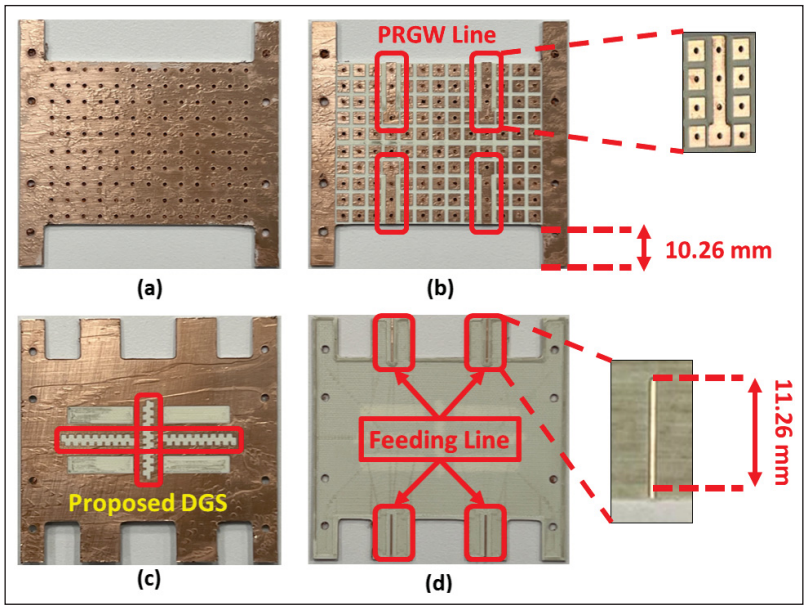

Figure 6.5 Disassembled fabricated 4-Port MIMO antenna (a) Bottom view of layer I (b) Top view of layer I (c) Top view of layer II (d) Bottom view of layer II

air space in the big DR serves to transform the impedance of the DRA to that of the slot by concentrating the fields underneath the DRA, thus improving the coupling performance (Weng, Wang, Jiao & Zhang, 2010).

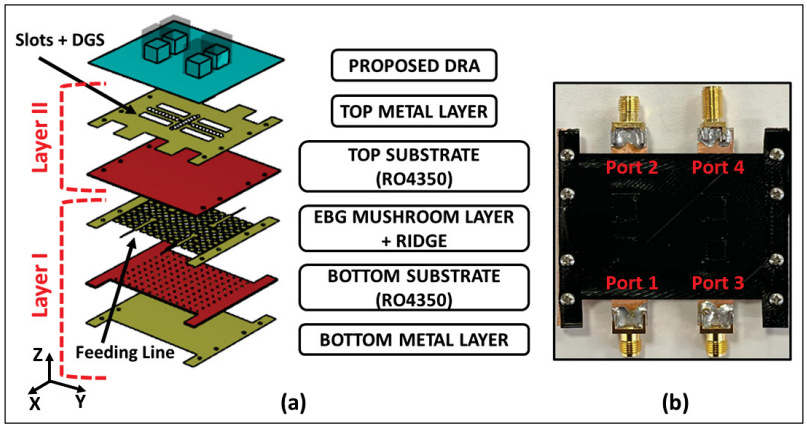

Figure 6.6 Fabricated 4-port MIMO antenna (a) Exploded view of the proposed 4-port MIMO antenna (3D model) (b) Assembled 4-port MIMO antenna with SMA port

As previously mentioned, the two different permittivities are achieved using two infills (ratio of PLA material to empty space): 100% for $\epsilon_r = 2.72$ and 18% for $\epsilon_r = 1.24$. The basic size before optimization of the two rectangular DR is determined using the following equation (Mongia, Ittibipoon & Cuhaci, 1994):

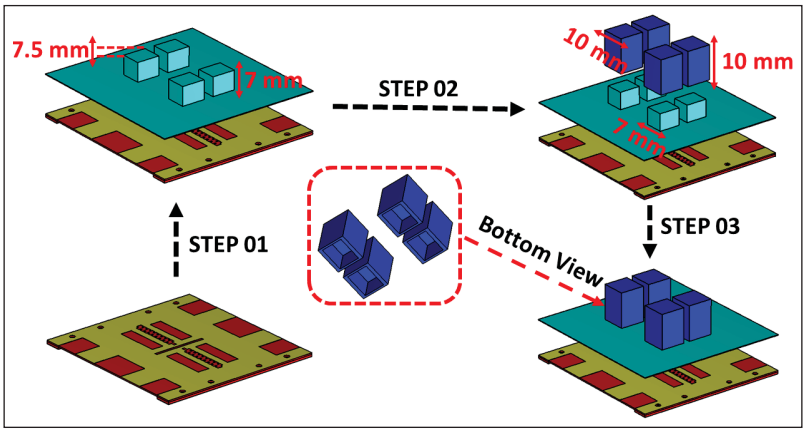

Figure 6.7 3D model 4-Port 3D printed DRA MIMO antenna with uniform DRA and with hybrid DRA

$$f_0 = \frac{c}{2\pi\sqrt{\epsilon_r}}\sqrt{k_x^2 + k_y^2 + k_z^2} \tag{6.1}$$

$$k_x = \frac{\pi}{a} \tag{6.2}$$

$$k_z = \frac{\pi}{2b} \tag{6.3}$$

$$d = \frac{2}{k_y \tanh(\frac{k_{y0}}{k_y})} \tag{6.4}$$

$$k_{y0} = \sqrt{k_x^2 + k_z^2} \tag{6.5}$$

Where ϵ_r is the relative dielectric constant of the material forming the DR and "a" and "b" are the width and length of the DR.

The enhancement in bandwidth is primarily due to the fact that the big DR includes an air space underneath the DR, thus lowering the effective air-dielectric constant of the DRA, which in turn lowers the Q-factor, leading to wideband enhancement. Filling the air gap with the small DR leads to multimode excitation at adjacent resonance frequencies, which further enhances the impedance bandwidth. The mode analysis is introduced in the following section.

6.2.4 Mode Analysis

In this section, we analyze how the wideband is achieved by investigating the electromagnetic (EM) field distribution. We can see from the simulated electric field vector distribution shown in Fig. 6.8 that the two DRs separately result in two distinct resonant modes in the passband. The TE111 mode related to the small DR at 12.5 GHz induces the first resonance, while the TE121 mode related to the big DR at 13.5 GHz induces the second resonance. Embedding the smaller DR into the larger DR led to obtaining the degenerate Mode B (Pan, Leung & Lu, 2019), enhancing impedance bandwidth further.

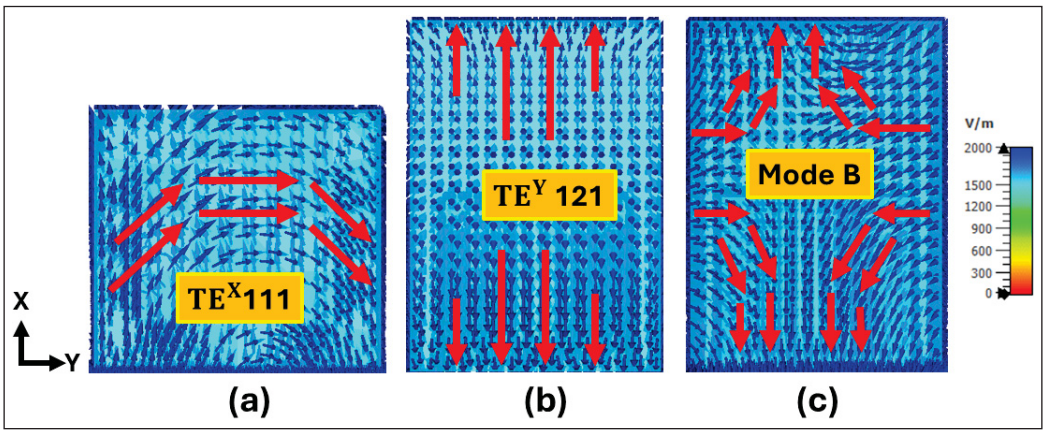

Figure 6.8 Electric field (E-field) distributions of the proposed multi-permittivity DRA (a) TE111 mode (Small DR) (b) TE121 mode (Big DR) (c) Hybrid Mode (multi-permittivity DRA)

6.3 Pattern Reconfiguration Mechanism

To enable physical beam reconfigurability, we introduce a compact, origami-based 8-port MIMO system that supports pattern diversity, as illustrated in Fig. 6.9. Inspired by (Hamza *et al.*, 2020), our design incorporates a surrogate hinge to enable folding.

To enhance foldability, we create the hinge by adding slots to standard PCB material, ensuring the slot width matches the substrate thickness. The hinge's stiffness and stress decrease with an increased number of torsional elements in series (n = 2) and in parallel (m = 3) (Figueiredo, 2017). To the best of our knowledge, there have been no previous studies on using such origami-foldable concepts in a PRGW-based structure.

The proposed MIMO antenna can be folded into various configurations; however, in this work, we focus on three specific fold states. These states are as follows: State I with a fold angle of 0°, State II with a fold angle of $\varphi = \pm 45°$, and State III with a fold angle of $\varphi = \pm 90°$.

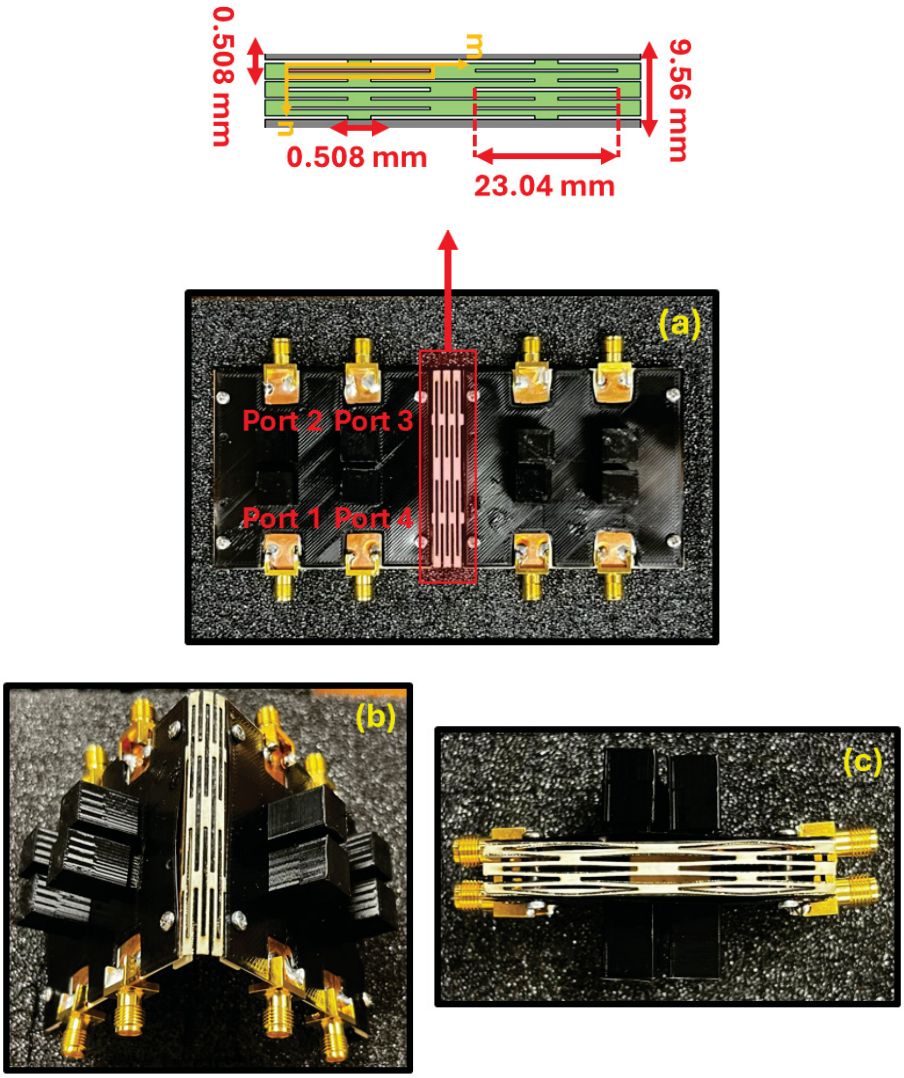

Figure 6.9 Fabricated prototype (a) State I (fold angle of 0°), (b) State II (fold angle of φ = 45°), (c) State III (fold angle of φ = 0°)

6.4 Simulated and Measured Results

In this section, we first present both the simulation of measurement s-parameters, isolation, and surface current distribution with and without DGS for the proposed 4-port MIMO antenna. Next, we analyze the realized gain and the impact of the loss tangent of PLA material on radiation efficiency. Lastly, we present the simulated and measured 2D radiation patterns for state I (without folding) and the simulated 3D radiation patterns for the 8-port MIMO antenna in all three states.

6.4.1 S-Paramters

From Fig. 6.10, we can notice that the addition of the big DR on top of the 4 small DR leads to enhancements in impedance bandwidth. Specifically, the bandwidth increases from 0.7 GHz (12.5–13 GHz) for the configuration with small DR to 2.22 GHz (12–15 GHz) for the configuration with big DR. Additionally, the use of the DGS structure keeps good isolation between the MIMO elements (40 dB) with a compact size of about 0.36λ between MIMO elements. The manufacturing, assembly, and misalignment difficulties typically observed during the fabrication and assembly process have not been taken into consideration during the simulation, leading to discrepancies between the simulated and measured results.

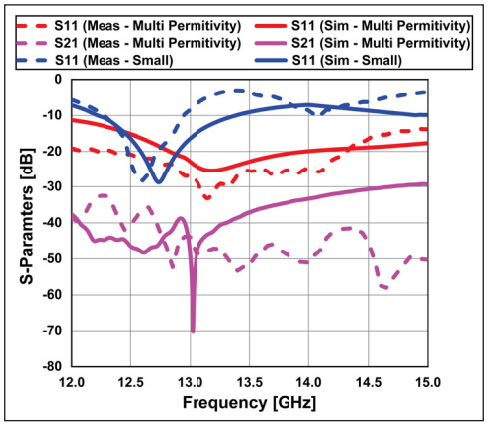

Figure 6.10 S-parameters of the proposed origami MIMO antenna

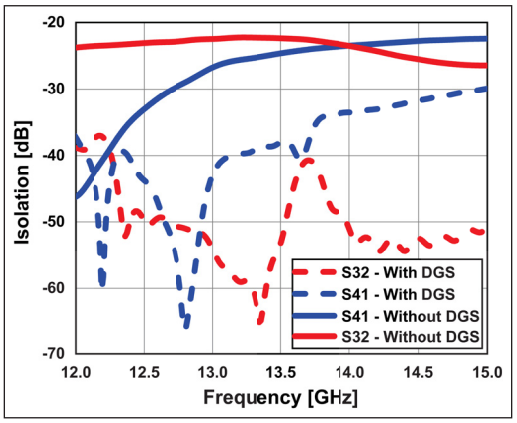

Figure 6.11 Isolation between the four ports of the proposed origami MIMO antenna

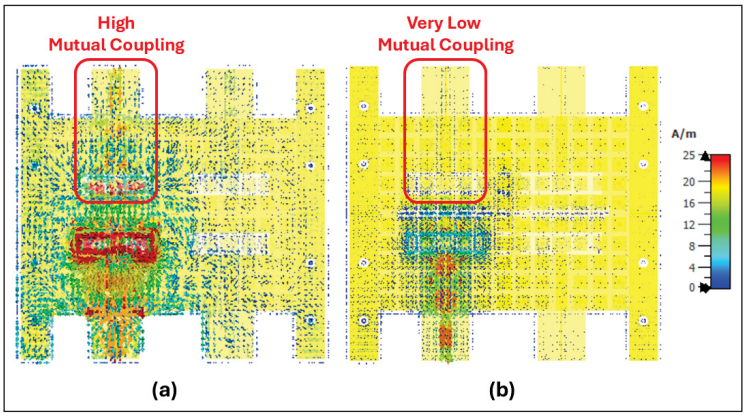

Figure 6.12 Surface current distribution: (a) With DGS (b) Without DGS

The isolation between the four ports for the configuration with and without DGS is plotted in Fig. 6.11. As can be seen, the isolation at the resonant frequency (13.5 GHz) when port 1 is excited is enhanced significantly from 20 dB (without DGS) to 40 dB (with DGS). Additionally, the current density distribution for the 4-port MIMO antenna,

with and without DGS, is shown in Fig. 6.12. As expected, incorporating DGS structure effectively reduces surface currents at adjacent radiating antennas. This decoupling method plays a crucial role in minimizing current flow between antennas, thereby improving isolation.

6.4.2 Realized Gain & Efficiency

Fig. 6.13 shows the measured and simulated realized gain varying between 6.8 and 7.5 dBi across the impedance bandwidth (12–15 GHz). With reference to Fig. 6.13, it can be observed that the measured gain is slightly lower than the simulated result between 13.75 and 15 GHz, but overall, a good agreement over the frequency band (12–15 GHz) can be noticed.

The discrepancy between the simulation and measured results is due to the fact that the simulated result did not take into account the effect of the connectors and cables. The maximum gain of 7.5 dBi is found at 13.5 GHz, and the gain across the impedance passband is between 7 and 7.5 dBi. It's worth emphasizing that a gain enhancement of approximately 0.5 to 1 dBi is observed when compared to the configuration with a small DR only.

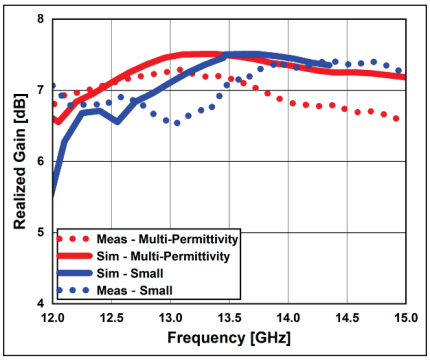

Figure 6.13 Realized gain

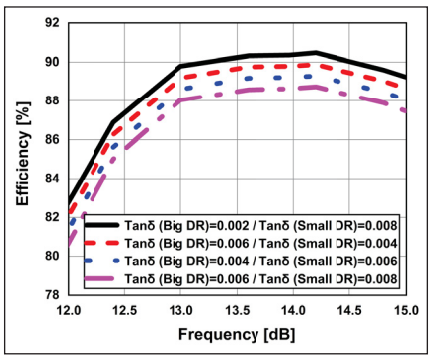

Figure 6.14 Radiation Efficiency

As the loss tangent of PLA material is relatively high, the impact on radiation efficiency is analyzed considering various loss tangent values for both small and big DR, as shown in Fig. 6.14. The efficiency achieved with low loss tangent value for both small and big DR shows a high efficiency of 90% in the frequency range of 13–15 GHz. However, for frequency ranges from 12 to 13 GHz, a value between 82%-90% is noticed. As the loss tangent value increases, the efficiency drops 2% from the previously achieved results.

6.4.3 Radiation Patterns

The antenna radiation pattern was measured in the anechoic chamber at Institut national de la recherche scientifique (INRS) Montreal, which facilitates characterization within the 0.8–40 GHz frequency range. Fig. 6.15(a) depicts

the measurement setup for the proposed antenna in State II at $\varphi = \pm 45°$, while Fig. 6.15(b) shows for State III at $\varphi = \pm 90°$.

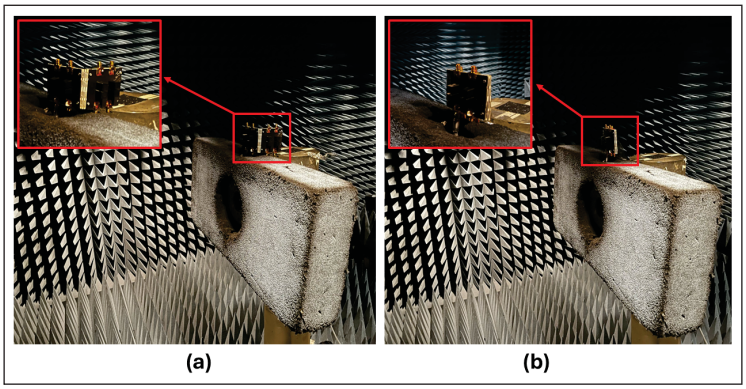

Figure 6.15 Proposed antenna inside the anechoic chamber: (a) State II at $\varphi = \pm 45°$, (b) State III at $\varphi = \pm 90°$

Based on this measurement setup, Fig. 6.16 presents the measured radiation characteristics of the proposed 4-port MIMO antenna configuration at 13.5 GHz, both with and without the proposed 3D-printed DRA, in the E-plane and H-plane, respectively. Without the DRA, the antenna exhibits a near broadside radiation pattern. However, when the DRA is integrated, the radiation pattern experiences a noticeable beam tilt, with a maximum tilt angle of 60° in the E-plane and 25° in the H-plane. This tilt, induced by the DRA, significantly alters the antenna's radiation characteristics, which may influence coverage or directional gain. The impact of the DRA presence is thus evident in the shifted radiation pattern, which deviates from the broadside pattern. A discrepancy between the simulated and measured radiation patterns is observed, likely due to slight misalignment during antenna assembly, which may have affected the positioning of the DRA.

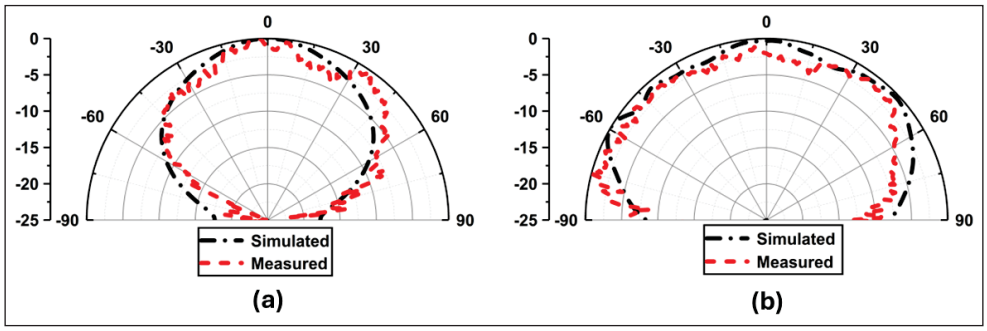

Figure 6.16 Simulated and measured radiation patterns at 13.5 GHz (a) E-Plane (Without DR) (b) H-Plane (Without DR) (c) E-Plane (With DR) (d) H-Plane (With DR)

Fig. 6.17 presents the analysis of simulated 3D radiation patterns for three folded configurations. Depending on the folding state, multiple beams are observed, with a consistent gain of 7.5 dBi. In Configuration I (no folding), a

single beam at $\varphi = 90°$ is visible (Fig. 6.17 (a)). In Configuration II (single-fold state), two beams at $\varphi = \pm 45°$ (Fig. 6.17 (b)). Finally, Configuration III (double-fold state) achieves two beams at $\varphi = \pm 90°$ (Fig. 6.17 (c)).

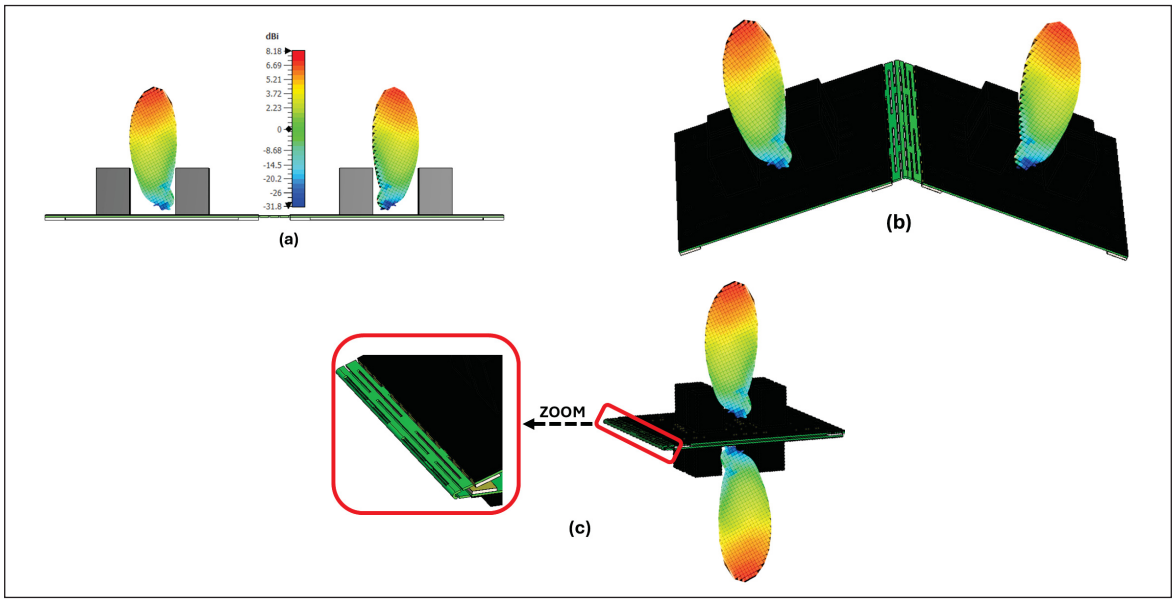

Figure 6.17 Simulated 3D polar radiation pattern of the proposed origami PRGW MIMO antenna at three configuration states: (a) State I ($\theta = 0°$), (b) State II ($\varphi = \pm 45°$), (c) State III ($\varphi = \pm 90°$).

6.5 MIMO Antenna Performance Evaluation

The efficiency of a MIMO antenna system is determined by two key parameters: the Envelope Correlation Coefficient (ECC) and Diversity Gain (DG). These parameters assess signal correlation and the overall diversity performance of the system. The ECC quantifies the degree of correlation between antenna elements. Lower ECC values indicate better isolation, leading to improved signal quality and reduced interference. It can be derived using far-field radiation patterns or S-parameters. Using the far-field method, ECC is obtained by integrating the radiation fields over a given angular space as expressed in equation (6) and to ensure effective diversity performance, ECC should remain below 0.5 (El-Din, Shams, Allam, Gaafar, Elhennawy & Fathy Abo Sree, 2022; Khan, Capobianco, Najam, Shoaib, Autizi & Shafique, 2014):

$$\rho_{e_{ij}} = \frac{\left| \int \int_{4\pi} \mathbf{F}_i(\theta, \phi) \cdot \mathbf{F}_j^*(\theta, \phi) d\Omega \right|^2}{\left(\int \int_{4\pi} |\mathbf{F}_i(\theta, \phi)|^2 d\Omega \right) \left(\int \int_{4\pi} |\mathbf{F}_j(\theta, \phi)|^2 d\Omega \right)} \tag{6.6}$$

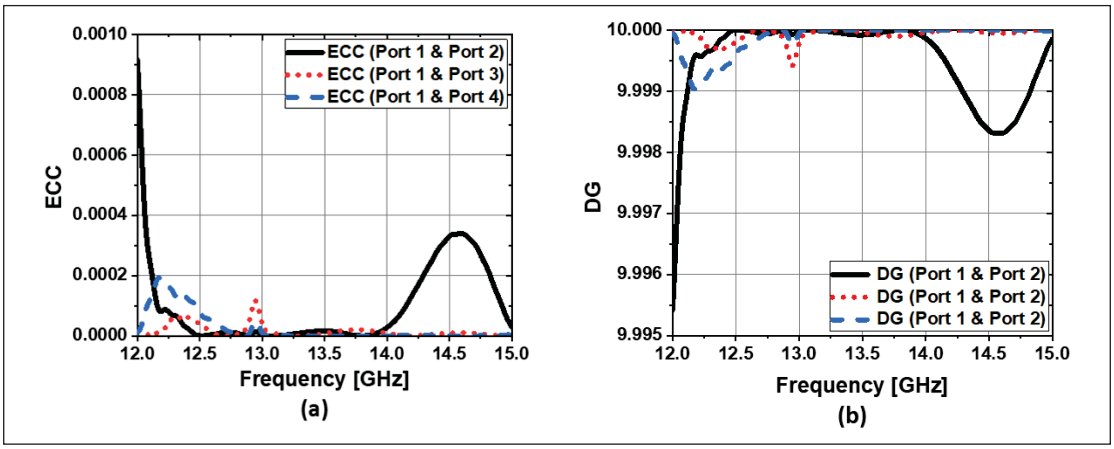

Figure 6.18 (a) Envelope correlation coefficient (ECC); (b) Diversity gain (DG) performance of the proposed MIMO antenna

Diversity Gain (DG), as expressed in Equation (8) (Yin, Chen, Chang, Li & Khamas, 2021b), measures a system's effectiveness in mitigating fading effects. Given the inverse relationship between ECC and DG, a lower ECC results in a higher DG, thereby enhancing overall diversity performance.

$$DG = 10\sqrt{1 - ECC^2} \tag{6.7}$$

Fig. 6.18(a) illustrates the ECC values obtained from simulations, demonstrating low correlation across all port pairs. The ECC remains below 10^{-3} for port (1,2) with a slight peak around 14.5 GHz, while ports (1,3) and (1,4) exhibit even lower values, ensuring good isolation and diversity. Fig. 6.18(b) presents the DG values, which stay close to the ideal 10 dB across the frequency range. A minor deviation is observed near 14.5 GHz for port (1,2), but overall, the results confirm good diversity performance, reinforcing the effectiveness of the MIMO antenna configuration.

6.6 Comparison with other similar reported works in literature

The 3D-printed DRA MIMO antenna system is compared to the reported works on Ku-band MIMO systems in Table 6.1. Several comparative metrics are considered, including the bandwidth, the edge-to-edge distance between MIMO elements, realized gain, and the mutual coupling. Even though the edge-to-edge distance of the works reported in (Belazzoug, Messaoudene, Aidel, Nedil & Kishk, 2020; et al., 2023b) is shorter and more compact, our proposed MIMO antenna outperforms them in terms of isolation, bandwidth, and gain. Compared to (Liang, Chen, Zeng & Chu, 2023; Zhang, Deng, Li, Sun & Guo, 2019c), it is shown that our proposed design is more compact and presents higher performance in terms of isolation, bandwidth, and gain. It is essential to emphasize that the

proposed MIMO system can be adopted into vast MIMO systems with more radiating elements (4×4, 16×16) that can be used for IoS applications.

Table 6.1 Comparison with other reported works in literature

Ref.	**Gain (dB)**	**Edge-to-Edge Distance (λ_0)**	**Isolation (dB)**	**Bandwidth (GHz)**
(Belazzoug *et al.*, 2020)	6.5	0.20	18	2.60
(et al., 2023b)	4.59	0.066	24	0.80
(Liang *et al.*, 2023)	3.75	NA	15	0.40
(Zhang *et al.*, 2019c)	NA	0.40	24	1.83
Our Work	8.0	0.36	40	2.22

6.7 Conclusion

A low-cost origami PRGW wideband MIMO antenna with additively manufactured DRs, operating from 12 to 15 GHz, is presented in this paper. For the first time, the proposed antenna integrates PRGW with a conventional surrogate hinge architecture, enabling full 360° mechanical movement to achieve pattern diversity without compromising electromagnetic functionality. Wideband impedance bandwidth is achieved by exciting various modes (TE11, TE21, and hybrid mode B) with two low-cost multi-permittivity Polylactic Acid (PLA) materials: ϵ_{r1} = 2.72 (100% infill) and ϵ_{r2} = 1.24 (18% infill), using a 3D printer. The compact size, high isolation (> 40 dB), gain of 7.5 dB at 13.5 GHz, and radiation efficiency (85%) make the proposed MIMO antenna a good candidate for massive MIMO systems with robust beam reconfigurable performance and packable capability.

CONCLUSION AND RECOMMENDATIONS

7.1 Summary

This dissertation presents a machine learning-aided design paradigm for ridge gap waveguide (RGW) and periodic ridge gap waveguide (PRGW)-based components, introducing an end-to-end ML framework that enables a fully automated and optimized design methodology. This framework represents a novel contribution to microwave engineering, particularly in the context of fully metallic 3D-printed waveguide structures, offering an efficient alternative to conventional electromagnetic (EM) design techniques. The research encompasses a broad frequency range of 3 to 300 GHz, demonstrating applicability in millimeter-wave and sub-THz communication systems.

The study commences with the generation of an extensive EM simulation-based dataset for 3D-printed RGW and PRGW unit cells, ensuring comprehensive parametric coverage. This dataset is leveraged for the training and evaluation of various machine learning models, with rigorous selection criteria based on prediction accuracy, computational efficiency, and generalization capability. The optimal models are integrated into a fully automated ML-driven design workflow, facilitating the synthesis of complex RGW architectures. Notably, the framework is validated through the design of a highly isolated 90° bent 4-port RGW structure, underscoring its capability to address intricate waveguide geometries.

Furthermore, the dissertation introduces, for the first time, a scalable genetic programming (GP)-based synthesis methodology for PRGW unit cells. This approach significantly reduces computational complexity while achieving superior performance metrics compared to conventional numerical optimization techniques. Notably, it formulates explicit mathematical models for the parametric synthesis of PRGW unit cells based on predefined stop-band characteristics, ensuring enhanced precision and design flexibility.

For MIMO antenna design, an Artificial Neural Network (ANN)-based inverse modeling approach is developed to optimize a newly structured Defected Ground Structure (DGS). This methodology provides a computationally efficient solution for the design of massive MIMO configurations, including high-order arrays such as 4×4 and 16×16, resulting in significant improvements in inter-element isolation and radiation performance.

The research yields in the application of the proposed ANN-based approach to the design of a low-cost, origami-inspired compact 4×4 MIMO antenna, utilizing multi-permittivity dielectric resonators (DRs) to enhance bandwidth while enabling radiation pattern reconfigurability. This innovative approach not only reduces fabrication costs

but also establishes a framework for the next generation of adaptive and reconfigurable wireless communication systems.

7.2 Discussion and Recommendations

In our previous research, we demonstrated that various AI models, including genetic programming (GP), were applied for the first time in electromagnetic (EM) research to assist engineers in designing PRGW- and RGW-based EM structures and antennas. This approach accelerates the design process across a broad frequency range, spanning from MHz to THz. To extend the advancements achieved in this doctoral research, several key recommendations can be outlined for future exploration:

7.2.1 GAN/LLM-Based Synthetic Data Generation for EM Structures

The success of AI-driven EM structure design heavily depends on the quality, quantity, and availability of data. Unlike fields such as computer vision, electronics particularly antenna design—lacks standardized datasets. In our research, datasets are generated using EM simulators such as Ansys HFSS and CST Studio, encompassing extensive simulations on PRGW-, RGW-, and SIW-based structures over a wide frequency range (MHz to THz).

Moving forward, we plan to investigate generative adversarial networks (GANs) and large language models (LLMs) to generate synthetic datasets, incorporating flexible materials and 3D-printed bio-sourced materials. This approach will also extend to passive components such as couplers, filters, and interconnections for 3D/4D SoP. By training a GAN or LLM on these datasets, the model learns the underlying data distribution, capturing knowledge from numerous design iterations and optimization rounds. Our goal is to develop a framework that enables engineers and researchers to generate datasets for any given EM structure using only a limited set of samples.

7.2.2 Hybrid Genetic Programming and Deep Learning Inverse Design Approach

In our previous research, we introduced a scalable GP-based approach for synthesizing a PRGW unit cell, applicable to stop-band frequencies from 3 to 300 GHz. GP generates closed-form mathematical expressions to predict unit cell dimensions based on predefined stop-band frequencies and substrate materials. This method enhances reliability and reduces computational time, outperforming test-and-trial and traditional machine learning techniques.

A key advantage of this approach is its ability to generate general closed-form formulas, making it applicable to other complex EM structures lacking analytical design equations. To advance this research, we aim to integrate deep

learning techniques, making the approach suitable for designing miniature and reconfigurable antennas, passive components (filters, couplers), and interconnections. This includes DRAs, GRIN lens antennas, waveguides, and 2D/3D artificial magnetic conductor (AMC) structures, all based on 3D-printing technology. The incorporation of deep learning enhances adaptability and performance, facilitating efficient and flexible designs across a broad frequency spectrum (MHz to THz).

7.2.3 Real-World Deployment in EM Structure Design Workflow

Our research extends beyond theoretical investigations by developing a practical framework that integrates AI-driven models with conventional EM modeling software, such as Ansys HFSS and CST Studio Suite. This implementation will allow us to evaluate the effectiveness of our methodologies in the complex and dynamic field of EM structure design.

Following deployment, we will conduct a comprehensive analysis to assess the impact of our AI-assisted models on RF and antenna engineering workflows. Specifically, we will examine improvements in productivity, the quality of AI-inverse-designed EM structures, and overall design efficiency. Our deployment efforts will focus on designing 3D/4D SoP architectures, including 3D-printed DRAs, GRIN lens antennas, passive components, and interconnections.

The primary applications include CubeSat systems and flexible wearable devices for tactical wireless communications in harsh environments. Ultimately, our goal is to develop a framework that enables the automatic and accelerated integration of multiple components and antennas into a SoP solution.

LIST OF REFERENCES

Ahmed, O. M. H., Sebak, A.-R. & Denidni, T. A. (2012). A novel butterfly shaped multilayer backward microstrip hybrid coupler for ultrawideband applications. *Microwave and Optical Technology Letters*, 54(10), 2231-2237.

Al-Alem, Y., Sifat, S. M., Antar, Y. M. M. & Kishk, A. A. (2023a). Circularly Polarized Ka-Band High-Gain Antenna Using Printed Ridge Gap Waveguide and 3-D-Printing Technology. *IEEE Transactions on Antennas and Propagation*, 71(9), 7644-7649.

Al-Alem, Y., Sifat, S. M., Antar, Y. M. M. & Kishk, A. A. (2023b). Circularly Polarized Ka-Band High-Gain Antenna Using Printed Ridge Gap Waveguide and 3-D-Printing Technology. *IEEE Transactions on Antennas and Propagation*, 71(9), 7644-7649.

Ali, M. M. M. & Sebak, A. (2018). Compact printed ridge gap waveguide crossover for future 5G wireless communication system. *IEEE Microwave and Wireless Components Letters*, 28(7), 549-551.

Ali, M. M. M., Shams, S. I. & Sebak, A.-R. (2019). Ultra-wideband printed ridge gap waveguide hybrid directional coupler for millimetre wave applications. *IET Microwaves, Antennas and Propagation*, 13(8), 1181–1187.

Ali, M. M. M., Afifi, I. & Sebak, A. (2020a). A dual-polarized magneto-electric dipole antenna based on printed ridge gap waveguide technology. *IEEE Transactions on Antennas and Propagation*, 68(11), 7589-7594.

Ali, M. M. M., Afifi, I. & Sebak, A.-R. (2020b). A dual-polarized magnetoelectric dipole antenna based on printed ridge gap waveguide technology. *IEEE Transactions on Antennas and Propagation*, 68(11), 7589-7594.

Ali, W. A. & Ibrahim, A. A. (2017). A compact double-sided MIMO antenna with an improved isolation for UWB applications. *AEU - International Journal of Electronics and Communications*, 82, 7-13. doi: https://doi.org/10.1016/j.aeue.2017.07.031.

Alibakhshikenari, M., Khalily, M., Virdee, B. S., See, C. H., Abd-Alhameed, R. A. & Limiti, E. (2019). Mutual Coupling Suppression Between Two Closely Placed Microstrip Patches Using EM-Bandgap Metamaterial Fractal Loading. *IEEE Access*, 7, 23606-23614.

Alonso-González, L., Rico-Fernández, J., Vaquero, F. & Arrebola, M. (2023). Metal-Only Additive-Manufactured in Monolithic Piece Array for Sum/Difference Pattern in Ka-Band. *IEEE Transactions on Antennas and Propagation*, 71(8), 6413–6422.

Amillia, F., Setijadi, E. & Hendrantoro, G. (2022). The Effect of Parasitic Patches Addition on Bandwidth Enhancement and Mutual Coupling in 2 × 2 Sub-Arrays. *IEEE Access*, 10, 72057-72064.

An, S. et al. (2022). Ultrawideband Schiffman Phase Shifter Designed With Deep Neural Networks. *IEEE Transactions on Microwave Theory and Techniques*, 70(11), 4694-4705.

Ansari, M., Zhu, H., Shariati, N. & Guo, Y. J. (2019). Compact Planar Beamforming Array With Endfire Radiating Elements for 5G Applications. *IEEE Transactions on Antennas and Propagation*, 67(11), 6859-6869.

Arani, M. S., Shahidi, R. & Zhang, L. (2024). A State-of-the-Art Survey on Advanced Electromagnetic Design: A Machine-Learning Perspective. *IEEE Open Journal of Antennas and Propagation*.

Arapoglou, P.-D., Liolis, K., Bertinelli, M., Panagopoulos, A., Cottis, P. & Gaudenzi, R. D. (2011). MIMO over satellite: A review. *IEEE Communications Surveys Tutorials*, 13(1), 27-51.

Atlantic Council. (2011). Could 3D Printing Change the World? Accessed: Mar. 11, 2025, Consulted at https://www.atlanticcouncil.org/in-depth-research-reports/report/could-3d-printing-change-the-world.

Attia, H., Kishk, A. A., Abdalla, M. A., Gaya, S., Hamza, A. & Mahmoud, A. (2021). Ridge gap waveguide antenna array with improved mutual isolation for millimeter-wave applications. *International Journal of RF and Microwave Computer-Aided Engineering*, 31(11), e22831.

Attia, H., Abdalrazik, A., Sharawi, M. S. & Kishk, A. A. (2023). Wideband Circularly Polarized Millimeter-Wave DRA Array for Internet of Things. *IEEE Internet of Things Journal*, 10(11), 9597-9606.

B-Suwailam, M. M., Siddiqui, O. F. & Ramahi, O. M. (2010). Mutual coupling reduction between microstrip patch antennas using slotted-complementary split-ring resonators. *IEEE Antennas and Wireless Propagation Letters*, 9, 876-878.

Baghernia, E., Ali, M. M. M. & Sebak, A. R. (2020). 2 × 2 slot spiral cavity-backed antenna array fed by printed gap waveguide. *IEEE Access*, 8, 170609-170617.

Baghernia, E., Movahedinia, R. & Sebak, A. (2021). Broadband compact circularly polarized spiral antenna array fed by printed gap waveguide for millimeter-wave applications. *IEEE Access*, 9, 86-95.

Balanis, C. A. (2005). *Antenna Theory Analysis and Design* (ed. Third).

Bayat-Makou, N. & Kishk, A. A. (2017). Millimeter-wave substrate integrated dual level gap waveguide horn antenna. *IEEE Transactions on Antennas and Propagation*, 65(12), 6847-6855.

Bayat-Makou, N. & Kishk, A. A. (2018a). Realistic Air-Filled TEM Printed Parallel-Plate Waveguide Based on Ridge Gap Waveguide. *IEEE Transactions on Microwave Theory and Techniques*, 66(5), 2128–2140.

Bayat-Makou, N. & Kishk, A. A. (2018b). Realistic Air-Filled TEM Printed Parallel-Plate Waveguide Based on Ridge Gap Waveguide. *IEEE Transactions on Microwave Theory and Techniques*, 66(5), 2128-2140. doi: 10.1109/TMTT.2018.2811487.

Belazzoug, M., Messaoudene, I., Aidel, S., Nedil, M. & Kishk, A. A. (2020). Ultra-compact 4-port DR antenna for multi-input multi-output standards. *International Journal of RF and Microwave Computer-Aided Engineering*, 30(2), e22145.

Beltayib, A. & Sebak, A. (2019a). Analytical design procedure for forward wave couplers in RGW technology based on hybrid PEC/PMC waveguide model. *IEEE Access*, 7, 119319–119331.

Beltayib, A. & Sebak, A. R. (2019b). Analytical Design Procedure for Forward Wave Couplers in RGW Technology Based on Hybrid PEC/PMC Waveguide Model. *IEEE Access*, 7, 119319–119331.

Beltayib, A., Afifi, I. & Sebak, A. R. (2019). 4×4-Element Cavity Slot Antenna Differentially-Fed by Odd Mode Ridge Gap Waveguide. *IEEE Access*, 7, 48185–48195.

Berenguer, A., Fusco, V., Zelenchuk, D. E., Sánchez-Escuderos, D., Baquero-Escudero, M. & Boria-Esbert, V. E. (2016a). Propagation Characteristics of Groove Gap Waveguide Below and Above Cutoff. *IEEE Transactions on Microwave Theory and Techniques*, 64(1), 27–36.

Berenguer, A., Fusco, V., Zelenchuk, D. E., Sánchez-Escuderos, D., Baquero-Escudero, M. & Boria-Esbert, V. E. (2016b). Propagation Characteristics of Groove Gap Waveguide Below and Above Cutoff. *IEEE Transactions on Microwave Theory and Techniques*, 64(1), 27–36.

Berenguer, A., Fusco, V., Zelenchuk, D. E., Sánchez-Escuderos, D., Baquero-Escudero, M. & Boria-Esbert, V. E. (2016c). Propagation Characteristics of Groove Gap Waveguide Below and Above Cutoff. *IEEE Transactions on Microwave Theory and Techniques*, 64(1), 27-36.

Bertrand, P., Bayle, F., Combe, C., Goeuriot, P. & Smurov, I. (2007). Ceramic components manufacturing by selective laser sintering. *Applied Surface Science*, 254, 989–992.

Bhartia, P., Ittipiboon, A., Garg, R. & Bahl, I. (2001). *Microstrip Antenna Design Handbook*. London: Artech House Antennas and Propagation Library.

Birgermajer, S., Janković, N., Radonić, V., Crnojević-Bengin, V. & Bozzi, M. (2018). Microstrip-ridge gap waveguide filter based on cavity resonators with mushroom inclusions. *IEEE Trans. Microw. Theory Techn.*, 66(1), 136–146.

Boas, E. C. V., Ribeiro, J. A. P., de Figueiredo, F. A. P. & Mejía-Salazar, J. R. (2024). 3-D-Printed All-Dielectric Corner-Like Bragg Reflector for Antenna Gain Enhancement. *IEEE Antennas and Wireless Propagation Letters*, 23(2), 558–562.

Bower, J. L. & Christensen, C. M. (1995). Disruptive Technologies: Catching the Wave. Accessed: Mar. 29, 2022, Consulted at https://hbr.org/1995/01/disruptive-technologies-catching-the-wave.

Brazalez, A. A., Zaman, A. U. & Kildal, P. (2012a). Improved microstrip filters using PMC packaging by lid of nails. *IEEE Trans. Compon., Packag., Manuf. Technol.*, 2(7), 1075–1084.

Brazalez, A. A., Zaman, A. U. & Kildal, P.-S. (2012b). Improved Microstrip Filters Using PMC Packaging by Lid of Nails. *IEEE Transactions on Components, Packaging and Manufacturing Technology*, 2(7), 1075-1084. doi: 10.1109/TCPMT.2012.2190931.

Cai, J., Chen, T., Qi, Y. et al. (2025). Fibrosis and inflammatory activity diagnosis of chronic hepatitis C based on extreme learning machine. *Scientific Reports*, 15, 11. doi: 10.1038/s41598-024-84695-4.

Cai, J., Li, Y., Liu, B., Wu, Z., Zhu, S., Chen, Q., Lei, Q., Hou, H., Guo, Z., Jiang, H., Guo, S., Wang, F., Huang, S., Zhu, S., Fan, X. & Tao, S. (2024). Developing Deep LSTMs With Later Temporal Attention for Predicting COVID-19 Severity, Clinical Outcome, and Antibody Level by Screening Serological Indicators Over Time. *IEEE Journal of Biomedical and Health Informatics*, 28(7), 4204-4215.

Cao, D., Li, Y., Wang, J., Sun, F. & Ge, L. (2021). Millimeter-wave three-dimensional substrate-integrated OMT-fed horn antenna using vertical and planar groove gap waveguides. *IEEE Trans. Microw. Theory Techn.*, 69(10), 4448–4459.

Castillo-Tapia, P., Zetterstrom, O., Algaba-Brazález, A., Manholm, L., Johansson, M., Fonseca, N. J. G. & Quevedo-Teruel, O. (2023). Two-Dimensional Beam Steering Using a Stacked Modulated Geodesic Luneburg Lens Array Antenna for 5G and Beyond. *IEEE Transactions on Antennas and Propagation*, 71(1), 487-496. doi: 10.1109/TAP.2022.3217175.

Celik, F. T., Yarovoy, A. & Aslan, Y. (2023). From Cooling to Coupling and Back: A Novel Beam-Switching Heatsink Antenna Array With CSRR Embedded Isolation Wall. *IEEE Antennas and Wireless Propagation Letters*, 22(11), 2690-2694.

Chaudhary, R. K., Srivastava, K. V. & Biswas, A. (2015). Variation of permittivity in radial direction in concentric half-split cylindrical dielectric resonator antenna for wideband application. *International Journal of RF and Microwave Computer-Aided Engineering*, 25, 321–329.

Chen, C., Chen, J. & Hong, W. (2022a). Differentially Fed Dual-Polarized 2-D Multibeam Dielectric Resonator Antenna Array Based on Printed Ridge Gap Waveguide. *IEEE Transactions on Antennas and Propagation*, 70(9), 7967-7977.

Chen, C., Chen, J., Zhou, J., Wen, L. & Hong, W. (2024a). Printed Ridge Gap Waveguide Fed Filtering Magnetoelectric Dipole Antenna Array for 5G Millimeter-Wave Applications. *IEEE Transactions on Antennas and Propagation*, 72(3), 2849-2854.

Chen, C., Chen, J., Zhou, J., Wen, L. & Hong, W. (2024b). Printed Ridge Gap Waveguide Fed Filtering Magnetoelectric Dipole Antenna Array for 5G Millimeter-Wave Applications. *IEEE Transactions on Antennas and Propagation*, 72(3), 2849-2854. doi: 10.1109/TAP.2024.3358384.

Chen, J., Shen, D., Zhang, X. & Sa, Y. (2021). Integrated substrate groove gap waveguide and application for filter design. *Int. J. RF Microw. Comput.-Aided Eng.*, 31(11), e22830.

Chen, J.-X., Ke, Y.-H., Yang, L.-L. & Yang, W.-W. (2022b). Pattern-Reconfigurable Dielectric Resonator Antenna With Endfire Beam-Scanning Feature. *IEEE Antennas and Wireless Propagation Letters*, 21(7), 1398–1402.

Chen, S.-H., Row, J.-S. & Wong, K.-L. (2007). Reconfigurable square-ring patch antenna with pattern diversity. *IEEE Transactions on Antennas and Propagation*, 55(2), 472–475.

Chen, X. et al. (2022c). Simultaneous Decoupling and Decorrelation Scheme of MIMO Arrays. *IEEE Transactions on Vehicular Technology*, 71(2), 2164-2169.

Christodoulou, C. & Georgiopoulos, M. (2001). *Applications of Neural Networks in Electromagnetics*.

Creech, G. L., Paul, B., Lesniak, C., Jenkins, T., Lee, R. & Calcatera, M. (1996, Jun.). Artificial neural networks for accurate microwave CAD applications. *IEEE MTT-S International Microwave Symposium Digest*, pp. 733-736.

Cui, L., Zhang, Y., Zhang, R. & Liu, Q. H. (2020). A Modified Efficient KNN Method for Antenna Optimization and Design. *IEEE Transactions on Antennas and Propagation*, 68(10), 6858–6866.

Dadashzadeh, G., Kargar, M., Torabi, Y. & Rahmati, B. (2016). Broad-band and wide scan phased array element design using data mining. *Appl. Comput. Electromagn. Soc. J.*, 31(3), 244–251.

Demuth, H. B., Beale, M. H. & Inc., M. (2001). Neural Network Toolbox for Use with MATLAB: User's Guide. Natick, MA, USA: MathWorks.

Deng, H., Zhu, L. & Ouyang, Z.-A. (2023). Systematic Design Method for Mutual Coupling Reduction in Closely Spaced Patch Antennas. *IEEE Open Journal of Antennas and Propagation*, 4, 349-360.

Deslandes, D. & Wu, K. (2001). Integrated Microstrip and Rectangular Waveguide in Planar Form. *IEEE Microwave and Wireless Components Letters*, 11(2), 68-70. doi: 10.1109/7260.914305.

Diaz, S., Diaz, M., Rajo-Iglesias, E. & Pizarro, F. (2024). 3-D-Printed High-Gain Multisection DRA With Symmetric Radiation Pattern. *IEEE Antennas and Wireless Propagation Letters*, 23(5), 1458–1462.

Djerafi, T. & Wu, K. (2007). Super-compact substrate integrated waveguide cruciform directional coupler. *IEEE Microwave and Wireless Components Letters*, 17(11), 757-759.

Doghri, A., Ghiotto, A., Djerafi, T. & Wu, K. (2014). Broadband E-Plane Junction for Three-Dimensional Substrate Integrated Waveguide Circuits and Systems. *IEEE Microwave and Wireless Components Letters*, 24(11), 739–741.

Doghri, A., Djerafi, T., Ghiotto, A. & Wu, K. (2015). Substrate Integrated Waveguide Directional Couplers for Compact Three-Dimensional Integrated Circuits. *IEEE Transactions on Microwave Theory and Techniques*, 63(1), 209–221.

Dyab, W. M., Ibrahim, M. S., Sakr, A. A. & Wu, K. Maximizing the Gap Height in Gap-Waveguides With Helical Wires Operating at the Vicinity of Resonance. *IEEE Transactions on Microwave Theory and Techniques*.

Ebrahimpouri, M., Quevedo-Teruel, O. & Rajo-Iglesias, E. (2017). Design guidelines for gap waveguide technology based on glide-symmetric holey structures. *IEEE Microwave and Wireless Components Letters*, 27(6), 542–544.

Ebrahimpouri, M., Rajo-Iglesias, E., Sipus, Z. & Quevedo-Teruel, O. (2018). Cost-effective gap waveguide technology based on glide-symmetric holey EBG structures. *IEEE Transactions on Microwave Theory and Techniques*, 66(2), 927–934.

El-Din, M. S. H. S., Shams, S. I., Allam, A. M. M. A., Gaafar, A., Elhennawy, H. M. & Fathy Abo Sree, M. (2022). SIGW Based MIMO Antenna for Satellite Down-Link Applications. *IEEE Access*, 10, 35965-35976. doi: 10.1109/ACCESS.2022.3160473.

El Misilmani, H. M., Naous, T. & Al Khatib, S. K. (2020). A review on the design and optimization of antennas using machine learning algorithms and techniques. *International Journal of RF and Microwave Computer-Aided Engineering*, 30(10), e22356. doi: https://doi.org/10.1002/mmce.22356.

et al., A. V. (2019). Compact integrated full-duplex gap waveguide-based radio front end for multi-Gbit/s point-to-point backhaul links at E-band. *IEEE Transactions on Microwave Theory and Techniques*, 67(9), 3783–3797.

et al., B. Z. (2023a). A Novel Cruciform TE10/TE20 Dual-Mode Power Divider Based on Groove Gap Waveguides. *IEEE Transactions on Microwave Theory and Techniques*, 71(12), 5246–5256.

et al., F. C. (2017a). Overview on additive manufacturing technologies. *Proceedings of the IEEE*, 105(4), 593–612.

et al., F. C. (2017b). Overview on additive manufacturing technologies. *Proceedings of the IEEE*, 105(4), 593–612.

et al., G. A. (2018). 3-D printing of high-performance feed horns from Ku- to V-bands. *IEEE Antennas and Wireless Propagation Letters*, 17, 2036–2040.

et al., G. H. (2021). Machine learning for electronic design automation: A survey. *ACM Transactions on Design Automation of Electronic Systems*, 26(5), 1-46.

et al., M. M. (2023b). Mutual Coupling Reduction Between Two Tightly Packed Half-Split Cylindrical Dielectric Resonator Antennas. *IEEE Transactions on Antennas and Propagation*, 71(12), 9974–9979.

et al., M. S. H. S. E.-D. (2020). Approach for Determination of the Stop Band for Ridge Gap Waveguide. *2020 7th International Conference on Electrical and Electronics Engineering (ICEEE)*, pp. 72–75. doi: 10.1109/ICEEE49618.2020.9102494.

et al., P. S.-O. (2023c). Manufacturing guidelines for W-band full metal waveguide devices: Selecting the most appropriate technology. *IEEE Antennas and Propagation Magazine*, 65(2), 48–62.

et al., X. Z. (2022). Design of 3-D Integrated SIW Multiband Bandpass Filter With Split-Type Extended Doublet Topology. *IEEE Transactions on Components, Packaging and Manufacturing Technology*, 12(10), 1681–1691.

et al., Y. S. (2023d). Gap Waveguide Technology: An Overview of Millimeter-Wave Circuits Based on Gap Waveguide Technology Using Different Fabrication Technologies. *IEEE Microwave Magazine*, 24(1), 62–73.

et al., Z. W. (2023e). Automated Antenna Design via Domain Knowledge-Informed Reinforcement Learning and Imitation Learning. *IEEE Transactions on Antennas and Propagation*, 71(7), 5549–5557.

et al., Z. W. (2023f). Fully Automated Design Method Based on Reinforcement Learning and Surrogate Modeling for Antenna Array Decoupling. *IEEE Transactions on Antennas and Propagation*, 71(1), 660–671.

et al., Z. W. (2024a). Fast and Automatic Parametric Model Construction of Antenna Structures Using CNN–LSTM Networks. *IEEE Transactions on Antennas and Propagation*, 72(2), 1319–1328.

et al., Z. Z. (2023g). A High-Quality Data Acquisition Method for Machine-Learning-Based Design and Analysis of Electromagnetic Structures. *IEEE Transactions on Microwave Theory and Techniques*, 71(10), 4295–4306.

et al., Z. Z. (2024b). Bayesian-Inspired Sampling for Efficient Machine-Learning-Assisted Microwave Component Design. *IEEE Transactions on Microwave Theory and Techniques*, 72(2), 996–1007.

Fan, F., Yang, J., Vassilev, V. & Zaman, A. U. (2018). Bandwidth investigation on half-height pin in ridge gap waveguide. *IEEE Transactions on Microwave Theory and Techniques*, 66(1), 100–108.

Farahani, H. S., Sadeghzadeh, R. A., Gharanfeli, N. & Kishk, A. A. (2017). Novel design of microwave diplexers using gap waveguide technology. *Microw. Opt. Technol. Lett.*, 59(5), 1133–1136.

Feng, F., Na, W., Jin, J., Zhang, J., Zhang, W. & Zhang, Q.-J. (2022). Artificial Neural Networks for Microwave Computer-Aided Design: The State of the Art. *IEEE Transactions on Microwave Theory and Techniques*, 70(11), 4597-4619.

Ferrage, L., Bertrand, G., Lenormand, P., Grossin, D. & Ben-Nissan, B. (2017). A review of the additive manufacturing (3DP) of bioceramics: alumina, zirconia (PSZ) and hydroxyapatite. *Journal of the Australian Ceramic Society*, 53, 11–20.

Figueiredo, B. P. D. (2017). *Developing New Classes of Thick Origami-Based Mechanisms: Conceal-and-Reveal Motion and Folding Printed Circuit Boards*. (Ph.D. Dissertation, Brigham Young University). Consulted at All Theses and Dissertations. 6646.

Gallo, M., Antonino-Daviu, E., Ferrando-Bataller, M., Bozzetti, M., Molina-Garcia-Pardo, J. M. & Juan-Llacer, L. (2012). A broadband pattern diversity annular slot antenna. *IEEE Transactions on Antennas and Propagation*, 60(3), 1596–1600.

Gandomi, A. H., Alavi, A. H. & Ryan, C. (2015). *Handbook of Genetic Programming Applications* (ed. 1st). Springer Cham.

Gao, D., Cao, Z.-X., Fu, S.-D., Quan, X. & Chen, P. (2020a). A Novel Slot-Array Defected Ground Structure for Decoupling Microstrip Antenna Array. *IEEE Transactions on Antennas and Propagation*, 68(10), 7027-7038.

Gao, D., Cao, Z.-X., Fu, S.-D., Quan, X. & Chen, P. (2020b). A Novel Slot-Array Defected Ground Structure for Decoupling Microstrip Antenna Array. *IEEE Transactions on Antennas and Propagation*, 68(10), 7027-7038.

Gautam, A. K., Yadav, S. & Rambabu, K. (2018). Design of ultra-compact UWB antenna with band-notched characteristics for MIMO applications. *IET Microwaves, Antennas and Propagation*, 12(12), 1895-1900.

Geng, C., Lian, J.-W., Guo, Y. J. & Ding, D. (2024). Millimeter-Wave Three-Layer Substrate-Integrated 9 × 9 Butler Matrix and Its Application to Wide-Angle Endfire Multibeam Metasurface Antenna. *IEEE Transactions on Microwave Theory and Techniques*, 72(4), 2253-2266.

Gibson, I., Rosen, D. W. & Stucker, B. (2010). *Additive Manufacturing Technologies: Rapid Prototyping to Direct Digital Manufacturing*. New York: Springer.

Gibson, I., Rosen, D. W. & Stucker, B. (2015). *Additive Manufacturing Technologies: 3D Printing, Rapid Prototyping, and Direct Digital Manufacturing* (ed. 2nd). Springer.

Gibson, W. C. (2014). *The Method of Moments in Electromagnetics*. CRC Press.

GmbH, E. (n.d.). EOS Aluminium AlSi10Mg Material Data Sheet. Available: https://www.eos.info/material-m/metal-materials/aluminium-alsi10mg.

Golboni, H., Arezoomand, M., Pirhadi, A. & Asadi, S. (2020). Design of high-selective printed-ridge gap waveguide filter using source–load and cross couplings. *IEEE Microw. Wireless Compon. Lett.*, 30(6), 557–560.

Gothait, H., Peleg, R. A. & Baharav, O. *(2001)*.

Gross, B. C., Erkal, J. L., Lockwood, S. Y., Chen, C. & Spence, D. M. (2014). Evaluation of 3D Printing and Its Potential Impact on Biotechnology and the Chemical Sciences. *Analytical Chemistry*, 86, 3240–3253.

Gupta, A., Karahan, E. A., Bhat, C., Sengupta, K. & Khankhoje, U. K. (2023). Tandem Neural Network Based Design of Multiband Antennas. *IEEE Transactions on Antennas and Propagation*, 71(8), 6308-6317. doi: 10.1109/TAP.2023.3276524.

Hamedani, M., Oraizi, H., Amini, A., Zarifi, D. & Zaman, A. U. (2020). Planar H-plane horn antenna based on groove gap waveguide technology. *IEEE Antennas and Wireless Propagation Letters*, 19(2), 302-306.

Hamza, M., Zekios, C. L. & Georgakopoulos, S. V. (2020). A Thick Origami Reconfigurable and Packable Patch Array With Enhanced Beam Steering. *IEEE Transactions on Antennas and Propagation*, 68(5), 3653–3663.

Haykin, S. O. (2008). *Neural Networks and Learning Machines*. Prentice Hall.

Hehenberger, S. P., Caizzone, S. & Yarovoy, A. G. (2023). Additive Manufacturing of Linear Continuous Permittivity Profiles and Their Application to Cylindrical Dielectric Resonator Antennas. *IEEE Open Journal of Antennas and Propagation*, 4, 373–382.

Hon, K., Li, L. & Hutchings, I. (2008). Direct writing technology—Advances and developments. *CIRP Annals - Manufacturing Technology*, 57(2), 601–620.

Horestani, A. K. & Shahabadi, M. (2018). Balanced filter with wideband common-mode suppression in groove gap waveguide technology. *IEEE Microw. Wireless Compon. Lett.*, 28(2), 132–134.

Hosseini, S. S. S. & Nemati, A. (2015). Application of Genetic Programming for Electrical Engineering Predictive Modeling: A Review. In Gandomi, A., Alavi, A. & Ryan, C. (Eds.), *Handbook of Genetic Programming Applications* (pp. 105-123). Springer.

Huang, H., Yang, X.-S. & Wang, B.-Z. (2023). Machine-Learning-Based Generative Optimization Method and Its Application to an Antenna Decoupling Design. *IEEE Transactions on Antennas and Propagation*, 71(7), 6243-6248.

Huang, J., Chen, S. J., Xue, Z., Withayachumnankul, W. & Fumeaux, C. (2018a). Impact of Infill Pattern on 3D Printed Dielectric Resonator Antennas. *2018 IEEE Asia-Pacific Conference on Antennas and Propagation (APCAP)*, pp. 233–235.

Huang, J., Chen, S. J., Xue, Z., Withayachumnankul, W. & Fumeaux, C. (2018b). Wideband endfire 3-D-printed dielectric antenna with designable permittivity. *IEEE Antennas and Wireless Propagation Letters*, 17, 2085–2089.

Hull, C. W. *(1986)*.

Jacob, P. F. (1992). *Rapid Prototyping and Manufacturing: Fundamentals of Stereolithography*. SME.

Jain, S., Patnaik, A. & Sinha, S. (2011). Neural network-based particle swarm optimizer for design of dual resonance X/Ku band stacked patch antenna. *IEEE International Symposium on Antennas and Propagation (APSURSI)*.

Jain, S. K. (2016). Bandwidth enhancement of patch antennas using neural network dependent modified optimizer. *Int J Microw Wirel Technol.*, 8(7), 1111–1119.

Jain, S. K., Patnaik, A. & Sinha, S. N. (2013). Design of custom-made stacked patch antennas: a machine learning approach. *Int J Mach Learn Cybernet.*, 4, 189–194.

Jin, J., Zhang, C., Feng, F., Na, W., Ma, J. & Zhang, Q. (2019). Deep neural network technique for high-dimensional microwave modeling and applications to parameter extraction of microwave filters. *IEEE Transactions on Microwave Theory and Techniques*, 67(10), 4140-4155.

Jun, S. Y. 3D Thesis: Additive Manufacturing for Antenna Applications. Thesis.

Juste, E., Petit, F., Lardot, V. & Cambier, F. (2014). Shaping of ceramic parts by selective laser melting of powder bed. *Journal of Materials Research*, 29(17), 2086–2094.

Karahan, E. A., Liu, Z., Gupta, A. et al. (2024a). Deep-learning enabled generalized inverse design of multi-port radio-frequency and sub-terahertz passives and integrated circuits. *Nature Communications*, 15, 10734. doi: 10.1038/s41467-024-54178-1.

Karahan, E. A., Gupta, A., Khankhoje, U. K. & Sengupta, K. (2022). Deep Learning based Modeling and Inverse Design for Arbitrary Planar Antenna Structures at RF and Millimeter-Wave. *2022 IEEE International Symposium on Antennas and Propagation and USNC-URSI Radio Science Meeting (AP-S/URSI)*, pp. 499-500. doi: 10.1109/AP-S/USNC-URSI47032.2022.9887077.

Karahan, E. A., Liu, Z. & Sengupta, K. (2023). Deep-Learning-Based Inverse-Designed Millimeter-Wave Passives and Power Amplifiers. *IEEE Journal of Solid-State Circuits*, 58(11), 3074-3088. doi: 10.1109/JSSC.2023.3276315.

Karahan, E. A., Shao, Z. & Sengupta, K. (2024b). Deep Learning Aided Modelling and Inverse Design for Multi-Port Antennas. *2024 IEEE International Symposium on Antennas and Propagation and INC/USNC-URSI Radio Science Meeting (AP-S/INC-USNC-URSI)*, pp. 799-800. doi: 10.1109/AP-S/INC-USNC-URSI52054.2024.10686871.

Kawase, T., Moriya, S., Newsome, C. J. & Shimoda, T. (2005). Inkjet printing of polymeric field-effect transistors and its applications. *Jpn. J. Appl. Phys.*, 44(6A), 3649–3658.

Khan, I., Zhang, K., Ali, L. & Wu, Q. (2023). A Compact FSS-Based Four-Port MIMO Antenna for Low Mutual Coupling. *IEEE Antennas and Wireless Propagation Letters*, 22(12), 2836-2840.

Khan, M. S., Capobianco, A.-D., Najam, A. I., Shoaib, I., Autizi, E. & Shafique, M. F. (2014). Compact ultra-wideband diversity antenna with a floating parasitic digitated decoupling structure. *IET Microwaves, Antennas and Propagation*, 8(10), 747-753. doi: https://doi.org/10.1049/iet-map.2013.0672.

Khan, T. & Roy, C. (2019). Prediction of slot-position and slot-size of a microstrip antenna using support vector regression. *Int. J. RF Microw. Comput Aid Eng.*, 29, e21623.

Khan, T., De, A. & Uddin, M. (2013). Prediction of slot-size and inserted air-gap for improving the performance of rectangular microstrip antennas using artificial neural networks. *IEEE Antennas Wirel Propag Lett.*, 12, 1367–1371.

Khatib, B. Y. E., Djerafi, T. & Wu, K. (2012). Substrate-integrated waveguide vertical interconnects for 3-D integrated circuits. *IEEE Transactions on Components, Packaging and Manufacturing Technology*, 2(9), 1526–1535.

Kiani, S. H., Marey, M., Rafique, U., Shah, S. I. H., Bashir, M. A., Mostafa, H., Wong, S.-W. & Parchin, N. O. (2022). A Deployable and Cost-Effective Kirigami Antenna for Sub-6 GHz MIMO Applications. *Micromachines*, 13(10), 1735.

Kildal, P. S. (1988a). Definition of Artificially Soft and Hard Surfaces for Electromagnetic Waves. *Electronics Letters*, 24(3), 168–170. doi: 10.1049/EL:19880112.

Kildal, P.-S. (1988b). Definition of artificially soft and hard surfaces for electromagnetic waves. *Electronics Letters*, 24(3), 168–170.

Kildal, P.-S. (1990). Artificially soft and hard surfaces in electromagnetics. *IEEE Transactions on Antennas and Propagation*, 38(10), 1537–1544.

Kildal, P. S., Alfonso, E., Valero-Nogueira, A. & Rajo-Iglesias, E. (2009a). Local metamaterial-based waveguides in gaps between parallel metal plates. *IEEE Antennas and Wireless Propagation Letters*, 8, 84–87.

Kildal, P.-S., Alfonso, E., Valero-Nogueira, A. & Rajo-Iglesias, E. (2009b). Local Metamaterial-Based Waveguides in Gaps Between Parallel Metal Plates. *IEEE Antennas and Wireless Propagation Letters*, 8, 84-87. doi: 10.1109/LAWP.2008.2011147.

Kim, I. & Rahmat-Samii, Y. (2015). Electromagnetic band gap-dipole sub-array antennas creating an enhanced tilted beam for future base station. *IET Microwaves, Antennas and Propagation*, 9(4), 319–327.

Koza, J. R. (1992). *Genetic programming: on the programming of computers by means of natural selection*. Cambridge, Mass.: MIT Press.

Kruth, J. P., Leu, M. C. & Nakagawa, T. (1998). Progress in Additive Manufacturing and Rapid Prototyping. *CIRP Annals - Manufacturing Technology*, 47(2), 525–540.

Kruth, J. P., Levy, G., Klocke, F. & Childs, T. H. C. (2007). Consolidation phenomena in laser and powder-bed based layered manufacturing. *CIRP Annals*, 56, 730–759.

Langdon, W. B., Poli, R., McPhee, N. F. & Koza, J. R. (1997). Genetic Programming: An Introduction and Tutorial, with a Survey of Techniques and Methods for the Design of Complex Systems. *IEEE Transactions on Evolutionary Computation*, 1(1), 1-17.

learn Contributors, S. [Scikit-learn: Machine Learning in Python]. sklearn.model_selection.GridSearchCV. Consulted at https://scikit-learn.org/stable/modules/generated/sklearn.model_selection.GridSearchCV.html.

Li, S., Chen, Z. N., Li, T., Lin, F. H. & Yin, X. (2020). Characterization of metasurface lens antenna for sub-6 GHz dual-polarization full-dimension massive MIMO and multibeam systems. *IEEE Transactions on Antennas and Propagation*, 68(3), 1366–1377.

Li, T. & Chen, Z. N. (2020). Wideband sidelobe-level reduced Ka-band metasurface antenna array fed by substrate-integrated gap waveguide using characteristic mode analysis. *IEEE Transactions on Antennas and Propagation*, 68(3), 1356-1365.

Liang, Y.-Z., Chen, F.-C., Zeng, W.-F. & Chu, Q.-X. (2023). Design of Self-Decoupling Dielectric Resonator Antenna With Shared Radiator. *IEEE Transactions on Antennas and Propagation*, 71(1), 1053–1058.

Liu, N.-W., Liang, Y.-D., Zhu, L., Liu, Z.-X., Liu, Y. & Sun, S. (2023). Mutual Coupling Reduction of a Dual-Band Four-Port Patch Antenna With Co-Polarized Radiation Pattern by Controlling Electric Fields. *IEEE Transactions on Antennas and Propagation*, 71(5), 4534-4539.

Liu, Q., Zhu, L. & Lu, W.-J. (2024). Decoupling of Closely Spaced Square Patch Antennas Using Short-Circuited /2 Microstrip Line. *IEEE Antennas and Wireless Propagation Letters*, 23(2), 728-732.

Liu, X., Wu, Y., Zhuang, Z., Wang, W. & Liu, Y. (2018). A dual-band patch antenna for pattern diversity application. *IEEE Access*, 6, 51986–51993.

Liu, Y., Yue, Z., Jia, Y., Xu, Y. & Xue, Q. (2021). Dual-Band Dual-Circularly Polarized Antenna Array With Printed Ridge Gap Waveguide. *IEEE Transactions on Antennas and Propagation*, 69(8), 5118-5123.

Liu, Y.-F., Peng, L. & Shao, W. (2022). An Efficient Knowledge-Based Artificial Neural Network for the Design of Circularly Polarized 3-D-Printed Lens Antenna. *IEEE Transactions on Antennas and Propagation*, 70(7), 5007-5014.

Lu, L., Pestourie, R., Yao, W., Wang, Z., Verdugo, F. & Johnson, S. G. (2021). Physics-Informed Neural Networks with Hard Constraints for Inverse Design. *SIAM Journal on Scientific Computing*, 43(6), B1105-B1132. doi: 10.1137/21M1397908.

Ma, J., Dang, S., Watkins, G., Morris, K. & Beach, M. (2023). A high-performance transfer learning-based model for microwave structure behavior prediction. *IEEE Transactions on Circuits and Systems II: Express Briefs*, 70(12), 4394-4398.

Marsland, S. (2014a). *Machine Learning: An Algorithmic Perspective* (ed. Second). Chapman and Hall/CRC.

Marsland, S. (2014b). *Machine Learning: An Algorithmic Perspective, Second Edition*. Chapman and Hall/CRC.

Martinez-Ramon, M. & Christodoulou, C. (2006). *Support vector machines for antenna array processing and electromagnetics*.

Misilmani, E., Naous, H., Khatib, T. A. & Salwa. (2020a). A Review on the Design and Optimization of Antennas Using Machine Learning Algorithms and Techniques. *International Journal of RF and Microwave Computer-Aided Engineering*. doi: 10.1002/mmce.22356.

Misilmani, E., Naous, H., Khatib, T. A. & Salwa. (2020b). A Review on the Design and Optimization of Antennas Using Machine Learning Algorithms and Techniques. *International Journal of RF and Microwave Computer-Aided Engineering*.

Misilmani, H. M. E., Naous, T. & Khatib, S. K. A. (2020c). A review on the design and optimization of antennas using machine learning algorithms and techniques. *International Journal of RF and Microwave Computer-Aided Engineering*, 30, e22356.

Mohammadpour, M., Mohajeri, F. & Razavi, S. A. (2022). A new wide band and compact H-plane horn antenna based on groove gap waveguide technology. *IEEE Trans. Antennas Propag.*, 70(1), 221–228.

Mongia, R. K., Ittibipoon, A. & Cuhaci, M. (1994). Low-profile dielectric resonator antennas using a very high permittivity material. *Electronics Letters*, 30(17), 1362–1363.

Murphy, K. P. (2012). *Machine Learning: A Probabilistic Perspective*. MIT Press.

Na, W., Bai, T., Jin, D., Xie, H., Zhang, W. & Zhang, Q.-J. (2025). Advanced Neural Space Mapping-Based Inverse Modeling Method for Microwave Filter Design. *IEEE Microwave and Wireless Technology Letters*, 35(1), 12-15.

Nakmouche, M. F., Deslandes, D. & Gagnon, G. 3D Printed Ridge Gap Waveguide Automated Design Approach Using Machine Learning. *IEEE Transactions on Microwave Theory and Techniques*. To be published.

Nakmouche, M. F., Deslandes, D., Nedil, M. & Gagnon, G. Machine Learning-Aided Design of Defected Ground Structures for PRGW-Based MIMO Antennas. Submitted for publication.

Nakmouche, M. F., Deslandes, D., Nedil, M. & Gagnon, G. Machine Learning-Aided Design of Defected Ground Structures for PRGW-Based MIMO Antennas. submitted for publication.

Nan, J., Xie, H., Gao, M., Song, Y. & Yang, W. (2021a). Design of UWB Antenna Based on Improved Deep Belief Network and Extreme Learning Machine Surrogate Models. *IEEE Access*, 9, 126541–126549. doi: 10.1109/ACCESS.2021.3111902.

Nan, J., Xie, H., Gao, M., Song, Y. & Yang, W. (2021b). Design of UWB antenna based on improved deep belief networks and extreme learning machine surrogate models. *IEEE Access*, 9, 126541-126549.

Naous, T., Merie, A. A., Khatib, S. K. A., Al-Husseini, M., Shubair, R. M. & Misilmani, H. M. E. (2022). Machine Learning-Aided Design of Dielectric-Filled Slotted Waveguide Antennas with Specified Sidelobe Levels. *IEEE Access*. doi: 10.1109/ACCESS.2022.3158976.

Nasr, M. A. & Kishk, A. A. (2019). Vertical coaxial-to-ridge waveguide transitions for ridge and ridge gap waveguides with 4:1 bandwidth. *IEEE Transactions on Microwave Theory and Techniques*, 67(1), 86–93.

Ourir, A., Rachedi, K., Phan-Huy, D.-T., Leray, C. & de Rosny, J. (2017, Mar.). Compact reconfigurable antenna with radiation pattern diversity for spatial modulation. *Proceedings of the 11th European Conference on Antennas and Propagation (EUCAP)*, pp. 3038–3043.

Palomares-Caballero, , Alex-Amor, A., Valenzuela-Valdés, J. & Padilla, P. (2021). Millimeter-Wave 3-D-Printed Antenna Array Based on Gap-Waveguide Technology and Split E-Plane Waveguide. *IEEE Transactions on Antennas and Propagation*, 69(1), 164–172.

Pan, Y. M. & Zheng, S. Y. (2016). A low-profile stacked dielectric resonator antenna with high-gain and wide bandwidth. *IEEE Antennas and Wireless Propagation Letters*, 15, 68–71.

Pan, Y. M., Leung, K. W. & Lu, K. (2019). Study of Resonant Modes in Rectangular Dielectric Resonator Antenna Based on Radar Cross Section. *IEEE Transactions on Antennas and Propagation*, 67(6), 4200–4205.

Patnaik, A. & Sinha, S. (2011). Design of custom-made fractal multi-band antennas using ANN-PSO. *IEEE Antennas Propag Mag.*, 53, 94–101.

Peng, S., Pu, Y., Wu, Z., Chen, X. & Luo, Y. (2021a). Embedded Bed of Nails With Robustness Suitable for Broadband Gap Waveguide Technology. *IEEE Transactions on Microwave Theory and Techniques*, 69(12), 5317–5326.

Peng, S., Pu, Y., Wu, Z., Chen, X. & Luo, Y. (2021b). A Broadband Transition From Ridge Gap Waveguide to Microstrip Using Suspended Line Coupling. *IEEE Microwave and Wireless Components Letters*, 31(3), 253–256.

Peng, S., Pu, Y., Wu, Z., Chen, X. & Luo, Y. (2021c). A broadband transition from ridge gap waveguide to microstrip using suspended line coupling. *IEEE Microwave and Wireless Components Letters*, 31(3), 253–256.

Peng, S., Pu, Y., Wu, Z. & Luo, Y. (2022a). High-Isolation Power Divider Based on Ridge Gap Waveguide for Broadband Millimeter-Wave Applications. *IEEE Transactions on Microwave Theory and Techniques*, 70(6), 3029–3039.

Peng, S., Pu, Y., Wu, Z. & Luo, Y. (2022b). Compact Ka-Band Magic-T Using Waveguide to Microstrip Dual-Probe Transition. *IEEE Microwave and Wireless Components Letters*, 32(8), 946–949.

Peng, S., Pu, Y., Jiang, Z., Chen, X., Wu, Z. & Luo, Y. (2023a). A Simple Way to Enhance the Isolation of Ridge Gap Waveguide T-Junction, for Application to Millimeter-Wave Feeder Networks. *IEEE Microwave and Wireless Technology Letters*, 33(7), 975–978.

Peng, S., Pu, Y., Jiang, Z., Chen, X., Wu, Z. & Luo, Y. (2023b). A Simple Way to Enhance the Isolation of Ridge Gap Waveguide T-Junction, for Application to Millimeter-Wave Feeder Networks. *IEEE Microwave and Wireless Technology Letters*, 33(7), 975–978.

Petosa, A. (2007). *Dielectric Resonator Antenna Handbook*. Artech House.

Petosa, A. & Ittipiboon, A. (2010). Dielectric resonator antennas: A historical review and the current state of the art. *IEEE Antennas and Propagation Magazine*, 52(5), 91–116.

Peverini, O. A., Lumia, M., Addamo, G., Virone, G. & Fonseca, N. J. G. (2023a). How 3D-Printing Is Changing RF Front-End Design for Space Applications. *IEEE Journal of Microwaves*, 3(2), 800–814.

Peverini, O. A., Lumia, M., Addamo, G., Virone, G. & Fonseca, N. J. G. (2023b). How 3D-Printing Is Changing RF Front-End Design for Space Applications. *IEEE Journal of Microwaves*, 3(2), 800–814.

Polemi, A. & Maci, S. (2010a). Closed form expressions for the modal dispersion equations and for the characteristic impedance of a metamaterial based gap waveguide. *IET Microwave, Antennas and Propagation*, 4(8), 1073–1080.

Polemi, A. & Maci, S. (2010b). Closed-Form Expressions for the Modal Dispersion Equations and for the Characteristic Impedance of a Metamaterial-Based Gap Waveguide. *IET Microwaves, Antennas and Propagation*, 4(8), 1073–1080. doi: 10.1049/iet-map.2009.0125.

Pozar, D. M. (2011). *Microwave Engineering* (ed. 4th). Hoboken, NJ: Wiley.

Pérez-Quintana, D., Bilitos, C., Ruiz-García, J., Ederra, I., Teniente-Vallinas, J., González-Ovejero, D. & Beruete, M. (2023). Fully Metallic Luneburg Metalens Antenna in Gap Waveguide Technology at V-Band. *IEEE Transactions on Antennas and Propagation*, 71(4), 2930-2937. doi: 10.1109/TAP.2023.3243277.

Qian, B., Chen, X. & Kishk, A. A. (2021). Decoupling of microstrip antennas with defected ground structure using the common/differential mode theory. *IEEE Antennas and Wireless Propagation Letters*, 20(5), 828-832.

Qian, B., Huang, X., Chen, X., Abdullah, M., Zhao, L. & Kishk, A. A. (2022). Surrogate-Assisted Defected Ground Structure Design for Reducing Mutual Coupling in 2 × 2 Microstrip Antenna Array. *IEEE Antennas and Wireless Propagation Letters*, 21(2), 351-355.

Qian, B., Chen, X., Zhao, L., Chen, J. & Kishk, A. A. (2023). Reduced Cross-Polarization and Backside Radiations for Rectangular Microstrip Antennas Using Defected Ground Structure Combined With Decoupling Structure. *IEEE Antennas and Wireless Propagation Letters*, 22(3), 517-521.

Qu, L., Piao, H. & Kim, H. (2019). Compact wideband MIMO mobile-antenna system design using mode-based decoupling techniques. *International Journal of RF and Microwave Computer-Aided Engineering*, 29(8), e21765. doi: https://doi.org/10.1002/mmce.21765.

Rajo-Iglesias, E. & Kildal, P.-S. (2009). Cut-off bandwidth of meta-material based parallel plate gap waveguide with one textured metal pin surface. *2009 3rd European Conference on Antennas and Propagation*, pp. 33–36.

Rajo-Iglesias, E. & Kildal, P.-S. (2011a). Numerical studies of bandwidth of parallel-plate cut-off realised by a bed of nails, corrugations and mushroom-type electromagnetic bandgap for use in gap waveguides. *IET Microwaves, Antennas and Propagation*, 5(3), 282–289.

Rajo-Iglesias, E. & Kildal, P.-S. (2011b). Numerical studies of bandwidth of parallel-plate cut-off realised by a bed of nails, corrugations and mushroom-type electromagnetic bandgap for use in gap waveguides. *IET Microwaves, Antennas and Propagation*, 5(3), 282-289.

Rajo-Iglesias, E. & Kildal, P.-S. (2011c). Numerical studies of bandwidth of parallel-plate cut-off realised by a bed of nails, corrugations and mushroom-type electromagnetic bandgap for use in gap waveguides. *IET Microwaves, Antennas and Propagation*, 5, 282-289. doi: 10.1049/iet-map.2010.0073.

Rajo-Iglesias, E., Caiazzo, M., Inclán-Sánchez, L. & Kildal, P.-S. (2007a). Comparison of bandgaps of mushroom-type EBG surface and corrugated and strip-type soft surfaces. *IET Microwaves, Antennas and Propagation*, 1, 184–189.

Rajo-Iglesias, E., Caiazzo, M., Inclán-Sánchez, L. & Kildal, P.-S. (2007b). Comparison of bandgaps of mushroom-type EBG surface and corrugated and strip-type soft surfaces. *IET Microwaves, Antennas and Propagation*, 1, 184-189.

Rajo-Iglesias, E., Ferrando-Rocher, M. & Zaman, A. U. (2018a). Gap waveguide technology for millimeter-wave antenna systems. *IEEE Communications Magazine*, 56(7), 14-20.

Rajo-Iglesias, E., Ferrando-Rocher, M. & Zaman, A. U. (2018b). Gap Waveguide Technology for Millimeter-Wave Antenna Systems. *IEEE Communications Magazine*, 56(7), 14-20. doi: 10.1109/MCOM.2018.1700998.

Ramamurthy, B. (2018). *MIMO for satellite communication systems*. (Ph.D. thesis, University of South Australia, Adelaide, SA, Australia).

Rasiya, G., Shukla, A. & Saran, K. (2021). Additive Manufacturing-A Review. *Materials Today: Proceedings*, 47, 6896–6901. doi: 10.1016/j.matpr.2021.05.181.

Ren, Q., Zaman, A. U., Yang, J., Vassilev, V. & Bencivenni, C. (2022). Novel Integration Techniques for Gap Waveguides and MMICs Suitable for Multilayer Waveguide Applications. *IEEE Transactions on Microwave Theory and Techniques*, 70(9), 4120–4128.

Rezaee, M. & Zaman, A. U. (2017). Realisation of carved and iris groove gap waveguide filter and E-plane diplexer for V-band radio link application. *IET Microw., Antennas Propag.*, 11(15), 2109–2115.

Rizzoli, V., Costanzo, A., Masotti, D., Lipparini, A. & Mastri, F. (2004). Computer-aided optimization of nonlinear microwave circuits with the aid of electromagnetic simulation. *IEEE Transactions on Microwave Theory and Techniques*, 52(1), 362-377.

Roy, C. & Wu, K. (2022). Homotopy Optimization and ANN Modeling of Millimeter-Wave SIW Cruciform Coupler. *IEEE Transactions on Microwave Theory and Techniques*, 70(11), 4751–4764.

Roy, C. & Wu, K. (TBD). Surrogate Model-Based Filter Optimization by a Field-Circuit Model Mapping. *IEEE Transactions on Microwave Theory and Techniques*.

Roy, C., Lin, W. & Wu, K. (2023). Swarm Intelligence-Homotopy Hybrid Optimization-Based ANN Model for Tunable Bandpass Filter. *IEEE Transactions on Microwave Theory and Techniques*, 71(6), 2567–2581.

Sadri-Moshkenani, P., Rashed-Mohassel, J. & Shahabadi, M. (2018). Microstrip antenna array fed by a low-loss gap-waveguide feed network. *IEEE Transactions on Antennas and Propagation*, 66(8), 4359-4363.

Sanchez-Cabello, C., Herran, L. F. & Rajo-Iglesias, E. (2020). Ka-band diplexer for 5G mmWave applications in inverted microstrip gap waveguide technology. *Electronics*, 9(12), 2094.

Santiago, D., Laso, M. A. G., Lopetegi, T. & Arregui, I. (2023). Novel Design Method for Millimeter-Wave Gap Waveguide Low-Pass Filters Using Advanced Manufacturing Techniques. *IEEE Access*, 11, 89711–89719.

Scikit-learn Community. (Accessed 2025a). Scikit-learn: Machine Learning in Python.

Scikit-learn Community. (Accessed 2025b). Scikit-learn documentation.

Scikit-learn Community. (Accessed 2025c). Scikit-learn: Machine Learning in Python.

Shah, M. A., Lee, D.-G., Lee, B.-Y. & Hur, S. (2021). Classifications and Applications of Inkjet Printing Technology: A Review. *IEEE Access*, 9, 140079-140102. doi: 10.1109/ACCESS.2021.3119219.

Shalev-Shwartz, S. & Ben-David, S. (2014a). *Understanding Machine Learning: From Theory to Algorithms*. Cambridge University Press.

Shalev-Shwartz, S. & Ben-David, S. (2014b). *Understanding Machine Learning: From Theory to Algorithms*. Cambridge University Press.

Shams, S. I. & Kishk, A. A. (2017a). Printed texture with triangle flat pins for bandwidth enhancement of the ridge gap waveguide. *IEEE Transactions on Microwave Theory and Techniques*, 65(6), 2093–2100.

Shams, S. I. & Kishk, A. A. (2017b). Determining the stop band of a Periodic Bed of Nails from the Dispersion Relation Measurements Prediction. *IEEE Transactions on Components, Packaging and Manufacturing Technology*, 7(4), 621-629.

Sharifi Sorkherizi, M. & Kishk, A. A. (2017). Self-Packaged, Low-Loss, Planar Bandpass Filters for Millimeter-Wave Application Based on Printed Gap Waveguide Technology. *IEEE Transactions on Components, Packaging and Manufacturing Technology*, 7(9), 1419-1431. doi: 10.1109/TCPMT.2017.2702753.

Sharma, Y., Wu, J., Xin, H. & Zhang, H. (2017). Sparse linear regression for optimizing design parameters of double T-shaped monopole antennas. *IEEE International Symposium on Antennas and Propagation USNC/URSI National Radio Science Meeting*.

Sharma, Y., Zhang, H. H. & Xin, H. (2020a). Machine learning techniques for optimizing design of double T-shaped monopole antenna. *IEEE Transactions on Antennas and Propagation*, 68(7), 5658–5663.

Sharma, Y., Zhang, H. H. & Xin, H. (2020b). Machine learning techniques for optimizing design of double T-shaped monopole antenna. *IEEE Trans Antenna Propag*.

Sharma, Y., Zhang, H. H. & Xin, H. (2020c). Machine Learning Techniques for Optimizing Design of Double T-Shaped Monopole Antenna. *IEEE Transactions on Antennas and Propagation*, 68(7), 5658-5663.

Sharma, Y., Chen, X., Wu, J., Zhou, Q., Zhang, H. H. & Xin, H. (2022). Machine Learning Methods-Based Modeling and Optimization of 3-D-Printed Dielectrics Around Monopole Antenna. *IEEE Transactions on Antennas and Propagation*, 70(7), 4997–5006.

Shen, D., Wang, K. & Zhang, X. (2018). A substrate integrated gap waveguide based wideband 3-dB coupler for 5G applications. *IEEE Access*, 6, 6679-66806.

Shi, L. P., Zhang, Q. H., Zhang, S. H., Yi, C. & Liu, G. X. (2021a). Efficient Graphene Reconfigurable Reflectarray Antenna Electromagnetic Response Prediction Using Deep Learning. *IEEE Access*, 9, 22671–22678.

Shi, Y., Feng, W. & Cao, B. (2021b). W-Band Gap Waveguide Antenna Array: Passive/Active Component Gap Waveguide Transition Interface for System Integration. *IEEE Antennas and Propagation Magazine*, 63(2), 40–49.

Shi, Y., Feng, W. & Cao, B. (2021c). W-Band Gap Waveguide Antenna Array: Passive/Active Component Gap Waveguide Transition Interface for System Integration. *IEEE Antennas and Propagation Magazine*, 63(2), 40–49.

Shi, Y., Feng, W., Qian, Z., He, S., Zhou, X. Y., Xue, Q., Che, W. & Wu, Q. (2023). Gap Waveguide Technology: An Overview of Millimeter-Wave Circuits Based on Gap Waveguide Technology Using Different Fabrication Technologies. *IEEE Microwave Magazine*, 24(1), 62-73. doi: 10.1109/MMM.2022.3211595.

Sievenpiper, D., Zhang, L., Jimenez-Broas, F., Alexopolous, N. & Yablonovitch, E. (1999). High-impedance electromagnetic surfaces with a forbidden frequency band. *IEEE Transactions on Microwave Theory and Techniques*, 47, 2059-2074.

Silveirinha, M. G., Fernandes, C. A. & Costa, J. R. (2008a). Electromagnetic characterization of textured surfaces formed by metallic pins. *IEEE Transactions on Antennas and Propagation*, 56, 405–415.

Silveirinha, M. G., Fernandes, C. A. & Costa, J. R. (2008b). Electromagnetic Characterization of Textured Surfaces Formed by Metallic Pins. *IEEE Transactions on Antennas and Propagation*, 56(2), 405–415. doi: 10.1109/TAP.2007.915449.

Singh, M., Haverinen, H. M., Dhagat, P. & Jabbour, G. E. (2010a). Inkjet Printing Process and Its Applications. *Adv. Mater.*, 22(6), 673–685.

Singh, M., Haverinen, H. M., Dhagat, P. & Jabbour, G. E. (2010b). Inkjet Printing—Process and Its Applications. *Adv. Mater.*, 22, 673–685. doi: 10.1002/adma.200901141.

Singh, R., Gupta, A., Tripathi, O., Srivastava, S., Singh, B., Awasthi, A., Rajput, S., Sonia, P., Singhal, P. & Saxena, K. K. (2020). Powder bed fusion process in additive manufacturing: An overview. *Materials Today: Proceedings*, 26, 3058–3070.

Sokunbi, O. & Kishk, A. A. (2023). Millimeter-Wave ME-Dipole Array Antenna Decoupling Using a Novel Metasurface Structure. *IEEE Access*, 11, 129854-129865. doi: 10.1109/ACCESS.2023.3329750.

Song, S., Wang, A., Huang, Q. & Tsung, F. (2014). Shape deviation modeling for fused deposition modeling processes. *2014 IEEE International Conference on Automation Science and Engineering (CASE)*, pp. 758–763.

Sorkherizi, M. S. & Kishk, A. A. (2017). Self-packaged, low-loss, planar bandpass filters for millimeter-wave application based on printed gap waveguide technology. *IEEE Trans. Compon., Packag., Manuf. Technol.*, 7(9), 1419–1431.

Sorkherizi, M. S., Dadgarpour, A. & Kishk, A. A. (2017). Planar high-efficiency antenna array using new printed ridge gap waveguide technology. *IEEE Transactions on Antennas and Propagation*, 65(7), 3772-3776.

Srivastava, T. [Analytics Vidhya]. (2014, Oct.). Introduction to K-Nearest Neighbors: A Powerful Machine Learning Algorithm. Consulted at https://www.analyticsvidhya.com/blog/2018/03/introductionk-neighbours -algorithm-clustering.

Su, S., Lee, C. & Chang, F. (2012). Printed MIMO-antenna system using neutralization-line technique for wireless USB-dongle applications. *IEEE Transactions on Antennas and Propagation*, 60(2), 456-463.

Sufian, M. A., Hussain, N., Abbas, A., Lee, J., Park, S. G. & Kim, N. (2022). Mutual coupling reduction of a circularly polarized MIMO antenna using parasitic elements and DGS for V2X communications. *IEEE Access*, 10, 56388-56400.

Sumithra, P. & Thiripurasundari, D. (2017). Review on computational electromagnetics. *Advances in Electromagnetics*, 6, 42–55.

Sun, J. X., Cheng, Y. J., Wang, L. & Fan, Y. (2023). Three-Dimensional Interconnection With Magnetically Coupled Transition for W-Band Integration Applications. *IEEE Transactions on Microwave Theory and Techniques*, 71(1), 112–121.

Swindlehurst, A. L., Ayanoglu, E., Heydari, P. & Capolino, F. (2014). Millimeter-wave massive MIMO: the next wireless revolution. *IEEE Communications Magazine*, 52(9), 56-62. doi: 10.1109/MCOM.2014.6894453.

Tak, J., Kantemur, A., Sharma, Y. & Xin, H. (2018). A 3-D-Printed W-Band Slotted Waveguide Array Antenna Optimized Using Machine Learning. *IEEE Antennas and Wireless Propagation Letters*, 17(11), 2008–2012.

Tamayo-Dominguez, A., Fernandez-Gonzalez, J. & Sierra-Perez, M. (2019). Metal-coated 3D-printed waveguide devices for mm-wave applications [application notes]. *IEEE Microwave Magazine*, 20(9), 18–31.

Tamayo-Domínguez, A., Fernández-González, J. M. & Sierra-Castañer, M. (2021). Monopulse Radial Line Slot Array Antenna Fed by a 3-D-Printed Cavity-Ended Modified Butler Matrix Based on Gap Waveguide at 94 GHz. *IEEE Transactions on Antennas and Propagation*, 69(8), 4558–4568.

Tayli, D. (2018). *Computational Tools for Antenna Analysis and Design*. (Ph.D. thesis, Lund University, Electromagnetic Theory Department of Electrical and Information Technology).

Tomassoni, C., Peverini, O. A., Venanzoni, G., Addamo, G., Paonessa, F. & Virone, G. (2020). 3D printing of microwave and millimeter-wave filters: Additive manufacturing technologies applied in the development of high-performance filters with novel topologies. *IEEE Microwave Magazine*, 21(6), 24–45.

Tong, K., Joshi, S. & Lehtihet, E. A. (2008). Error compensation for fused deposition modeling (FDM) machine by correcting slice files. *Rapid Prototyping Journal*, 14(1), 4–14.

Vai, M. & Prasad, S. (1993). Automatic impedance matching with a neural network. *IEEE Microwave and Guided Wave Letters*, 3(10), 353-354.

Valero-Nogueira, A., Baquero, M., Herranz, J. I., Domenech, J., Alfonso, E. & Vila, A. (2011). Gap Waveguides Using a Suspended Strip on a Bed of Nails. *IEEE Antennas and Wireless Propagation Letters*, 10, 1006-1009. doi: 10.1109/LAWP.2011.2167591.

Vanderplas, J., Pedregosa, F. & Gramfort, A. [GitHub]. (2011, Sep.). Base and Mixin Classes for Nearest Neighbors. Consulted at https://github.com/scikit-learn/scikit-learn/blob/7813f7efb/sklearn/neighbors/base.py#L858.

Vanderplas, J., Pedregosa, F. & Gramfort, A. [Tslearn]. (2017). Source Code for Sklearn.Neighbors.Base. Consulted at https://tslearn.readthedocs.io/en/latest/_modules/sklearn/neighbors/base.html.

Volakis, J. L., Johnson, R. C. & Jasik, H. (2007). *Antenna Engineering Handbook*. New York: McGraw-Hill.

Vosoogh, A. & Kildal, P. (2016). Corporate-fed planar 60-GHz slot array made of three unconnected metal layers using AMC pin surface for the gap waveguide. *IEEE Antennas and Wireless Propagation Letters*, 15, 1935-1938.

Vosoogh, A., Brazález, A. A. & Kildal, P. (2016). A V-band inverted microstrip gap waveguide end-coupled bandpass filter. *IEEE Microw. Wireless Compon. Lett.*, 26(4), 261–263.

Vosoogh, A., Sorkherizi, M. S., Zaman, A. U., Yang, J. & Kishk, A. A. (2018). An integrated Ka-band diplexer-antenna array module based on gap waveguide technology with simple mechanical assembly and no electrical contact requirements. *IEEE Trans. Microw. Theory Techn.*, 66(2), 962–972.

Vosoogh, A., Sharifi Sorkherizi, M., Vassilev, V., Zaman, A. U., He, Z. S., Yang, J., Kishk, A. A. & Zirath, H. (2019a). Compact Integrated Full-Duplex Gap Waveguide-Based Radio Front End For Multi-Gbit/s Point-to-Point Backhaul Links at E-Band. *IEEE Transactions on Microwave Theory and Techniques*, 67(9), 3783-3797. doi: 10.1109/TMTT.2019.2919539.

Vosoogh, A., Zirath, H. & He, Z. S. (2019b). Novel Air-Filled Waveguide Transmission Line Based on Multilayer Thin Metal Plates. *IEEE Transactions on Terahertz Science and Technology*, 9(3), 282-290. doi: 10.1109/TTHZ.2019.2905775.

W, R. & A, S. (2006). The method of moments: a numerical technique for wire antenna design. *High Freq Electron.*, 5, 42–47.

Watson, P. & Gupta, K. C. (1996a, Jun.). EM-ANN models for via interconnects in microstrip circuits. *IEEE MTT-S International Microwave Symposium Digest*, pp. 1819-1822.

Watson, P. M. & Gupta, K. C. (1996b). EM-ANN models for microstrip vias and interconnects in dataset circuits. *IEEE Transactions on Microwave Theory and Techniques*, 44(12), 2495-2503.

Wei, Z. et al. (2023a). Automated Antenna Design via Domain Knowledge-Informed Reinforcement Learning and Imitation Learning. *IEEE Transactions on Antennas and Propagation*, 71(7), 5549–5557.

Wei, Z. et al. (2023b). Fully Automated Design Method Based on Reinforcement Learning and Surrogate Modeling for Antenna Array Decoupling. *IEEE Transactions on Antennas and Propagation*, 71(1), 660–671.

Wei, Z. et al. (2024). Fast and Automatic Parametric Model Construction of Antenna Structures Using CNN–LSTM Networks. *IEEE Transactions on Antennas and Propagation*, 72(2), 1319–1328.

Weir, W. B. (1974). Automatic measurement of complex dielectric constant and permeability at microwave frequencies. *Proceedings of the IEEE*, 62(1), 33–36.

Weng, Z., Wang, X., Jiao, Y. & Zhang, F. (2010). Wideband rectangular dielectric resonator antenna (DRA) with slot-fed design. *Progress in Electromagnetics Research Letters*, 16, 181–190.

Wohlers, T. (2005). *Additive Manufacturing and 3D Printing State of the Industry Annual Worldwide Progress Report*.

Wu, Q., Wang, H. & Hong, W. (2020). Multistage collaborative machine learning and its application to antenna modeling and optimization. *IEEE Transactions on Antennas and Propagation*, 68(5), 3397–3409.

Xia, Z.-X., Leung, K. W. & Lu, K. (2019). 3-D-Printed Wideband Multi-Ring Dielectric Resonator Antenna. *IEEE Antennas and Wireless Propagation Letters*, 18(10), 2110–2114.

Xia, Z.-X., Leung, K. W., Gu, P. & Chen, R. (2022). 3-D-printed wideband high-efficiency dual-frequency antenna for vehicular communications. *IEEE Transactions on Vehicular Technology*, 71(4), 3457–3469.

Xiao, L.-Y., Shao, W., Jin, F.-L. & Wang, B.-Z. (2018). Multiparameter Modeling With ANN for Antenna Design. *IEEE Transactions on Antennas and Propagation*, 66(7), 3718-3723.

Xiao, L.-Y., Shao, W., Jin, F.-L., Wang, B.-Z. & Liu, Q. H. (2021). Inverse Artificial Neural Network for Multiobjective Antenna Design. *IEEE Transactions on Antennas and Propagation*, 69(10), 6651-6659. doi: 10.1109/TAP.2021.3069543.

Xu, Y., Wu, X., Guo, X., Kong, B., Zhang, M., Qian, X., Mi, S. & Sun, W. (2017). The Boom in 3D-Printed Sensor Technology. *Sensors*, 17, 1166.

Yang, T., Jiao, J., Wu, S., Lu, R. & Zhang, Q. (2022). Grant Free Age-Optimal Random Access Protocol for Satellite-Based Internet of Things. *IEEE Transactions on Communications*, 70(6), 3947-3961.

Yang, X., Liu, Y., Xu, Y.-X. & Gong, S. (2017). Isolation enhancement in patch antenna array with fractal UC-EBG structure and cross slot. *IEEE Antennas and Wireless Propagation Letters*, 16, 2175-2178.

Yang, X., Chen, Y., Zhao, Y., Pan, J., Guo, J. & Yang, D. (2023). Application of KNN for Linear Array Pattern Prediction Based on the Active Element Pattern Method. *IEEE Antennas and Wireless Propagation Letters*, 22(5), 1134–1138.

Yin, W., Chen, S., Chang, J., Li, C. & Khamas, S. K. (2021a). CPW fed compact UWB 4-element MIMO antenna with high isolation. *Sensors*, 21(8), 2688.

Yin, W., Chen, S., Chang, J., Li, C. & Khamas, S. K. (2021b). CPW Fed Compact UWB 4-Element MIMO Antenna with High Isolation. *Sensors*, 21(8). doi: 10.3390/s21082688.

Yong, W. Y., Vosoogh, A., Bagheri, A., Van De Ven, C., Hadaddi, A. & Glazunov, A. A. (2023a). An Overview of Recent Development of the Gap-Waveguide Technology for mmWave and Sub-THz Applications. *IEEE Access*, 11, 69378-69400. doi: 10.1109/ACCESS.2023.3293739.

Yong, W. Y., Vosoogh, A., Bagheri, A., Ven, C. V. D., Hadaddi, A. & Glazunov, A. A. (2023b). An Overview of Recent Development of the Gap-Waveguide Technology for mmWave and Sub-THz Applications. *IEEE Access*, 11, 69378–69400. doi: 10.1109/ACCESS.2023.3293739.

Zaman, A. U. & Kildal, P. (2014). Wide-band slot antenna arrays with single-layer corporate-feed network in ridge gap waveguide technology. *IEEE Transactions on Antennas and Propagation*, 62(6), 2992-3001.

Zarifi, D., Farahbakhsh, A. & Zaman, A. U. (2017). A gap waveguide-fed wideband patch antenna array for 60-GHz applications. *IEEE Transactions on Antennas and Propagation*, 65(9), 4875-4879.

Zarifi, D., Shater, A., Ashrafian, A. & Nasri, M. (2018). Design of Ku-band diplexer based on groove gap waveguide technology. *Int. J. RF Microw. Comput.-Aided Eng.*, 28(9), e21487.

Zhang, J., Wei, Z., Kang, K. & Yin, W.-Y. (2024). Intelligent Inverse Designs of Impedance Matching Circuits With Generative Adversarial Network. *IEEE Transactions on Computer-Aided Design of Integrated Circuits and Systems*, 43(10), 3171-3183.

Zhang, Q.-J., Gupta, K. C. & Devabhaktuni, V. K. (2003a). Artificial neural networks for RF and microwave design-from theory to practice. *IEEE Transactions on Microwave Theory and Techniques*, 51(4), 1339-1350.

Zhang, Q.-J., Gupta, K. C. & Devabhaktuni, V. K. (2003b). Artificial neural networks for RF and microwave design - from theory to practice. *IEEE Transactions on Microwave Theory and Techniques*, 51(4), 1339–1350. doi: 10.1109/TMTT.2003.809179.

Zhang, X., Lin, M., Zhang, X. & Li, Y. (2019a). The Design of Microstrip Array Antenna and Its Optimization by a Memetic Method. *IEEE Access*, 7, 96434–96443.

Zhang, Y., Deng, J.-Y., Li, M.-J., Sun, D. & Guo, L.-X. (2019b). A MIMO Dielectric Resonator Antenna With Improved Isolation for 5G mm-Wave Applications. *IEEE Antennas and Wireless Propagation Letters*, 18(4), 747-751.

Zhang, Y., Deng, J.-Y., Li, M.-J., Sun, D. & Guo, L.-X. (2019c). A MIMO Dielectric Resonator Antenna With Improved Isolation for 5G mm-Wave Applications. *IEEE Antennas and Wireless Propagation Letters*, 18(4), 747–751.

Zhao, P. & Wu, K. (2020). Homotopy Optimization of Microwave and Millimeter-Wave Filters Based on Neural Network Model. *IEEE Transactions on Microwave Theory and Techniques*, 68(4), 1390–1400.

Zheng, Y., Vandenbosch, G. A. E. & Yan, S. (2020). Low-profile broadband antenna with pattern diversity. *IEEE Antennas and Wireless Propagation Letters*, 19(7), 1231–1235.

Zheng, Z., Chen, X. & Huang, K. (2011). Application of support vector machines to the antenna design. *Int. J. RF Microw. Comput.-Aided Eng.*, 21(1), 85–90.

Zhou, Z. et al. (2024). Bayesian-Inspired Sampling for Efficient Machine-Learning-Assisted Microwave Component Design. *IEEE Transactions on Microwave Theory and Techniques*, 72(2), 996–1007.